東京大学 大学院新領域創成科学研究科
基盤科学研究系
先端エネルギー工学専攻

平成 25 年度

修士論文

Scaling Law for Argon Anode Layer Hall Thrusters

－ アルゴンアノードレイヤ型ホールスラスタの設計則 －

2014 年 1 月提出
指導教員　小紫　公也　教授

47126091　藤田　大樹

Acknowledgement

I would first like to thank my supervisor, Dr. Kimiya Komurasaki, for guiding my dissertation, and for the opportunity to conduct this research. I would also like to express my gratitude to Dr. Yoshihiro Arakawa, my co-adviser, for advising my research according to his expertise about Hall thrusters. I could never walk through without the guidance of both professors.

I owe special thanks to Dr. Hiroyuki Koizumi, my co-advisor, for his contribution and effort made to complete this research. I would also like to express my gratitude for the contribution to this work made by Dr. Tony Schönherr.

For Dr. Shinatora Cho and Mr. Kawashima, I cannot thank them enough for the support and contribution made by them. Very special thanks also to the members of Hall thruster research group, Mr. Kaneko, Mr. Hosoda, Mr. Ito, Mr. Akagi, and Mr. Suzuki, for the corroborations in experiments and fruitful discussions in seminar. I must thank my colleagues in Arakawa Komurasaki Koizumi laboratory, whom I shared an office for 3 years.

Personally, of course, I would like to thank my family and friends who supported me.

Table of Contents

Chapter 1 Introduction 1
1.1 Electric Propulsion 1
1.2 Basic Principles of Hall thrusters 3
1.2.1 Principle of Operation 4
1.2.2 Type of Hall Thrusters 6
1.2.3 Performance Definition 8
1.3 Application of Alternative Propellants to Hall Thrusters 9
1.4 Japanese 'In-Space Propulsion' 12
1.5 Dissertation Goals 13
Chapter 2 Operation Characteristics of Anode Layer Hall Thrusters and Discharge Current Oscillation 14
2.1 Input Power and Anode Efficiency 14
2.2 Discharge Current Oscillation in Hall Thrusters 15
2.2.1 Oscillation Amplitude of Discharge Current 15
2.2.2 Mechanism of Ionization Oscillation in Hall Thrusters 17
2.3 Operation Characteristics of Hall Thrusters with Argon Propellant 19
2.4 Theory of Ionization Oscillation and Electron Diffusion in Hall Thrusters 20
Chapter 3 Designing of UT-58 Anode Layer Type Hall Thruster 24
3.1 Designing Procedure 24
3.1.1 The Reference Thruster 24
3.1.2 Fundamental Parameters 26
3.1.3 Fundamental Physical Relations for Hall Thruster Scaling 26
3.2 Assuming Specification of UT-58 Anode Layer Hall Thruster 27
3.3 Geometric Structure 28
3.4 Magnetic Circuit with Magnetic Shielding System 29
3.5 Heat Flux Transfer Simulation 32
3.6 Other Noted Points 33
Chapter 4 Experimental Setup 36
4.1 Hollow Cathode 36
4.2 Vacuum System 37
4.3 Thruster Cooling System 38
4.4 Propellant Supplying System 39

4.5 Measurement Systems 42
4.5.1 Electric Circuit 42
4.5.2 Digital Oscilloscope 45
4.5.3 Thrust Balance 46
Chapter 5 Results and Discussions 48
5.1 Discharge Characteristics of UT-58 with Xenon and Argon Propellant 48
5.1.1 Discharge Characteristics of UT-58 with Xenon Propellant 48
5.1.2 Discharge Characteristics of UT-58 with Argon Propellant 50
5.2 Thrust Performance of UT-58 with Xenon and Argon Propellant....53
5.2.1 Thrust Performance of UT-58 with Xenon Propellant 53
5.2.2 Thrust Performance of UT-58 with Argon Propellant 56
5.3 Comparison of Operating Characteristics of UT-58 between Xenon and Argon Propellant..58
5.3.1 Characteristics of Discharge Current and Oscillation Amplitude versus Magnetic Flux Density with Xenon and Argon Propellant 58
5.3.2 The Definition of Common Three Electron Diffusion Modes by Each Oscillation Amplitude with Xenon and Argon Propellant....60
5.3.3 Oscillation Map and Anode Efficiency Map with Xenon and Argon propellant 61
5.3.4 Discussions of the Difference of Optimal Operation Regime between Xenon and Argon Propellant 65
5.4 Design Suggestion for Argon Anode Layer Thruster....69
5.4.1 Internal Efficiencies of UT-58 with Argon Propellant 69
5.4.2 Methods for Improvement of Propellant Utilization Efficiency with Argon Propellant .70
5.4.3 Scaling Method for the Optimal Argon Anode Layer Hall Thrusters 71
5.4.4 Validation of Scaling Method by the Results with Xenon Propellant....78
Chapter 6 Conclusions....81

List of Figures

Figure 1.1 Thrust density and specific impulse of various propulsion systems. 3
Figure 1.2 Picture of Hall thruster operation. 4
Figure 1.3 Principle of Hall thruster operation 5
Figure 1.4 Magnetic layer type (left) and anode layer type (right) Hall thruster. 7
Figure 1.5 Thrust performance of SPT and TAL 7
Figure 1.6 Definition of each current.....9
Figure 1.7 Ideal thrust of alternative propellant compared to xenon 11
Figure 1.8 Ideal specific impulse of alternative propellant compared to xenon 11
Figure 1.9 Development roadmap for next space exploration shown by JAXA.....12
Figure 1.10 Concept of project 'RAIJIN' 13
Figure 2.1 Anode efficiency versus input power of an anode layer Hall thruster in the University of Tokyo 14
Figure 2.2 Operation characteristics of UT-60:.....16
Figure 2.3 Concept of ionization oscillation.....18
Figure 2.4 Typical discharge current oscillation of UT-58 (V_d=250 V, Q= 2.0 Aeq, I_c= 2.0 A) .18
Figure 2.5 Small operation region of UT-38 anode layer Hall thruster.....19
Figure 2.6 Anode efficiency versus discharge voltage of SPT type-93 in the University of Tokyo 19
Figure 2.7 Transition of diffusion coefficient versus magnetic flux density (N.Yamamoto et al.) : Anode layer type, hollow anode D8Z3, V_d =300 V, $\dot{m}$ =2.72 mg/s. 22
Figure 2.8 Typical tendencies of discharge current and oscillation amplitude versus magnetic flux density and three electron diffusion modes. 23
Figure 3.1 Cross-section drawing of UT-55 anode layer thruster 25
Figure 3.2 Magnetic field configuration (Gap = 14).....30
Figure 3.3 Magnetic field configuration (Gap = 19).....30
Figure 3.4 Magnetic field configuration (Gap = 24).....31
Figure 3.5 Axial distribution along with the center line between hollow anode of magnetic flux density with each type, when the coil current is 3 A.....31
Figure 3.6 Temperature profiles of UT-58 calculated by heat flux assumption 33
Figure 3.7 Outlook of OU-58 anode layer Hall thruster 34
Figure 3.8 Cross-section drawing of UT-58 anode layer Hall thruster 34

Figure 3.9 Cross-section drawing of the hollow anode of UT-58 35
Figure 3.10 4 partitions of the plenum chamber 35
Figure 4.1 appearance of hollow cathode 36
Figure 4.2 Operation principle of hollow cathode 37
Figure 4.3 Outlook of 2.0 m×3.0 m vacuum chamber 38
Figure 4.4 Water pump and cooling tower outside of the laboratory 39
Figure 4.5 Mass flow controllers (Left: MODEL3660, Right: MODEL 3200, ... 40
Figure 4.6 Lead-out units (Upper: CR300, Downer: CR700) 41
Figure 4.7 Electric circuit of Hall thruster measurement system 43
Figure 4.8 PPU devices 44
Figure 4.9 Outlook of ion collector. 45
Figure 4.10 Digital oscilloscope. 45
Figure 4.11 Dual pendulum thrust balance. 46
Figure 4.12 Relation of control current versus load and coil current. 47
Figure 5.1 UT-58 operation with xenon propellant 49
Figure 5.2 Discharge characteristics with xenon propellant 49
Figure 5.3 Oscillation characteristics with xenon propellant 50
Figure 5.4 UT-58 operation with argon propellant 51
Figure 5.5 Discharge characteristics with argon propellant 52
Figure 5.6 Oscillation characteristics with argon propellant 52
Figure 5.7 Internal current characteristics with argon propellant (Q=6.0 Aeq) 53
Figure 5.8 Thrust versus input power with xenon propellant 54
Figure 5.9 Thrust performance with xenon propellant 55
Figure 5.10 Comparison of the anode efficiency versus input power with Russia D series 55
Figure 5.11 Thrust versus input power with argon propellant 56
Figure 5.12 Thrust performance with argon propellant 57
Figure 5.13 Typical characteristics of discharge current and oscillation with xenon propellant (V_d=200 V, Q=2.0 Aeq). 59
Figure 5.14 Typical characteristics of discharge current and oscillation with argon propellant (V_d=250 V, Q=6.0 Aeq). 59
Figure 5.15 Three same electron diffusion modes regardless of xenon and argon propellant 61
Figure 5.16 Oscillation map with xenon propellant 63
Figure 5.17 Oscillation map with argon propellant. 63
Figure 5.18 Anode efficiency map with xenon propellant 64
Figure 5.19 Anode efficiency map with argon propellant 64
Figure 5.20 Discharge current and thrust versus magnetic flux density 66

Figure 5.21 Anode efficiency map and discharge voltage lines with xenon propellant.....66
Figure 5.22 Acceleration efficiency and propellant utilization efficiency versus 68
Figure 5.23 Internal efficiencies with argon propellant. 69
Figure 5.24 Relation between channel cross-section area and propellant utilization efficiency with argon propellant. 71
Figure 5.25 Channel geometry determination flow.....73
Figure 5.26 Relation among channel mean diameter, aspect ratio of channel length and channel width, and output anode efficiency (V_d = 250 V, Q = 6.0 Aeq).....74
Figure 5.27 Optimal anode efficiency line with appropriate *d* and *L/b*.....74
Figure 5.28 Relation among channel mean diameter, aspect ratio of channel length and channel width, and output anode efficiency (V_d = 300 V, Q = 7.0 Aeq).....75
Figure 5.29 Optimal anode efficiency line with appropriate *d* and *L/b*.....76
Figure 5.30 Relation among channel mean diameter, aspect ratio of channel length and channel width, and output anode efficiency (V_d = 300 V, Q = 136 Aeq).....78
Figure 5.31 Relation among channel mean diameter, aspect ratio of channel length and channel width, and output anode efficiency with xenon propellant (V_d = 250 V, Q = 3.0 Aeq).....80

List of Tables

Table 1.1 Physical properties of each considerable propellant 10
Table 1.2 Achieved thrust performance of each considerable propellant.....10
Table 3.1 Important parameters and specifications of UT-55 25
Table 3.2 Assumed specifications of a new thruster 28
Table 3.3 Heat flux assumption.....32
Table 3.4 Cooling calculation values 32
Table 4.1 Relative sensitivity of gases 37
Table 4.2 Background pressure during the experiment.....37
Table 5.1 Summary of thrust performance of UT-58 57
Table 5.2 Calculated loss factors of UT-58 with argon propellant.....72
Table 5.3 Supposed specifications of the next generation argon thruster 76
Table 5.4 Required parameters per one thruster for next asteroid mission 77
Table 5.5 Optimal channel geometry for next asteroid mission.....77
Table 5.6 Measured thrust and calculated propellant utilization efficiency with xenon and argon propellant 79

Nomenclature

B = magnetic flux density

b = channel height

C = arbitrary constant

D = diffusion coefficient

d = channel mean diameter

E = electric field

e = elementary charge, 1.6022×10^{-19} C

F = thrust

g = gravitational acceleration constant, 9.80665 m/s^2

I_b = beam current

I_d = discharge current

I_e = electron current

I_g = guard ring current

I_{sp} = specific impulse

k_B = Boltzmann constant, 1.3807×10^{-23} J/K

L = channel length

l = characteristic length of channel

m = mass

$\dot{m}$ = propellant mass flow rate

n = number density

P = input power

Q = number mass flow rate

r = Larmor radius

S = channel cross section area

T = temperature

V_d = discharge voltage

v = velocity

β = product of ionization cross section by averaged electron velocity over electron distribution function

Δ = oscillation amplitude

ε_a = anode sheath losses factor

ε_i = energy losses factor for ionization process

ε_w = wall losses factor

η_A = anode efficiency

η_a = acceleration efficiency

η_e = energy efficiency

η_t = thrust efficiency

η_u = propellant utilization efficiency

κ = propellant mass ratio

λ = mean free path

μ = electron mobility

ν = collision frequency

σ = collision cross section

τ = measured time

$\Delta\varphi$ = potential drop

ω = frequency

Subscripts

e = electron

$exit$ = at channel exit

i = ion

n = neutral particles

ref = reference

z = axial direction

$\perp$ = perpendicular direction to magnetic line

Ar = argon

Xe = xenon

Chapter 1

Introduction

1.1 Electric Propulsion

Recently, a space satellite ‘HAYABUSA’ succeeded in sampling and returning from the asteroid ‘Itokawa’, NASA launched a space satellite ‘Curiosity’ to explore Mars in 2011, or JAXA launched the first Epsilon rocket in 2013. The space development or utilization commercially of space cannot stop, rather accelerate globally. And Great East Japan Earthquake broke up the accident of a nuclear power plant, so people insist on abolishing them not only in Japan but all over the world. The solar power commands a lot of attentions as substitution for the nuclear power. The research of Solar Power Satellite (SPS) is being conducted for the practical use, which launch the solar cells into the space, and can transport the solar energy generated there to the Earth.

Thus, the reduction of cost is essential in developing and utilizing space, and electric propulsion (EP) [1] [2] commands a lot of attentions, which was used also in the HAYABUSA mission. Although the mechanism of thrust generation of EPs is the same as that of the conventional chemical propulsion (CP) systems, usually EPs can achieve higher exhaust velocity and hence specific impulse is higher than CPs by order of magnitude. The definition of specific impulse I_{sp} is written as follows:

$$I_{sp} \equiv \frac{F}{\dot{m}g} = \frac{v}{g} \tag{1.1}$$

Specific impulse is a fundamental and critical performance indication of space propulsion systems which shows how efficiently the propellant is accelerated [3]. Higher specific impulse means less propellant necessary to achieve required final velocity and leads to more payload the vehicle can transport. The advantages of high specific impulse of EP are achieved by the separation of propellant and source of energy. EPs generate the thrust using the electric energy generated by solar cells or nuclear battery unlike the CPs using the chemical energy generated by propellant. Consequently, EP can achieve much higher energy concentration and thus higher exhaust velocity the CP, which enables space missions can never be completed by CP like deep space exploration. On the other hand, the major drawbacks of the EP are the thrust density is very limited compared with CP, and generally EP cannot be used within the atmosphere. Therefore, EP and CP should be selected according to the mission requirements.

Theoretically, the specific impulse of EP can be increased by the increase of input power against

the propellant mass flow rate. However, the increase of input power results in the increased mass for the solar panel (or battery) and power processing unit (PPU), which reduces or even negates the mass saving by the increase of specific impulse. Thus, one always has to take into consideration the mass necessary for the power supply for mission applications of EP. Naturally, another critical performance of EP is thrust efficiency defined by Eq. 1.1 which shows how efficiently the input power was transferred to the thrust.

$$\eta_t \equiv \frac{\frac{1}{2}\dot{m}v^2}{P} = \frac{F^2}{2\dot{m}I_d V_d} \tag{1.2}$$

The efficiency an EP system can achieve depends on the type of the EP, and which specific impulse range to use.

There are three major types of EP according to their propellant acceleration mechanism. The first is electric thermal acceleration thruster represented by Resistojet and Arcjet which utilize electric energy for propellant heating. The acceleration principle is the same as conventional CP that this type of EP is efficient in low specific impulse range (200 - 1,000 s), but can achieve relatively high thrust density (~ 10^4 N/m^2) compared with other EPs. The second is electric magnetic acceleration thruster represented by Magneto Plasma Dynamic (MPD) thruster and Pulsed Plasma Thruster (PPT). This type of EP ionizes the propellant and utilizes Lorenz force for its acceleration and is efficient in the specific impulse range of 1,000 – 10,000 s, and can achieve thrust density of 10^3 N/m^2 – 10^4 N/m^2. The final one is electric static acceleration thruster represented by ion thruster, which ionizes the propellant and accelerates it by static electric field. Ion thruster can perform high thrust efficiency (~ 80 %) at high specific impulse range (2,000 – 20,000 s), though the thrust density can be generated is the lowest among all types of EP. Because there only exists ions at ion acceleration region, the ion beam current density and hence thrust density is regulated by the space charge limit.

The research topic of this study is focused on Hall thruster which has the aspects of both electric magnetic thruster and electric static thruster. Although the ion acceleration of Hall thruster is conducted by static electric field, the quasi-neutrality of acceleration region is sustained that the thrust density can be achieved by Hall thrusters is much higher than that of ion thrusters. Figure 1.1 shows the relation between thrust density and specific impulse of each EPs [1]. Hall thrusters have already been put in practical use, and a lot of researches are being conducted all over the world.

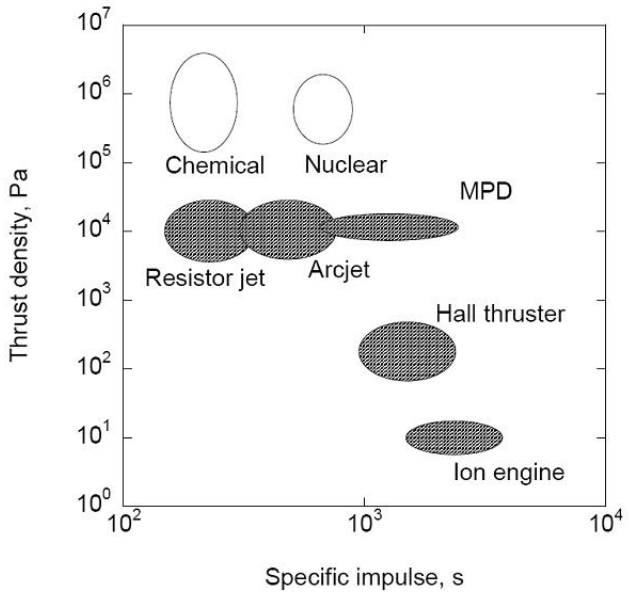

Figure 1.1 Thrust density and specific impulse of various propulsion systems.

1.2 Basic Principles of Hall thrusters

A Hall thruster is one of the most successful electric propulsion which has three major advantages [2] [4]:

1. High thrust efficiency (more than 50 %) at wide specific impulse range (1000 s ~ 3000 s)
2. High thrust density compared with ion thruster
3. Feasibility as a propulsion system (simple and compact, can use various propellant)

The noble gases are mainly used in Hall thrusters as propellants, and xenon is mostly used because it has lower ionization energy than other noble gases. This results in the reduction of the ionization energy ratio, which leads high thrust efficiency in the lower specific impulse range.

Consequently, Hall thrusters are considered to be an ideal propulsion system for satellite missions like station keeping, orbit transfer, or deep space exploration, and currently intensively launched more than 100 Hall thrusters for satellite station keeping. NASA is developing NASA457 50 kW-class high power Hall thruster, ESA has used PPS-1350 [5] [6] Hall thruster for their lunar exploration ‘SMART-1 [7]’ mission, and MELCO [8] is developing a 5 kW-class Japanese Hall thruster.

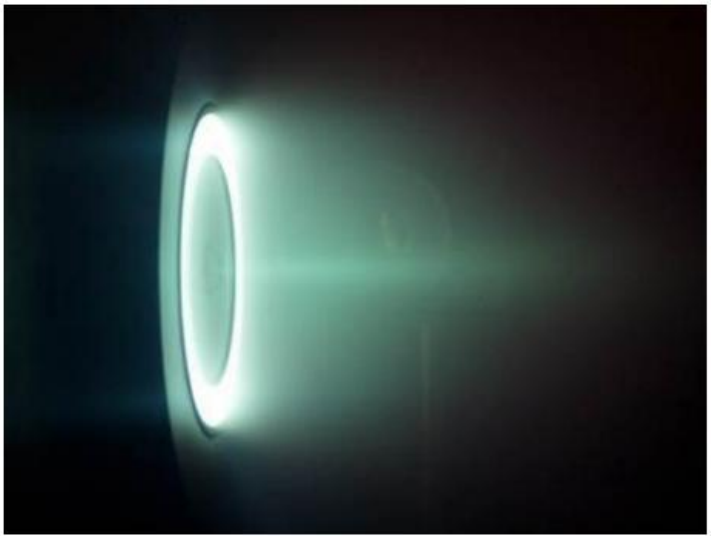

Figure 1.2 Picture of Hall thruster operation.

1.2.1 Principle of Operation

The Hall thruster's principle of operation is illustrated in Figure 1.3. Typically, the discharge channel has an annular shape, and radial magnetic field is imposed throughout the channel by a magnetic current. Because of this applied radial magnetic field, strong axial electric field is sustained throughout the discharge channel, rather than concentrated only on the near-electrode region due to the plasma Debye length. The electrons emitted from the cathode are trapped by the radial magnetic field due to the E×B drift. This azimuthal guiding center drift forms Hall current, which enables the heavy particle acceleration and thrust generation. The entrapped electrons are gradually accelerated toward the anode due to the diffusion, and ionize the propellant supplied through the anode. The ionized propellant are accelerated by the axial electric field and exhausted in high speed generating thrust. Different from ion thrusters, the ionization and ion acceleration area is not separated in Hall thrusters, and the quasi-neutrality is sustained throughout the discharge channel with the exception of sheath region. This feature enables Hall thrusters to achieve much higher thrust density than ion thrusters because the current density is not limited by the Child-Langmuir law. The cathode has the function of not only an electron source but also a neutralizer that the entire system is electrically neutralized by emitting excess electrons. It is to be noted that the exhausted propellant ion beam itself is not necessarily neutralized. In summary, the thrust of Hall thrusters is generated by the electric static acceleration of propellant, whereas the thrust is transferred to the thruster by electromagnetic force generated by the Hall current. This is why the Hall thrusters are classified to the electric static EP, though they have the features of electric magnetic EP at the same time.

There are three fundamental design criteria of Hall thrusters written as follows:

$$\omega_e \nu_{en} >> 1 \tag{1.3}$$

$$r_e << l << r_i \tag{1.4}$$

$$\lambda_n < l << \lambda_i \tag{1.5}$$

First, Eq.1.3 means the cyclotron frequency should be much higher than the collision frequency for electrons that the electrons should be well confinement by the applied magnetic field. Second, Eq. 1.4 indicates that only the electrons are trapped by the magnetic field but the ions are exhausted without suffering guiding center drift. Finally, Eq. 1.5 denotes that the neutral propellant should be efficiently ionized within the discharge channel, whereas the ions should be exhausted before they recombine with electrons. Generally, these three fundamental criteria are easily satisfied and more detailed considerations are necessary for actual Hall thruster design.

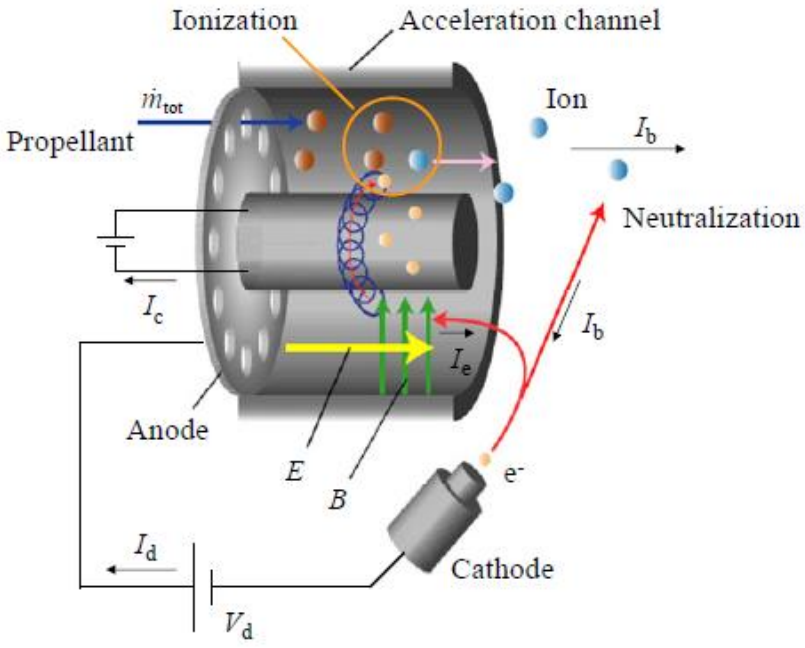

Figure 1.3 Principle of Hall thruster operation.

1.2.2 Type of Hall Thrusters

Hall thrusters are usually classified to two major types according to their acceleration mechanism [9]. One is called magnetic layer type represented by SPT (Stationary Plasma Thruster) series [10] first developed Morozov during 1960s, and the other is called anode layer type represented by TAL (Thruster with Anode Layer) series first developed by Zharinov [11]. The schematics of both thrusters are shown in Figure 1.3.

Magnetic layer type Hall thrusters have a dielectric ceramic discharge channel wall, usually Boron Nitride (BN). Dielectric wall sheath is formed at the vicinity of channel wall, and the electron wall loss is relatively high because of the secondary electron emission from the wall. This is the main energy loss mechanism of magnetic layer type Hall thrusters and thus, usually SPTs have relatively long channel length for sufficient propellant ionization because the electron temperature is regulated to low level. This is the major disadvantage of SPTs that the plasma inflow to the wall is intense which decreases the thrust performance and causes severe wall erosion [12]. On the other hand, the major advantage of SPTs is that their operation is very stable and has small discharge oscillation amplitude. Consequently, SPTs are the most developed and the most used Hall thrusters for satellite missions because of their reliability.

In comparison, anode layer type Hall thrusters have a metallic channel wall biased to cathode potential to minimize the electron wall loss. Thus, the electron temperature inside the TALs is usually much higher than that of SPTs [13], and the necessary channel length is accordingly shorter. There exists near anode electron sheath in TALs and the propellant acceleration inside this anode layer is significant, which is the reason why the TALs is called anode layer type. Naturally, the main energy loss mechanism of TALs is the high energy electron impingement to the anode. Compared with SPTs, the major advantage of TALs is that the plasma wall loss is significantly reduced that typically the thrust and lifetime performance of TALs are higher than that of SPTs. Unfortunately, the disadvantage of TALs is their large discharge oscillation and low operation stability, which results in the limited use of TALs for flight missions.

Figure 1.5 shows each thrust efficiency versus input power of SPT and TAL series [14] [15] [16] [17].

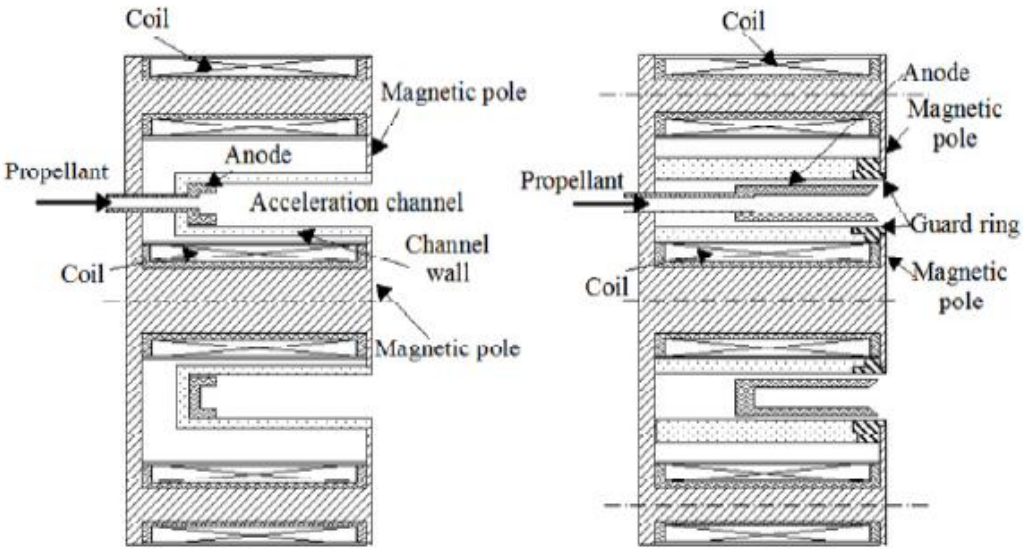

Figure 1.4 Magnetic layer type (left) and anode layer type (right) Hall thruster.

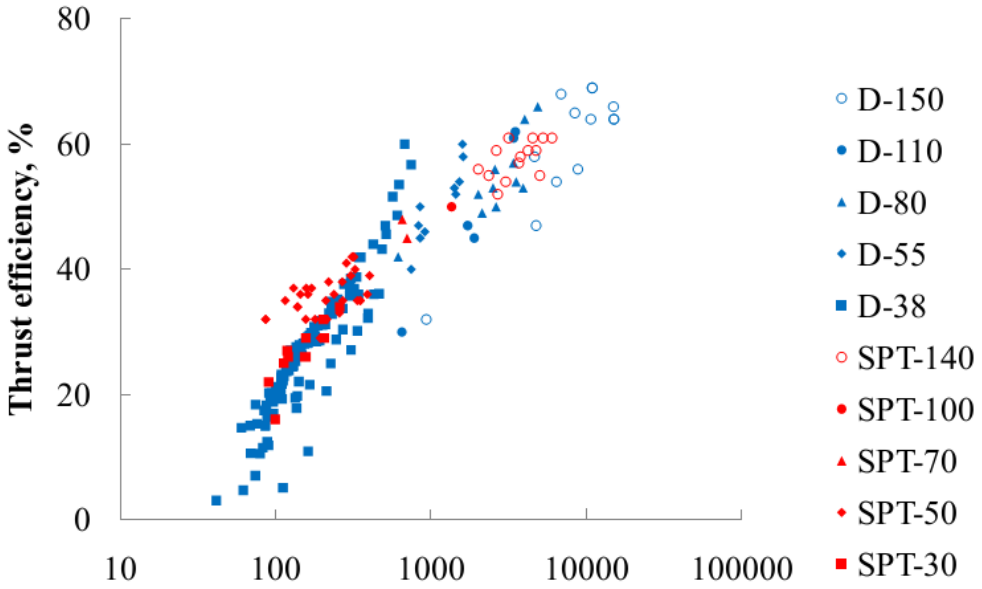

Figure 1.5 Thrust performance of SPT and TAL.

1.2.3 Performance Definition

In EPs, anode efficiency is as an important parameter as specific impulse in evaluating their performances. And this anode efficiency is represented by the product of propellant utilization efficiency, acceleration efficiency, and energy efficiency as shown in Eq. 1.6:

$$\eta_A = \eta_u \cdot \eta_a \cdot \eta_e \tag{1.6}$$

First, propellant utilization efficiency is defined as shown in Eq. 1.7, which shows the ratio of ion beam contributing to thrust to entire propellant flow rate which is current equivalent.

$$\eta_u \equiv \frac{m_i I_b}{e\dot{m}} \tag{1.7}$$

Considering the single ionization, $I_b = e\dot{m}_i / m_i$ thus $\eta_u = \dot{m}_i / \dot{m}$. That is the ratio of propellant extracted as ions to entire propellant mass flow rate. Propellant ionization occurs by the collision with electrons which have more than 12.13 eV energy, thus as electron density and electron temperature inside the channel are increased, propellant is ionized more easily, leading that propellant utilization efficiency is improved.

Second, acceleration efficiency is defined by Eq. 1.8, which shows the ratio of ion beam current contributing to thrust to entire discharge current.

$$\eta_a \equiv \frac{I_b}{I_d} \tag{1.8}$$

In anode layer thrusters, discharge current is dismantled as shown in Eq. 1.9. (Figure 1.5)

$$I_d = I_b + I_g + I_e \tag{1.9}$$

Except ion beam current, guard ring current and electron current cause the useless power consumption which does not contribute to thrust. Ion beam current is a current which is resulted by extracted ions toward outside of the channel as an ion beam. Guard ring current is a current which is resulted by neutralized ions by colliding with guard ring and receiving electrons. Because this is a current generated by the ions' collision with guard rings, it is desirable to reduce it as much as possible for also the sake of the reduction of wall erosion. And electron current is a current supplied from outside of the channel by the cathode, which much affected by the extent of confinement of electrons by magnetic field.

Finally, energy efficiency is defined by Eq. 1.10.

$$\eta_e = \frac{eF^2}{2m_i I_b^2 V_d} \tag{1.10}$$

Where, $F = m_i n_i \left\langle v_{iz}{}^2 \right\rangle S$, $I_b = e n_i \left\langle v_{iz} \right\rangle S$. So that can described as shown in Eq. 1.11

$$\eta_e = \frac{\frac{1}{2} m_i \left\langle v_{iz}{}^2 \right\rangle}{eV_d} \cdot \frac{\left\langle v_{iz}{}^2 \right\rangle}{\left\langle v_{iz} \right\rangle^2} \tag{1.11}$$

In addition, in case of $\left\langle v_{iz}{}^2 \right\rangle = \left\langle v_{iz} \right\rangle^2$, energy efficiency represents the ratio of mean axial kinetic energy by actually extracted ions to energy ions can receive by discharge voltage.

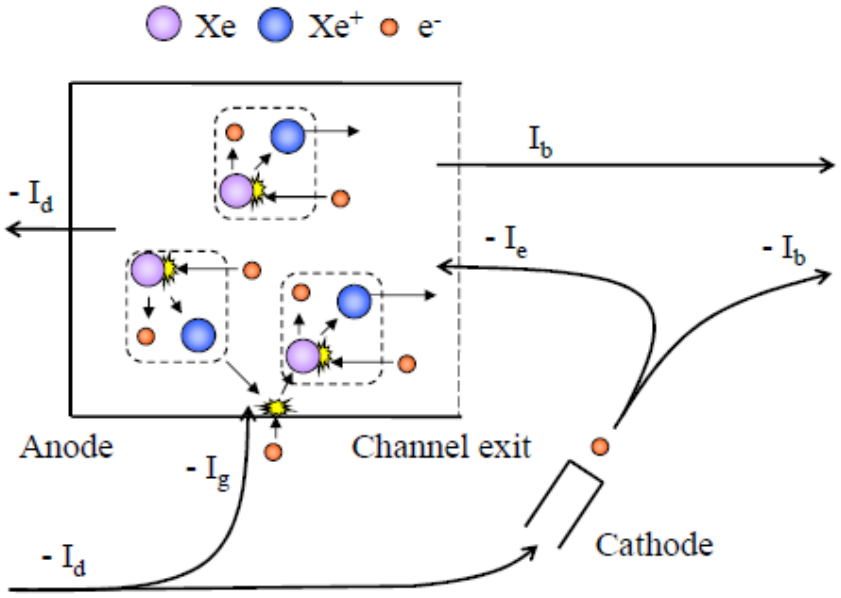

Figure 1.6 Definition of each current.

1.3 Application of Alternative Propellants to Hall Thrusters

Hall thrusters are developed using different propellant in different institutes and companies. NASA Glenn Research Center is researching krypton propellant [18] and Busek Co. is researching many kinds of propellants including light metals such as magnesium or zinc [19]. Table 1.1 shows physical and typical properties of each propellant, and Table 1.2 shows achieved thrust performance of each propellant. The first ionization energy versus atomic mass of propellant candidates and their typical thrust density versus specific impulse are shown in Figure 1.7 and Figure 1.8 respectively. The larger the atomic mass is, the more thrust will be achieved, and the smaller the atomic mass is, the more specific impulse will be achieved. It is, thus, clear that feasible thrust and specific impulse

vary by the difference in propellant. Currently, xenon is mainly used in Hall thrusters as a propellant due to its high thrust performance. However, its output on the Earth is tremendously little. Therefore, alternative propellant commands much attention which is more abundant like argon to achieve large space missions which requires much quantity of propellant. However, Table 1.2 and Figure 1.8 show that other propellants have not achieved enough thrust performance, especially up to 15 % of quite low anode efficiency with argon propellant. In addition, metal propellants have some problems that they are very instable or it is difficult to supply propellant to a thruster stably.

As missions of space development are increasing in number in recent years, more advanced missions can be achieved if the thrusters can change its operation mode as numerously as number of possible missions. Figure 1.8 shows that the thrusters can operate in higher specific-impulse regime by using argon as propellant instead of xenon. Thus, the necessity to develop a Hall thrusters using argon is given.

Table 1.1 Physical properties of each considerable propellant

	Kr	**I**	**Xe**	**Ar**	**Cs**	**Bi**	**Mg**	**Zn**	**Cd**	**Hg**
Atomic mass	83.8	126.9	131.3	39.9	132.9	209	24.3	65.4	112.4	200.6
First ionization energy (eV)	14	10.4	12.1	15.8	3.9	7.3	7.6	9.4	9	10.4
Freezing point (C^o)	-157	114	-112	-189	28	271	650	420	321	-39
Boiling point (C^o)	-153	184	-108	-186	658	1561	1095	907	767	357
Toxicity	None	Low/Med	None	None	Hazard	Low/None	Low	None	Hazard	Hazard
Cost per kg (Thousand yen)	24	39	91	4.7	5000	0.5	0.2	0.2	2	0.3
Domestic annual output (m^3)	-	-	8760	2.2×10^{14}	-	-	-	-	-	-

Table 1.2 Achieved thrust performance of each considerable propellant

	Kr	**I**	**Xe**	**Ar**	**Cs**	**Bi**	**Mg**	**Zn**	**Cd**	**Hg**
Isp	~4500	-	~3000	~1500	-	~2200	~3500	~3000	-	-
Thrust (mN)	~40	-	~60	22	-	~90	~30	40	-	-
Anode Efficiency (%)	~60	-	~70	~15	-	~60	~50	40	-	-

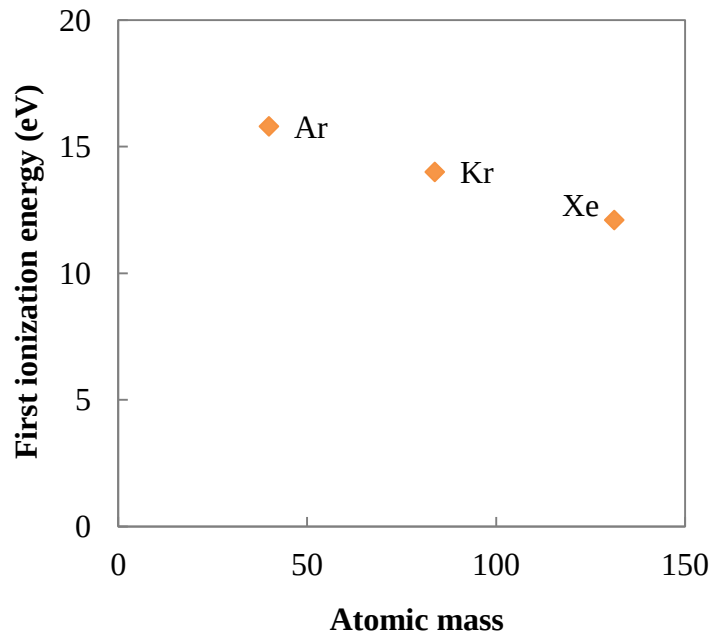

Figure 1.7 First ionization energy versus atomic mass of propellant candidates.

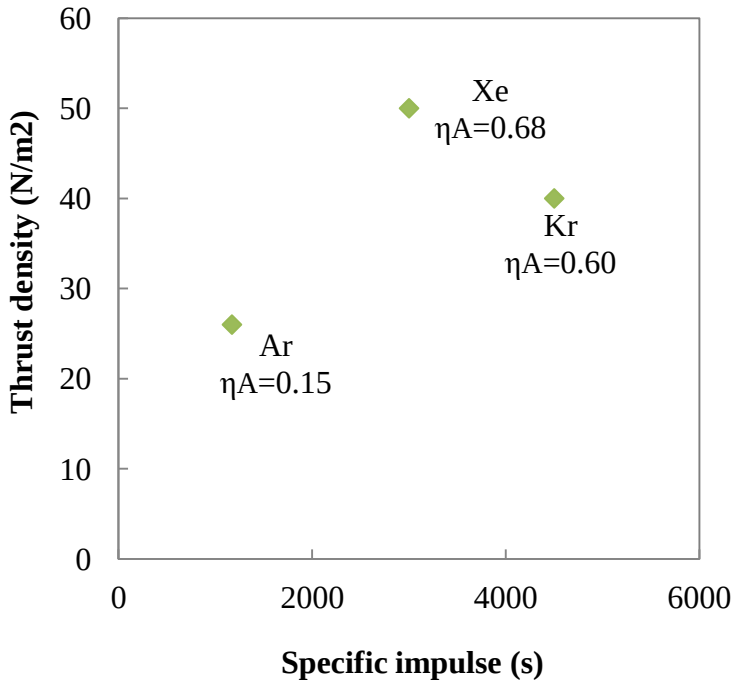

Figure 1.8 Achieved thrust density versus specific impulse of propellant candidates with each typical anode efficiency.

1.4 Japanese ‘In-Space Propulsion’

Currently, ISECG (International Space Exploration Coordination Group) established in 2007 draws up the next space exploration mission aiming at manned flight to Mars in the future, and the research and development of thrust bus-system to achieve these ‘In-space propulsion’ all over the world. In Japan, JAXA shows the development roadmap shown in Figure 1.9 and many thrust system are considered to be candidates to achieve this roadmap [20]. Especially, Hall thruster commands much attention because of its reliability, high thrust density and high specific impulse. To conduct research and development of Hall thrusters efficiently by all Japan system, project ‘RAIJIN (Robust Anode layer Intelligent Japan IN-space propulsion system)’ was established in 2012. The concept of this project is shown in Figure 1.10. This project contains research and development of thruster head and PPU, interference of plume and mountability, high current neutralizer, mission, orbit analysis, and industrialization. In this study, selection of propellant and high specific impulse shown in the roadmap are focused, and research and development of new anode layer thruster head are conducted along project RAIJIN [21] [22].

Results of calculations show that the entire cost of transportation will be reduced to 300 B YEN from 1 T YEN in case that argon is used as propellant for transportation of SPS from LEO to GEO instead of xenon. In that paper, thruster with argon propellant will be advantageous rather that xenon propellant in terms of transportation cost if it has more than 15 % of anode efficiency [23].

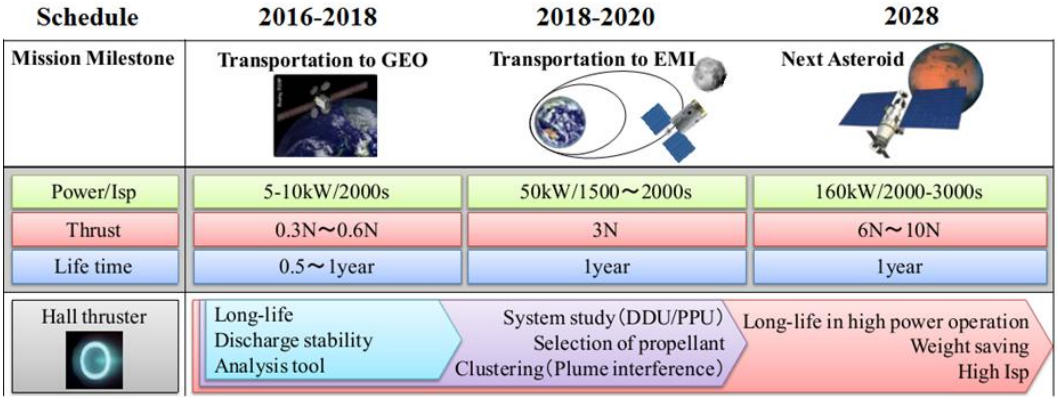

Figure 1.9 Development roadmap for next space exploration shown by JAXA.

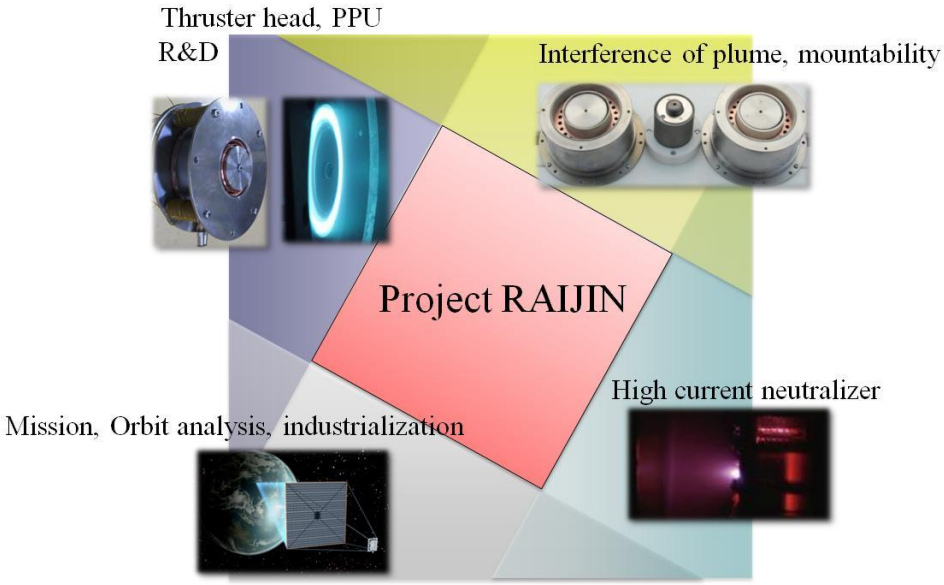

Figure 1.10 Concept of project 'RAIJIN'.

1.5 Dissertation Goals

The final goals of this dissertation are as:

1. Achieve high anode efficiency with argon thruster, and show predominance over other propellant candidates
2. Uncover the operation characteristics and detect optimal operation regime of argon anode layer Hall thrusters
3. Construct a scaling law only for argon anode layer Hall thrusters.

In order to accomplish the final goals, we conducted our research in three steps: First, develop a 1.0 to 2.0 kW class new anode layer Hall thruster from the scaling law of xenon thrusters; Second, operate the new thruster not only with xenon propellant but also argon propellant and uncover the operation characteristics with argon propellant comparing to those with xenon propellant; Third, get the design guideline only for argon anode layer thruster using experimental results.

In this research, the operation characteristics of an argon anode layer Hall thruster are shown which was newly developed. After discussions of the results for xenon and argon propellant, scaling model for argon anode layer Hall thruster is shown. This research will be used as a first step to develop high-power argon anode layer Hall thruster in the near future to achieve those missions in JAXA's roadmap.

Chapter 2

Operation Characteristics of Anode Layer Hall Thrusters and Discharge Current Oscillation

2.1 Input Power and Anode Efficiency

Generally, anode efficiency is improved as input power is increased in anode layer Hall thrusters [24]. As the propellant mass flow rate is increased, density of neutral particles is increased, which results in efficient ionization of propellant. In other words, propellant utilization efficiency is improved. Further, as the discharge voltage is increased, electron energy is increased which leads that propellant utilization efficiency is improved.

Figure 2.1 shows the thrust performance of an anode layer type Hall thruster, UT-60 of the University of Tokyo [25]. Anode efficiency of 53 % is achieved with the input power of 1700 W, leading to specific impulse of 2000 s. It is indicated that anode efficiency is improved as the input power is increased. At the same time, the specific impulse is improved as the discharge voltage is increased.

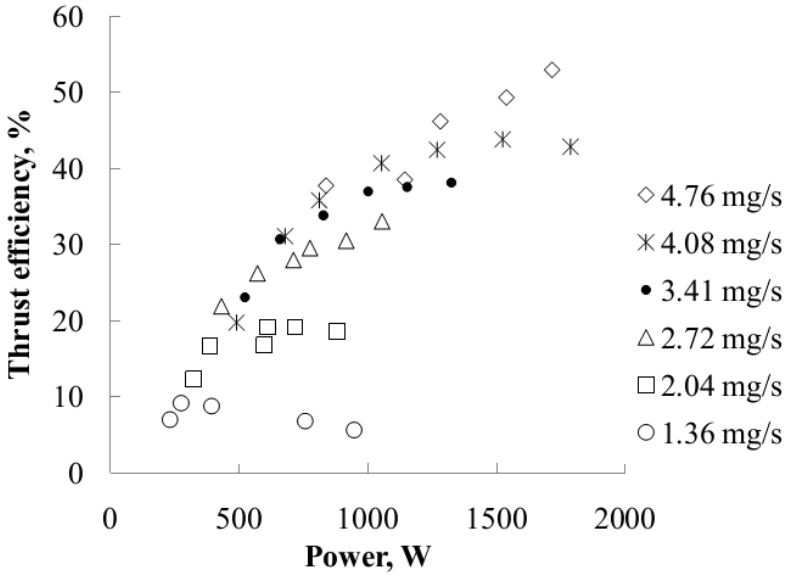

Figure 2.1 Anode efficiency versus input power of an anode layer Hall thruster in the University of Tokyo.

2.2 Discharge Current Oscillation in Hall Thrusters

2.2.1 Oscillation Amplitude of Discharge Current

Because discharge current oscillation intensively affects on Hall thruster operation, its amplitude is quite important. In this research, the oscillation amplitude of discharge current is defined as follows:

$$\Delta \equiv \frac{1}{\bar{I}_d}\sqrt{\frac{\int_0^\tau \left(I_d - \bar{I}_d\right)^2 dt}{\tau}}, \left(\bar{I}_d = \frac{\int_0^\tau I_d dt}{\tau}\right) \tag{2.1}$$

In SMART-1 mission, I_d =4.28 A versus oscillation amplitude $\Delta \approx 0.23$ [6]. Therefore, it can perfume a mission that operation points which meet $\Delta < 0.2$, such points are defined as stable operation regime in this research.

Operation characteristics of Hall thrusters are determined by propellant flow rate, discharge voltage, and magnetic flux density. Particularly, they are much affected by magnetic flux density in the operation regime where anode efficiency is high. Figure 2.2 shows the operation characteristics of UT-60 anode layer Hall thruster in the University of Tokyo [26]. The abscissa of each figure shows the magnetic flux density at the channel exit. In region (I), electrons are likely to flow into the anode due to the insufficiency of the confinement of electrons, which results in large discharge current. In region (II), oscillation of discharge current becomes higher and the thruster cannot be operated stably though discharge current becomes smaller. With higher magnetic flux density, the decreasing ratio of discharge current does not follow $1/B^2$, that can be thought the transition to anomalous diffusion in region (III). In this transition region, the discharge is stable.

In region (I), the anode efficiency is small due to large discharge current though the oscillation amplitude is small. And region (III) is quite narrow of 44 mT – 48 mT though the oscillation amplitude is small and anode efficiency is high. Because Hall thrusters premise several thousand hours operation, the thrust performance is thought changeable according to the operation time. Consequently, it is desirable that the stable operation regime is as wide as possible.

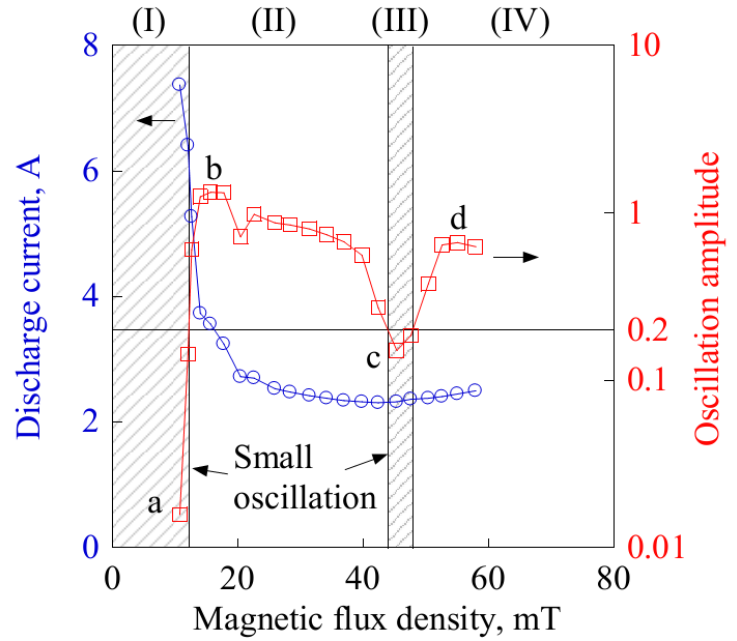

(a) Discharge current and its oscillation amplitude.

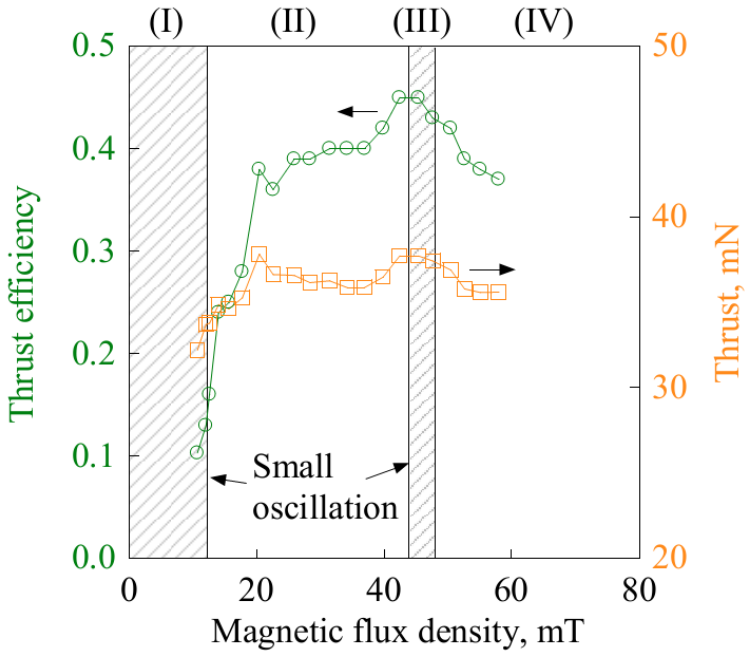

(b) Anode efficiency and thrust.

Figure 2.2 Operation characteristics of UT-60:
V_d=250 V, $\dot{m}$=2.73 mg/s.

2.2.2 Mechanism of Ionization Oscillation in Hall Thrusters

Ionization oscillation is considered to occur as follows. The concept of ionization oscillation is shown in Figure 2.3 [27] [28], and typical discharge oscillation history is shown in Figure 2.4.

<Step 1>

In case that electrons generated in ionization are prevented from flowing into the anode, for example, that velocity of electrons is very small, electron density increases there, which leads ionization collision to increase. This provokes sharp acceleration of ionization because electron density increases more.

<Step 2>

Density of neutral particles decreases because of ionization acceleration of ions. The number of neutral particles in the entire channel decreases immediately because suddenly increased electrons flows into the anode.

<Step 3>

After the number of neutral particles in the channel, frequency of ionization decreases and generation rate of electrons decreases. Consequently, although density of neutral particles gets to recover, electron density decreases in advance because velocity of neutral particles is quite smaller than that of electrons.

<Step 4>

Density of neutral particles recovers from the anode side. That at the channel exit keeps small until neutral particles fill the entire channel. Because electrons flow into the anode side by the collision with neutral particles, electrons hardly flow into the channel until density of neutral particles at the channel exit recovers. In other words, the condition that electrons hardly flow into the channel keep for a while, which allows neutral particles to fill the entire channel, and goes back to Step 1. After neutral particles fill the channel, electrons are induced into the channel and ionization collision occurs again.

This repetition of ionization acceleration phase and density recovery of neutral particles phase is considered to be the ionization oscillation. Because in ionization acceleration phase, neutral particles in the channel ionize at one time, quite high current flows.

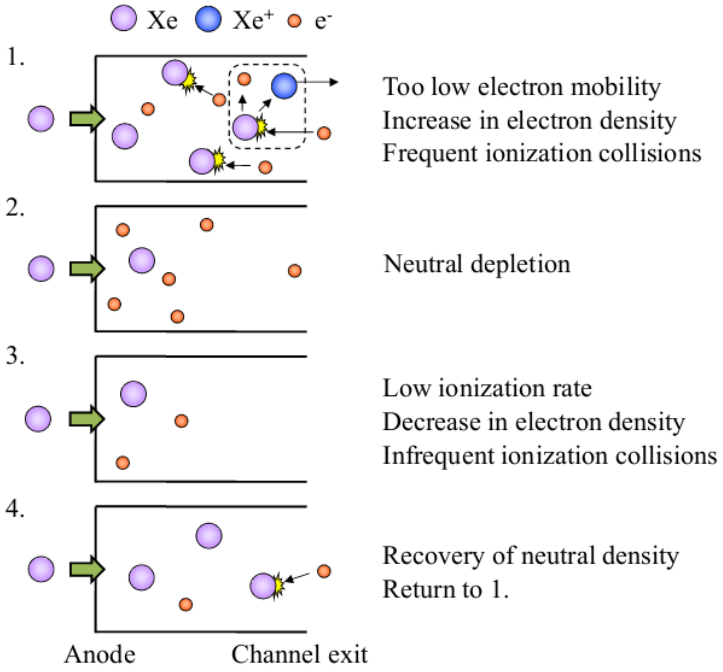

Figure 2.3 Concept of ionization oscillation.

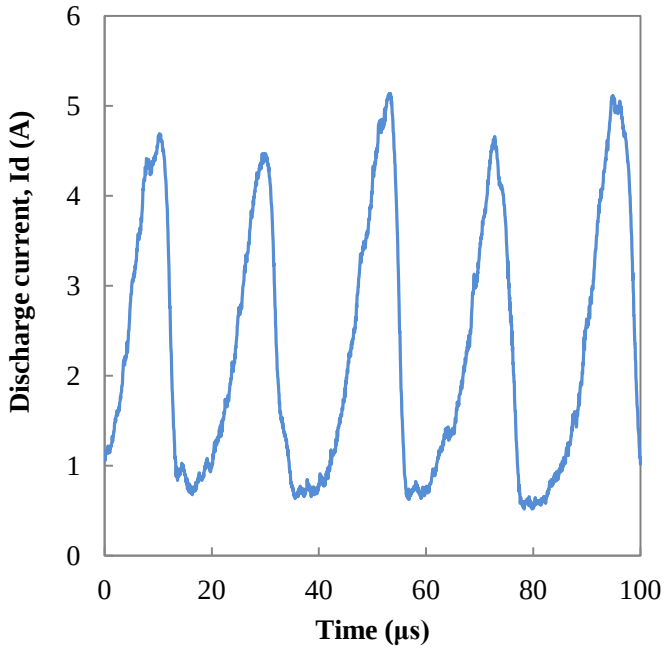

Figure 2.4 Typical discharge current oscillation of UT-58 (V_d=250 V, Q= 2.0 Aeq, I_c= 2.0 A).

2.3 Operation Characteristics of Hall Thrusters with Argon Propellant

Figure 2.5 shows the operation region of UT-38 anode layer Hall thruster in the University of Tokyo. It could not be operated on the quite limited regime where magnetic flux density of 2.7 mT to that of 5.2 mT.

Figure 2.6 shows the anode efficiency versus input power of SPT type-93 in the University of Tokyo with argon propellant [29].

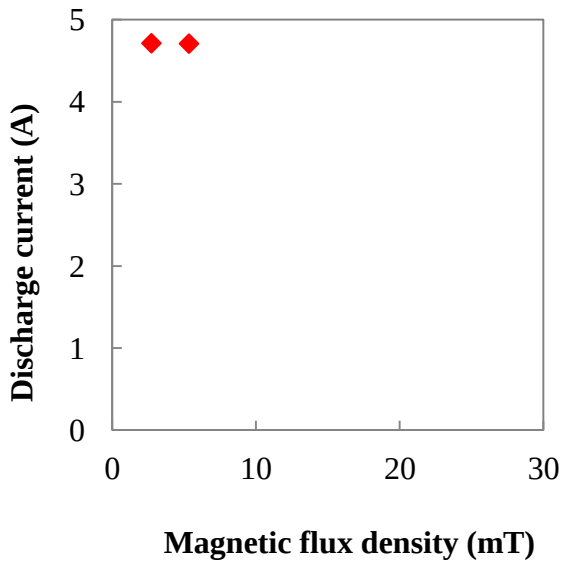

Figure 2.5 Small operation region of UT-38 anode layer Hall thruster.

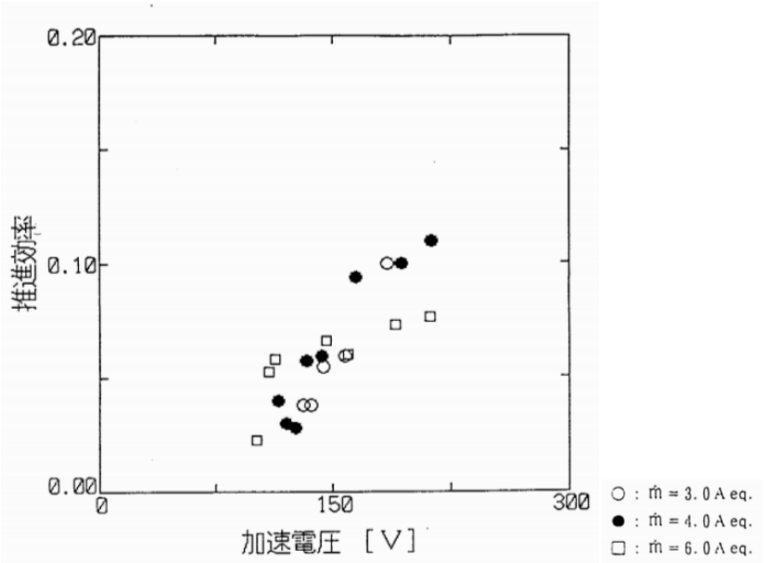

Figure 2.6 Anode efficiency versus discharge voltage of SPT type-93 in the University of Tokyo.

2.4 Theory of Ionization Oscillation and Electron Diffusion in Hall Thrusters

Electron density or energy is intensively related to the ionization of propellant and hence electron's motion plays a very important role in Hall thruster operation. First of all, focused is put on the each electron mean free path. The mean free path of electron is described as:

$$\lambda_m = \frac{v_e}{\nu_{en}} = \frac{1}{n_n \cdot \sigma} \tag{1.12}$$

Further, the flow rate of neutral particle is described as:

$$Q = n_n \cdot v_n \cdot S = n_n \cdot \sqrt{\frac{3k_B T_n}{m_n}} \cdot S \tag{1.13}$$

Using Eq. 1.12 and Eq. 1.13 can be described as:

$$\lambda_m = \frac{S}{Q \cdot \sigma} \cdot \sqrt{\frac{3k_B T_n}{m_n}} \tag{1.14}$$

Next electron's motion is considered which diffuses by the confinement by the magnetic field and the collision with neutral particles. Considering the collision between electrons and neutral particles as a loss of momentum and neglecting the collision between electrons and ions because of its quite small collision frequency, the diffusion equation of electrons is described as follows:

$$m_e n_e \left[\frac{\partial v_e}{\partial t} + (v_e \cdot \nabla) v_e \right] = -e n_e (E + v_e \times B) - \nabla (n_e k_B T_e) - m_e n_e v_e \nu_{en} \tag{1.15}$$

Considering that the collision frequency between electrons and neutral particles ν_{en} $(= n_n \langle \sigma v_e \rangle_{T_e})$ is very large, and assuming that it is possible to neglect the time differentiation term and convection differentiation term in the left side of the equation, the electron velocity which is perpendicular to magnetic lines $v_{e\perp}$ is described as follows,

$$v_{e\perp} = -\mu_\perp \left[E + \frac{\nabla (n_e k_B T_e)}{e n_e} \right] + \frac{E \times B}{B^2} + \frac{\nabla (n_e k_B T_e) \times B}{e n_e B^2} \tag{1.16}$$

$\mu_\perp$ is called electron mobility which is defined as follows:

$$\mu_\perp \equiv \frac{1}{1 + (\omega_{ce} / \nu_{en})^2} \frac{e}{m_e \nu_{en}} \tag{1.17}$$

In Hall thrusters, $\omega_{ce}\tau_{en} \approx 100$ generally, and in case of $\omega_{ce}\tau_{en} >> 1$ and using Eq. 1.12, $\mu_\perp$ is described as follows:

$$\mu_\perp \approx \frac{m_e \nu_{en}}{eB^2} = \frac{m_e v_e}{eB^2 \lambda_m} = \frac{m_e v_e}{eB^2} \frac{Q\sigma}{S} \sqrt{\frac{m_n}{3k_B T_n}} \tag{1.18}$$

Assuming azimuthal uniformity by the axial symmetry of Hall thrusters, axial velocity of electrons $-v_{ez}$ is expressed as follows:

$$-v_{ez} = -\frac{m_e \nu_{en}}{eB^2} \left[E_z + \frac{1}{e n_e} \frac{\partial}{\partial z} (n_e k_B T_e) \right] = -\frac{m_e v_e}{eB^2} \frac{Q\sigma}{S} \sqrt{\frac{m_n}{3k_B T_n}} \left[E_z + \frac{1}{e n_e} \frac{\partial}{\partial z} (n_e k_B T_e) \right] \tag{1.19}$$

As is shown in this equation, $-v_{ez}$ is proportional to B^{-2} and ν_{en}. The reason why the first term

is proportional to ν_{en} is explained as: $E \times B$ drifting electrons by E_z and B_r lose almost all their kinetic energy by the collision with neutral particles. When non-energy electrons resume $E \times B$ drifting, the first velocity is given by E_z. Therefore, the center of drift circling moves to the anode with the velocity proportional to ν_{en}.

$-\nu_{ez}$ in Hall thrusters does not meet Eq. 1.19, and it indicates the higher value than that given by Eq. 1.19. This phenomenon is called Anomalous diffusion, and the relation between electron mobility and magnetic flux density changes into that shown as:

$$\mu_{\perp} = k\frac{1}{B} \quad (k : \text{proportionality constant}) \tag{1.20}$$

This phenomenon is observed not only in Hall thrusters but also confinement of plasma by magnetic field, and it was reported by Bohm et al. first [30]. Bohm et al. derived the experimental equation, $k = 1/16$ in Eq. 1.20. This equation corresponds to experimental values very well, so the diffusion which meets Eq. 1.20 is called Bohm diffusion.

Figure 1.6 shows the transform of diffusion constant $D_{\perp}\left(= k_B T_e \mu_{\perp} / e\right)$ versus B derived by the experiment using an anode layer type Hall thruster by N.Yamamoto et al. [26] [27]. It is indicated that $D_{\perp}$ transforms to anomalous diffusion which is proportional to $1/B$ from classical diffusion which is proportional to $1/B^2$.

There exists several theories concerning anomalous diffusion, and some kinds of research are conducted now. In Hall thrusters, mainly 2 points as follows or more are considered to be the cause [31] [32]:

1. Effect by wall
2. High frequency azimuthal drift waves

Tamida et al. discovered the relation between the oscillation amplitude and electron diffusion by focusing on the mobility of electrons [33] [34] [35] [36]. Figure 1.7 shows the typical tendencies of discharge current and oscillation amplitude of discharge current versus magnetic flux density. The discharge current oscillation can be roughly classified into three diffusion modes, those are classical diffusion region (C), transition region (T), and anomalous diffusion region (A). In classical diffusion region, the confinement of electrons increases as magnetic flux density increases, so the discharge current decreases following the classical diffusion of electrons. In transition from classical to anomalous diffusion, very severe oscillations are typically observed. In the anomalous diffusion region, however, the oscillations are relatively small. They classified electron diffusion modes using the parameter of electron velocity of the channel exit. Assuming that electron number density, electron temperature, electron velocity, and temperature of neutral particles at the channel exit are constant, and that electric field intensity at the channel exit is proportional to the discharge voltage in Eq.1.19, the electron velocity at the channel exit is described as:

$$-v_{ez,exit} \propto \frac{Q \cdot \sqrt{m_n} \cdot \sigma \cdot V_d}{B^2} \tag{1.21}$$

Electron velocity at the channel exit depends on propellant flow rate, mass of propellant, cross section of collision between electrons and neutral particles, and discharge voltage regardless of kinds of propellants. In this research, oscillation characteristics of two kinds of plasma (xenon and argon) are discussed using this parameter of electron velocity at the channel exit.

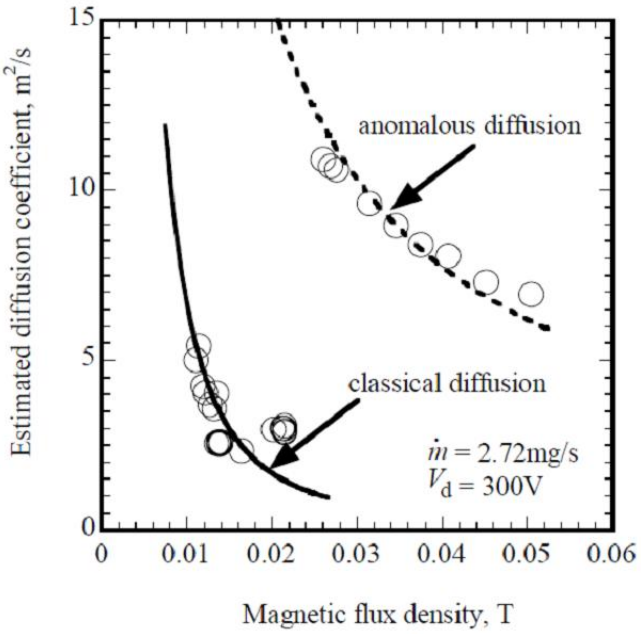

Figure 2.7 Transition of diffusion coefficient versus magnetic flux density (N.Yamamoto et al.) :

Anode layer type, hollow anode D8Z3, V_d =300 V, $\dot{m}$ =2.72 mg/s.

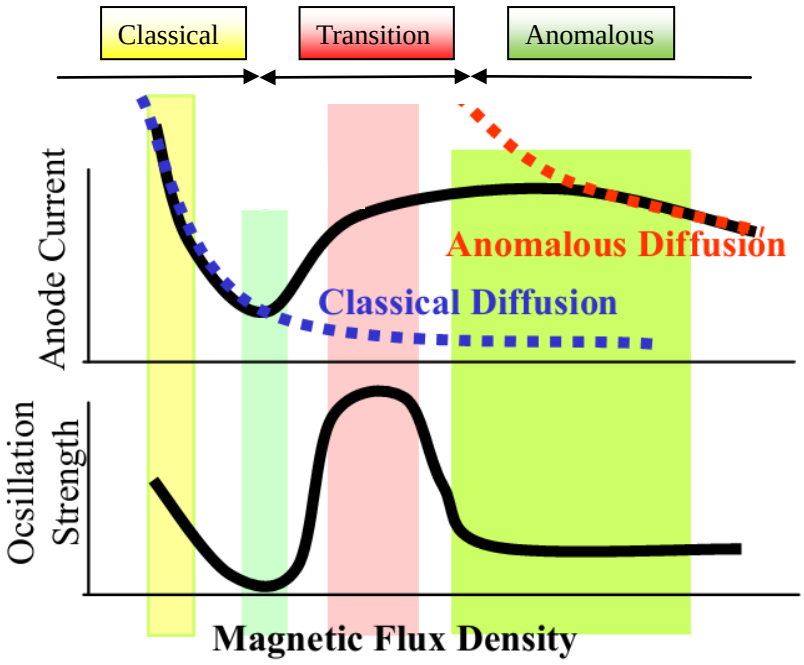

Figure 2.8 Typical tendencies of discharge current and oscillation amplitude versus magnetic flux density and three electron diffusion modes.

Chapter 3

Designing of UT-58 Anode Layer Type Hall Thruster

3.1 Designing Procedure

Tommaso Misuri et al. developed analytical scaling model coupled with a statistical database defining the opportunity of a wide and more flexible way of scaling Hall thruster in order to follow different design requirements. They focused on the scaling methodology applied to a high power Hall thruster and aim to provide different design options for high-power class of thrusters [37].

In this research, a reference thruster, UT-55 anode layer thruster was chosen as the first step. Second, in order to determine the very fundamental five values, mean diameter of channel, channel height, channel length, discharge voltage, and propellant particle density, the supposed input power and anode efficiency were picked up. Third, the five fundamental values were determined by following the elemental physical equations using the values of the reference thrusters. Fourth, magnetic circuits were designed to fill our requirements using argon propellant. Fifth, a heat flux transfer simulation was conducted and temperature profile of the thruster was discovered, to meet the heat proof temperature of each material, especially the inner coil wire. Finally, several divices are worked out and the global structure was determined.

3.1.1 The Reference Thruster

In dealing with a scaling method, the very first step is to choose a reference thruster. In the University of Tokyo, we have chosen the UT-55 anode layer thruster, which is the one that best suits our needs, which has a large database regarding its thrust performance with xenon propellant. The table below shows the parameters of interest at the desired operating point for our reference thruster, and the cross section drawing is shown in Figure 3.1. All the other quantities will be evaluated in this chapter next by this group of parameters using appropriate physical relations.

Table 3.1 Important parameters and specifications of UT-55.

Parameters	Values	Unit of measure
d_{ref}	55	mm
b_{ref}	7	mm
L_{ref}	3	mm
V_{d_ref}	250	V
I_{d_ref}	2.32	A
P_{ref}	580	W
$\dot{m}_{ref}$	2	Aeq
ε_{w_ref}	0.263	n.d.
ε_{a_ref}	0.06	n.d.
ε_{i_ref}	0.168	n.d.
F_{ref}	38	mN
I_{sp_ref}	1400	s
η_{A_ref}	0.45	n.d.

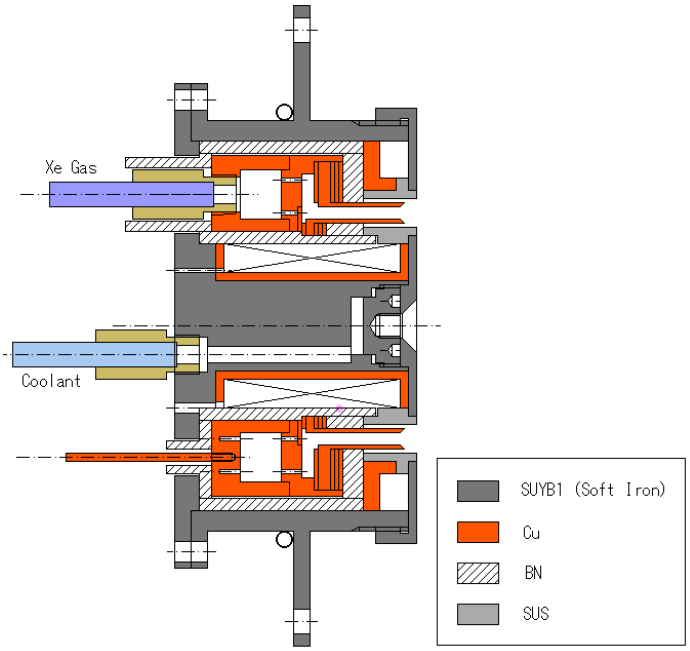

Figure 3.1 Cross-section drawing of UT-55 anode layer thruster.

3.1.2 Fundamental Parameters

They have chosen a group of fundamental parameters which can be independently tailored in the preliminary design plane. All the scaling relations that will be presented in the next paragraph will depend on these fundamental parameters. The chosen parameters are the following ones:

1) d channel mean diameter
2) b channel height
3) L channel length
4) V_d discharge voltage
5) n_n propellant particle density in the injection plane

They have then a total of five parameters, the first three of them describing the geometry of the scaled thruster. Knowing their values, all the other data of interest can be described by means of the physical equations governing the acceleration process inside a Hall thruster.

3.1.3 Fundamental Physical Relations for Hall Thruster Scaling

Some basic relations that allow us to obtain the thruster performance starting from the five fundamental parameters are now introduced. From the knowledge of previous five parameters and of the reference thruster data, we can calculate all the other meaningful functioning parameters. As a first step, the total discharge current is evaluated as:

$$I_d \propto \dot{m} \propto n_n \cdot e \cdot v_n \cdot d \cdot b \;\Rightarrow \frac{I_d}{I_{d_ref}} = \frac{n_n}{n_{n_ref}} \cdot \frac{d}{d_{ref}} \cdot \frac{b}{b_{ref}} \tag{3.1}$$

The Hall thruster's input power is:

$$P = I_d V_d \;\Rightarrow\; \frac{P}{P_{ref}} = \frac{n_n}{n_{n_ref}} \cdot \frac{d}{d_{ref}} \cdot \frac{b}{b_{ref}} \cdot \left(\frac{V_d}{V_{d_ref}} \right)^{1/2} \tag{3.2}$$

The thruster global anode efficiency, η_A, can be described as:

$$\eta_A = \eta_{losses} \cdot \eta_I \cdot \eta_{vel} \cdot \eta_\varphi \cdot \eta_m \tag{3.3}$$

The latter four efficiency factors keep into account losses due to the electron current (η_I), the spread velocity loss (η_{vel}), the beam divergence loss (η_φ), and losses due to presence of neutral particles in the beam (η_m). They are usually considered constant and for them we have assumed the following values [38]:

$$\eta_I = 0.81 \quad \eta_{vel} = 0.95 \quad \eta_\varphi = 0.95 \quad \eta_m = 0.98 \tag{3.4}$$

And the first loss factor η_{losses} takes into account the effect of the wall losses [39], the anode sheath losses and of the energy lost for the ionization process. Its expression is the following one:

$$\eta_{losses} = 1 - \varepsilon_w - \varepsilon_a - \varepsilon_i \tag{3.5}$$

Where $\varepsilon_w, \varepsilon_a, \varepsilon_i$ can be evaluated with their scaling model (since their values are known for the reference thruster):

$$\varepsilon_{\mathrm{w}} \propto \frac{T_e^{3/2} \cdot n \cdot d \cdot L}{P} \Rightarrow \frac{\varepsilon_{\mathrm{w}}}{\varepsilon_{\mathrm{w_ref}}} = \frac{L}{L_{ref}} \cdot \left(\frac{V_d}{V_{d_ref}} \cdot \frac{b}{b_{ref}} \right)^{-1} \tag{3.6}$$

$$\varepsilon_{\mathrm{a}} \propto \frac{T_e^{3/2} \cdot n \cdot d \cdot b}{P} \Rightarrow \frac{\varepsilon_{\mathrm{a}}}{\varepsilon_{\mathrm{a_ref}}} = \left(\frac{V_d}{V_{d_ref}} \right)^{-1} \tag{3.7}$$

$$\varepsilon_{\mathrm{i}} \propto \frac{\dot{m}}{P} \Rightarrow \frac{\varepsilon_{\mathrm{i}}}{\varepsilon_{\mathrm{i_ref}}} = \left(\frac{V_d}{V_{d_ref}} \right)^{-1} \tag{3.8}$$

Total mass flow rate can be described as:

$$\dot{m}_{tot} = \frac{\dot{m}_i}{\eta_m} \tag{3.9}$$

Total thrust:

$$F = \dot{m}_i \cdot v_i \tag{3.10}$$

Effective exhaust velocity and specific impulse:

$$I_{sp} = \frac{v_{eff}}{g} \Rightarrow v_{eff} = \frac{F}{\dot{m}_{tot}} = \eta_m v_i \tag{3.11}$$

3.2 Assuming Specification of UT-58 Anode Layer Hall Thruster

As a first step to determine the assuming specification of a new thruster, the input power and discharge voltage was determined. By the limit of the PPU system in our laboratory, the discharge voltage was up to 400 V, and we aimed at achieving the highest thrust performance in our laboratory, we set the input power and propellant mass flow rate 1500 W and 3.0 Aeq respectively. And total anode efficiency was assumed to be more than 60 %.

By using the following equations, the assumed specifications of a new thruster were determined as shown in Table 3.2.

$$\frac{F}{F_{ref}} = \frac{\dot{m}_i v_i}{(\dot{m}_i v_i)_{ref}} \propto \frac{n}{n_{ref}} \left(\frac{V_d}{V_{d_ref}} \right)^{1/2} \tag{3.12}$$

$$\frac{I_{sp}}{I_{sp_ref}} = \frac{v_{eff}}{v_{eff_ref}} \propto \left(\frac{V_d}{V_{d_ref}} \right)^{1/2} \tag{3.13}$$

In order to meet these specifications, the geometric and other parameters were determined since the next paragraph.

Table 3.2 Assumed specifications of a new thruster.

Parameters	Values	Unit of measure
V_d	400	V
P	1700	W
$\dot{m}$	3	Aeq
ε_w	0.096	n.d.
ε_a	0.038	n.d.
ε_i	0.105	n.d.
F	71.8	mN
I_{sp}	1770	s
η_A	0.673	n.d.

3.3 Geometric Structure

In order to determine the geometric structure, we set some qualifications from the previous assumed specification of a new thruster. The first one is from the input power of 1700 W. The following condition can be described:

$$\frac{P}{P_{ref}} = \frac{1700}{580} = \frac{V_d}{V_{d_ref}} \frac{n_n}{n_{n_ref}} \frac{d}{d_{ref}} \frac{b}{b_{ref}} \Rightarrow \frac{d}{d_{ref}} \frac{b}{b_{ref}} = 1.22 \tag{3.14}$$

The second one is from the global anode efficiency of more than 60 %. The following condition can be described using from Eq. 3.3 to 3.8 and the values of the reference thruster:

$$\eta_A = \eta_{losses} \cdot \eta_{vel} \cdot \eta_{\varphi} \cdot \eta_m > 0.6 \Rightarrow \eta_{losses} = 1 - \varepsilon_w - \varepsilon_a - \varepsilon_i > 0.678 \tag{3.15}$$

$$\therefore\ \eta_{losses} = 1-\varepsilon_w-\varepsilon_a-\varepsilon_i = 1-\left(\frac{V_d}{V_{d_ref}}\right)^{-1}\left[\frac{L}{L_{ref}}\left(\frac{b}{b_{ref}}\right)^{-1}\varepsilon_{w_ref}-\left(\varepsilon_{a_ref}+\varepsilon_{i_ref}\right)\right] > 0.678 \tag{3.16}$$

$$\Rightarrow\ \frac{L}{L_{ref}}\left(\frac{b}{b_{ref}}\right)^{-1} < 0.708$$

By Eq. 3.14 and 3.16, d, b, L were determined as:

$$d = 58, \quad b = 8, \quad L = 2 \tag{3.17}$$

3.4 Magnetic Circuit with Magnetic Shielding System

Magnetic circuit is composed of electromagnetic soft iron poles made of SUYB1. One of iron poles are positioned in the center axis, and four are positioned in the outer. Each iron pole has 160 turns and 320 turns of ceramic insulated wire, CEW, respectively. The inner coil and outer coils are connected directly, and the same current is flowing to all coils. A radial magnetic field is applied to the discharge channel by inner and outer solenoid coils. Now, the researches concerning erosion-less thruster by magnetic shielding system are conducted all over the world [40] [41] [42]. The magnetic shielding system is installed to UT-58 around the hollow anode. The width of magnetic pole piece can be adjusted to apply the different shape of magnetic field lines (Figure 3.2). When a larger thruster is designed, the width of pole piece will increase according to the mean diameter of acceleration channel. Figure 3.3 and Figure 3.4 shows the shape of magnetic lines of UT-58 whose widths between pole pieces are 19 mm and 24 mm respectively, and Figure 3.5 shows the axial distribution of magnetic flux density of each magnetic field configuration. Figure 3.5 shows that if the width between pole pieces is increased, the peak value of magnetic flux density decreases. Additionally, in case of using wider gap between pole pieces, a more ideal shape of magnetic field lines is achieved. This is, many of them can escape from entering into the guard ring and the peak value is located outside of the channel as shown in Figure 3.6. This means that the ionization region is pushed downstream and out of the channel leading less erosion of the channel walls. Using argon propellant, we aim at achieving the optimal conditions that operating points are located in the regime where magnetic flux density is as small as possible. The magnetic type of Figure 3.4 is more ideal one than that of Figure 3.2 and 3.3 in terms of that shape, but it can achieve only 33 mT at peak value of the axial distribution of magnetic flux density when the coil current is 3.0 A. On the other hand, the magnetic type of Figure 3.2 can achieve more than 60 mT at peak value of the axial distribution of magnetic flux density when the coil current is 3.0 A. So in this research, we fixed magnetic shielding type to Figure 3.2 in order to achieve wider magnetic flux range with argon

propellant. At peak value, the magnetic flux density is 63 mT at 3 A of coil current. In calculating the magnetic field configuration and the intense of the magnetic flux density, the software of FEMM was used.

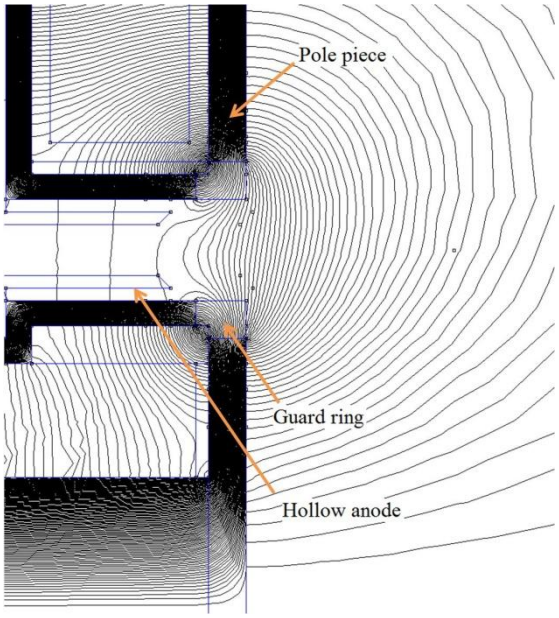

Figure 3.2 Magnetic field configuration (Gap = 14).

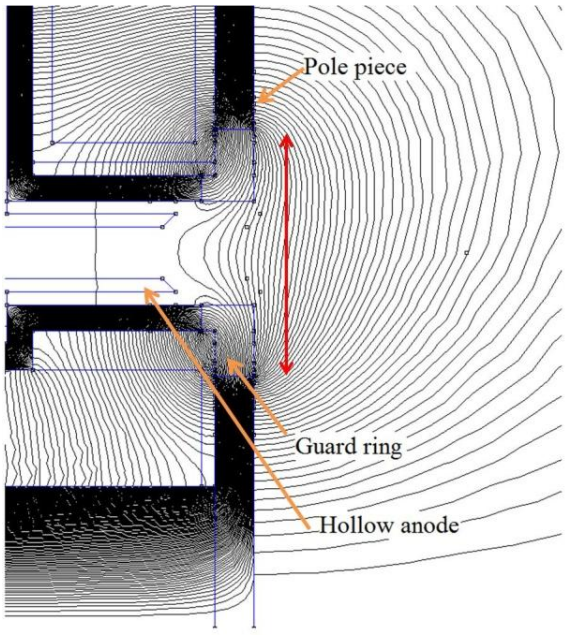

Figure 3.3 Magnetic field configuration (Gap = 19).

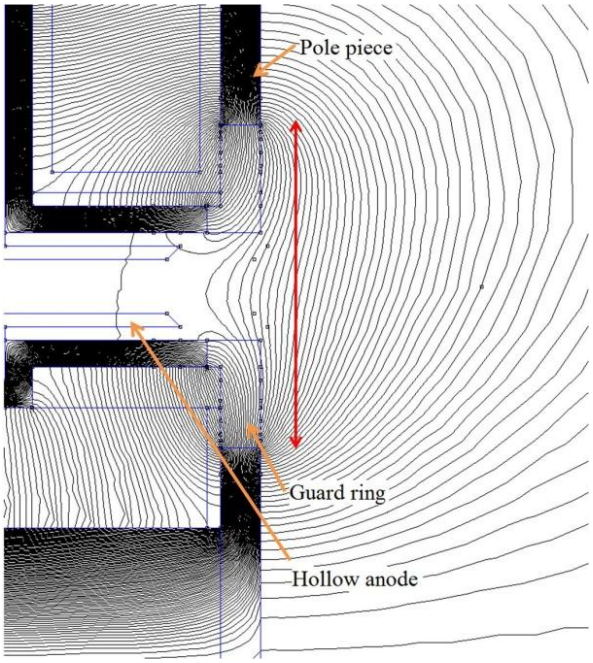

Figure 3.4 Magnetic field configuration (Gap = 24).

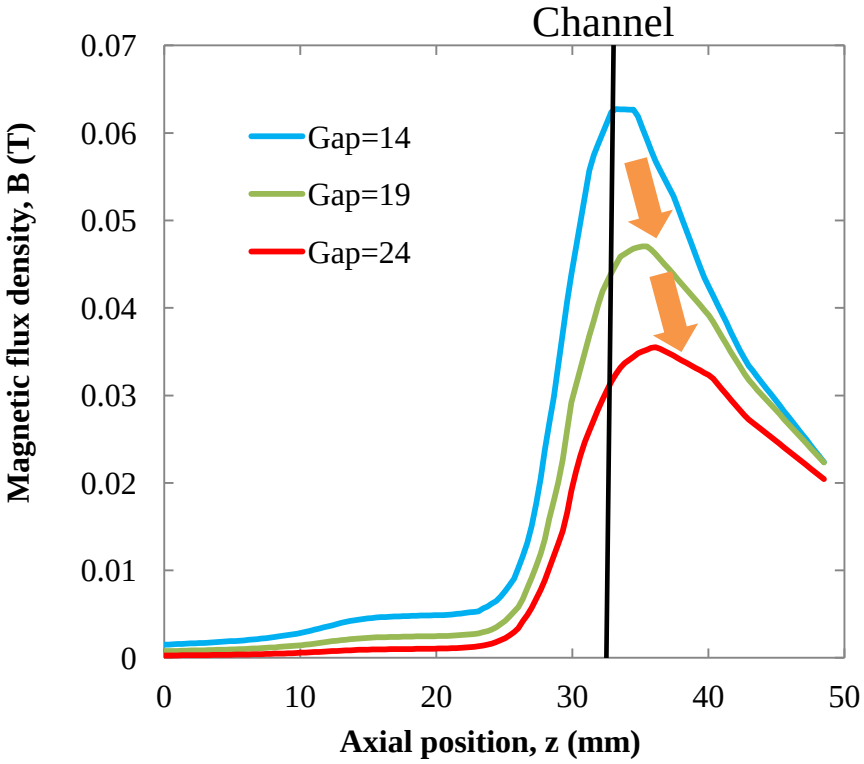

Figure 3.5 Axial distribution along with the center line between hollow anode of magnetic flux density with each type, when the coil current is 3 A.

3.5 Heat Flux Transfer Simulation

In analyzing heat flux transfer of UT-58, the first step is to assume the entire input power and the ratio of heat flux inflow to each part in the thruster body. The heat flux assumption is shown in Table 3.3. The entire input power was assumed to be 2000 W, and it was also assumed that 80 % of it inflows to the anode tips, 15 % to guard rings, and 5 % to pole pieces. The next step is to assume the cooling by water. To protect the thruster from the heat input to the anode and generation of heat at coils, the inner iron pole and the outer casing is cooled by water. The assumptions of cooling are shown in Table 3.4. The diameter of cooling tube was designed to be 4 mm, and water flowing velocity was assumed from the pump delivery pressure of 0.4 MPa of the water tower in the laboratory. MA 995 was used as insulators to insulate the anode potential parts and cathode potential parts. Analysis result of heat flux transfer is shown in Figure 3.6. The maximum temperature is 622 K at the tips of hollow anode. The temperature around inner coil is 510 K, which is below the maximum heatproof temperature of coil wire of 670 K.

Table 3.3 Heat flux assumption.

Power （W）	2000
Anode efficiency	0.3
Heat to anode (W)	1120 (80%)
Heat to guard ring (W)	210 (15%)
Heat to pole piece (W)	70 (5%)
Heat flux of anode (kW/m^2)	1173
Heat flux of guard ring (kW/m^2)	147
Heat flux of pole piece (kW/m^2)	42

Table 3.4 Cooling calculation values.

Diameter of pipe (cm)	0.4
Flow velocity (m/s)	100
Kinetic coefficient of viscosity (cm2/s)	8.58×10^{-7}
Reynolds number	4.66×10^{5}
Prandtl number	13
Nusselt number	1.07×10^{3}
Thermal conductivity (W/m・K)	0.60
Heat transfer coefficient (W/m^2・K)	2.26×10^{3}

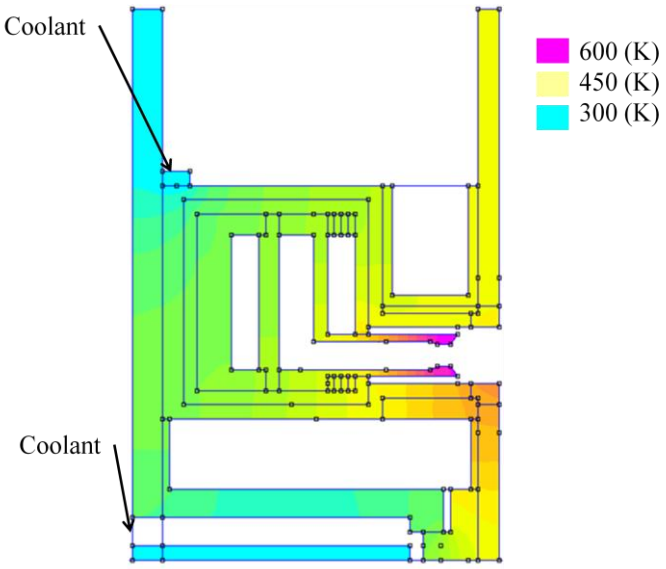

Figure 3.6 Temperature profiles of UT-58 calculated by heat flux assumption.

3.6 Other Noted Points

The outlook and cross-section drawing of UT-58 is shown in Figure 3.7 and Figure 3.8 respectively. The inner diameter and outer diameter of the channel are 50 mm and 66 mm respectively, and the channel length can be changed from 2 mm to 6 mm by removing the anode spacers. Guard rings are made of SUS304 and kept the same potential as the cathode. The entire diameter of the thruster is 160 mm, and the length is 53.5 mm.

Hollow anode made of copper whose thickness is 1 mm was installed because hollow anode was effective to decrease discharge current oscillation in the previous researches [27] [43]. Hollow anode has a bump structure in order neutral particles to be denser at the anode tip, which leads to be assumed propellant utilization efficiency becomes higher (Figure 3.9).

The propellant is induced to the plenum chamber through 4 ports at the back of the thruster and supplied to the anode section through 24 small holes whose diameter is 1 mm. After that neutral particles go through the inside of the hollow anode and supplied to the acceleration channel. This anode has 4 partitions at the intervals of 90^{o} to supply the propellant non-uniformly by the azimuthal position (Figure 3.10). Hollow anode is divided in the part where 10 mm upstream from the anode tip considering the PIC code numerical simulation by Yokota, S. et al. [44].

The discharge potential is applied to the anode though the anode pole made by copper, which is the same material as the anode in the back hole of the thruster insulating around it not to discharge between the pole and other body parts. The thruster assembly is keep simple and easy structure to perform maintenance.

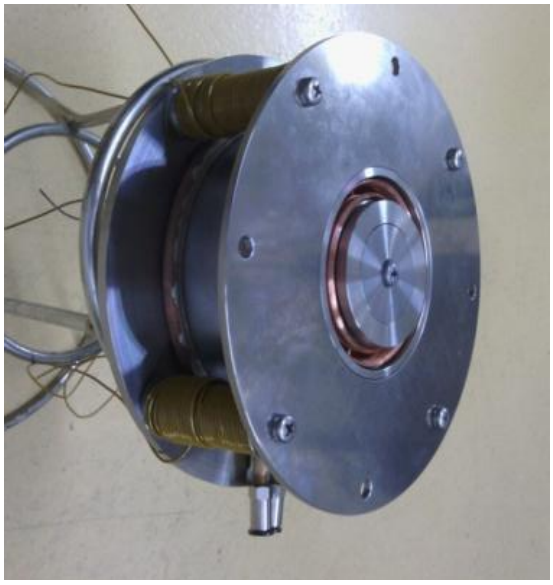

Figure 3.7 Outlook of OU-58 anode layer Hall thruster.

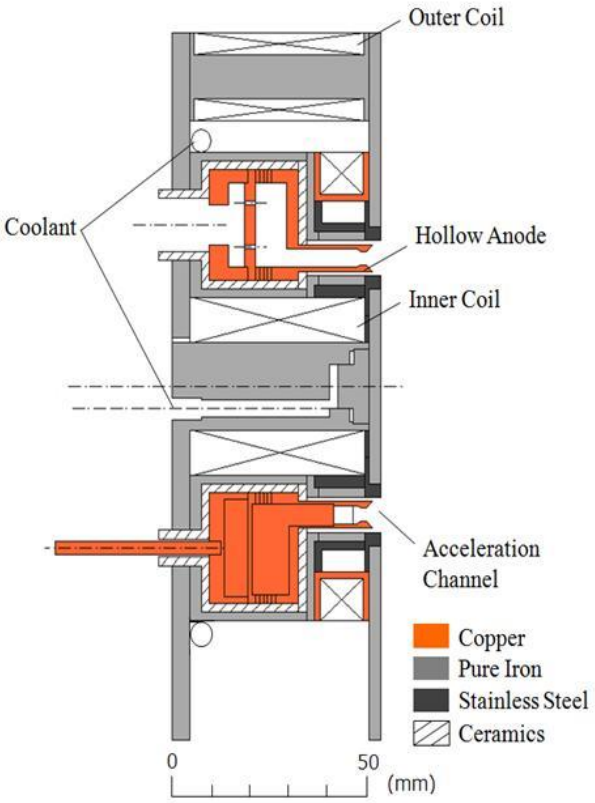

Figure 3.8 Cross-section drawing of UT-58 anode layer Hall thruster.

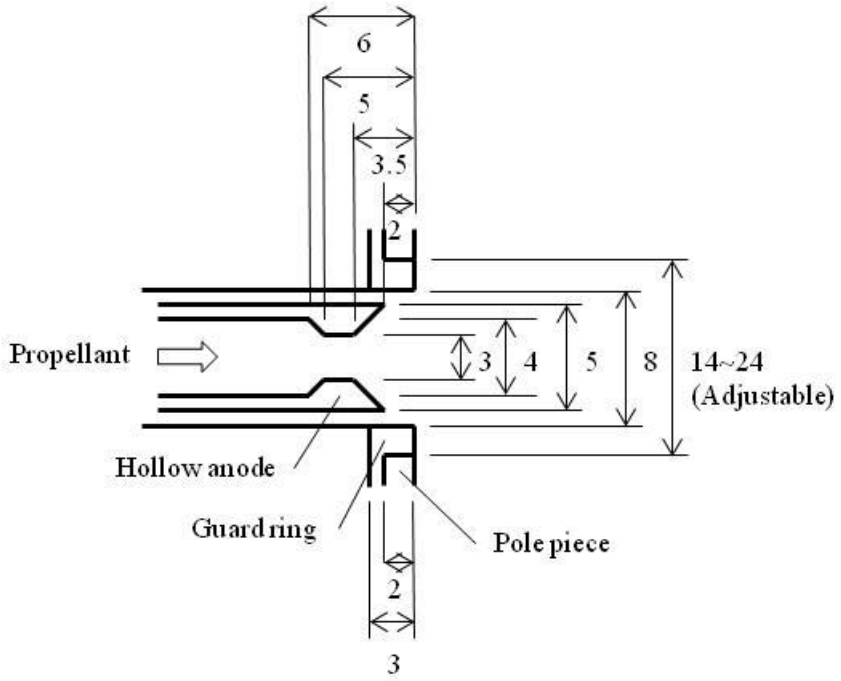

Figure 3.9 Cross section drawing of the acceleration channel of UT-58.

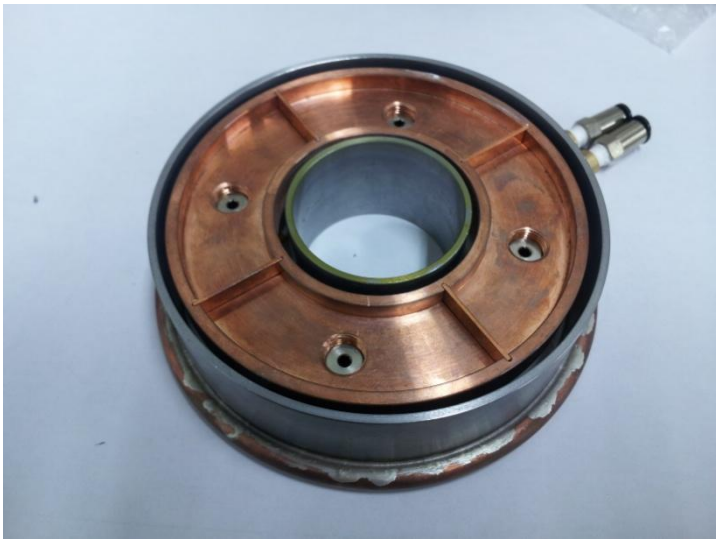

Figure 3.10 4 partitions of the plenum chamber.

Chapter 4

Experimental Setup

4.1 Hollow Cathode

A hollow cathode (HC-252, Vecco) was used as a neutralizer and electron source for the Hall thruster operation. Hollow cathodes are currently the most used neutralizer for EPs because it has low energy consumption, low mass flow consumption and long lifetime [45] [46] [2]. The appearance and operation principle of hollow cathode is shown in Figure 3.1 and 3.2 respectively. The electrons are emitted by low work function $(Ba/Sr)CO_3$ insert, and are extracted by scattering collisions with neutral gas, whereas the ions are confined by the double sheath structure at the cathode orifice. In this study, the cathode mass flow rate was kept to be 0.00 mg/s (5.78 sccm, 0.0 A_{eq}) of xenon gas, and the keeper was operated with constant current mode of 0.2 A.

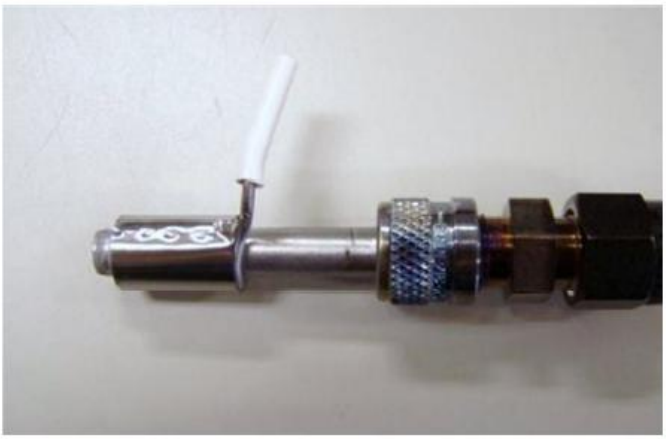

Figure 4.1 appearance of hollow cathode.

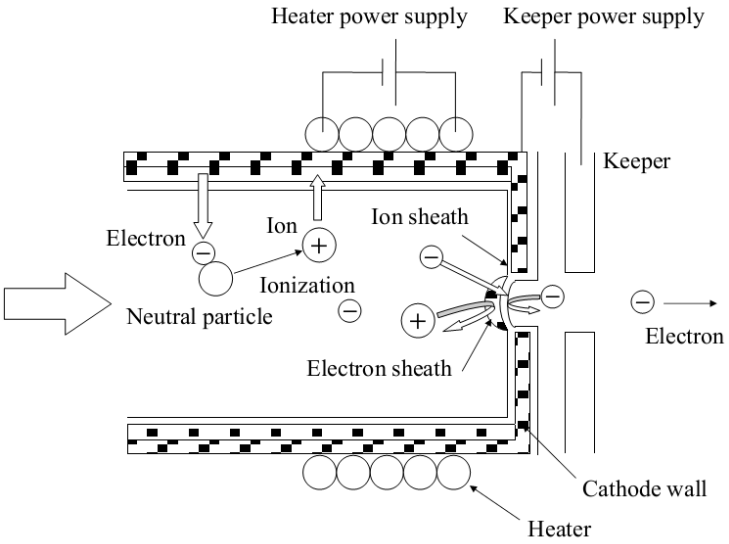

Figure 4.2 Operation principle of hollow cathode.

4.2 Vacuum System

The Hall thruster operation and all kinds of measurements were conducted in a 2.0 m × 3.0 m stainless vacuum chamber of the University of Tokyo, which is shown in Figure 3.3. The chamber was vacuumed by an oil diffusion pump (SPD-36, ULVAC) whose pumping speed was 37000 L/s. The main diffusion pump was supported by a mechanical booster pump (MB-10000, ULVAC, 10000 m^3/h) and two oil rotary pump (KS-150, ULVAC, 15000 L/min). The background pressure was measured at the opposite side of Hall thruster mount by an ionization vacuum gauge (WI-T15, ULVAC). Relative sensitivity of each gases and the background pressure was kept as shown in Table 3.1. and Table 3.2.

Table 4.1 Relative sensitivity of gases

Species	**He**	**Ne**	**Ar**	**Kr**	**Xe**	**N_2**	**O_2**	**H_2**	**Air**	**CO_2**
Relative sensitivity	0.221	0.358	1.34	1.88	2.5	1	0.879	0.491	0.97	1.35

Table 4.2 Background pressure during the experiment

Propellant (Mass flow rate)	**Xe (3.0 Aeq)**	**Ar (8.0 Aeq)**
Back pressure (Torr)	4.0×10^{-5}	7.3×10^{-5}

Figure 4.3 Outlook of 2.0 m×3.0 m vacuum chamber.

4.3 Thruster Cooling System

A circling cooling system was used to cool down the Hall thruster. A water pump and cooking tower is installed outside of the laboratory and supply 0.3 MPa cooling water as shown in Figure 3.00. The cooling water is induced into the chamber through the same flange as the propellant supplying system, and is exhausted out of the chamber again after cooling the thruster.

Figure 4.4 Water pump and cooling tower outside of the laboratory.

4.4 Propellant Supplying System

Xenon and argon gases which are used for thruster and the cathode regulated by the mass flow controller and supplied to the thruster and the cathode. The mass flow controllers for the thruster (KOFLOC, MODEL3200 and MODEL3610) and for the cathode (KOFLOC, MODEL 3600) were used as shown in Figure 3.00. To operate the mass flow controller, lead-put units (KOFLOC, MDEL CR300 and CR700) were used. The accuracy of the controller is 1 % at the maximum flow rate.

Figure 4.5 Mass flow controllers (Left: MODEL3660, Right: MODEL 3200, Downer: MODEL3610).

Figure 4.6 Lead-out units (Upper: CR300, Downer: CR700).

4.5 Measurement Systems

In this study, discharge current, guard ring current, beam current, and thrust were measured. These measurements are consist of electric circuits, digital oscilloscope, LabVIEW (National Instruments Corporation), and thrust balance systems. Each system is explained from next paragraph.

4.5.1 Electric Circuit

Figure 4.7 shows the concept of electric circuit of Hall thruster. The vacuum chamber is floated form the PPU devices of the thruster. Electric input or output of the thruster and ion collector is induced inside the chamber through the current inducing terminals in a flange. PPU devices used in this study were shown in Figure 4.8. These stabilized DC power supply has the transit response velocity of 100 μs for the low-voltage mode.

In order to measure entire ion beam current, 500×500 mm ion collector made of copper was used as shown in Figure 4.9. The fixed position is 250 mm downstream from thruster exit. In addition, the collector was kept -20 V to the ground to collect only ions and electrons escape from entering. If the secondary electrons are discharged by the ion collision, the ion beam current can be measured more highly, but the secondary electron discharge coefficient of copper is very small of 0.01 versus Xenon ions of 500 eV, thus this effect is negligible. Moreover, ion beam current is measured less when the ions are neutralized before they reach the ion collector. But xenon and argon mean free path of collision between ions and electrons is quite high compared to 250 mm, which is the distance between the thruster and collector, therefore, this effect is also negligible.

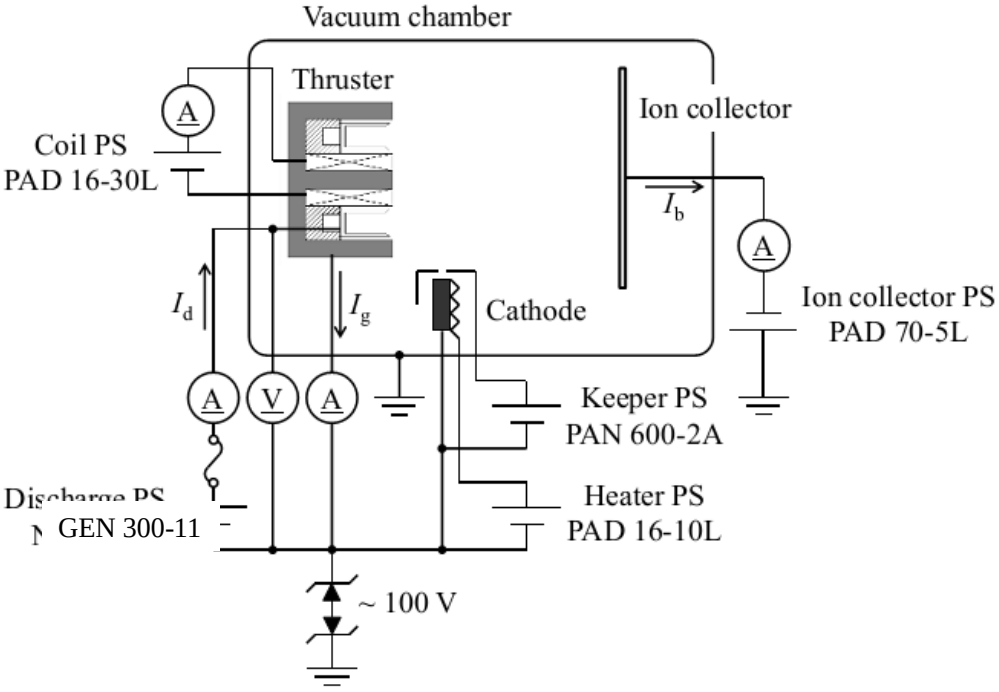

Figure 4.7 Electric circuit of Hall thruster measurement system.

Figure 4.8 PPU devices.

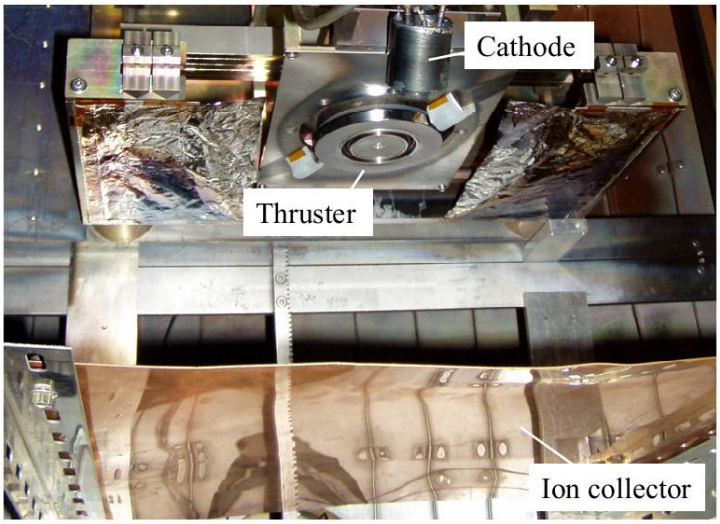

Figure 4.9 Outlook of ion collector.

4.5.2 Digital Oscilloscope

An oscilloscope (WE7000, Yokogawa Electric Corporation) was used for each current measurement. The maximum sampling rate was 20 MS/s, which is high enough to resolve the discharge oscillation of Hall thrusters [26]. The outlook is shown in Figure 4.10.

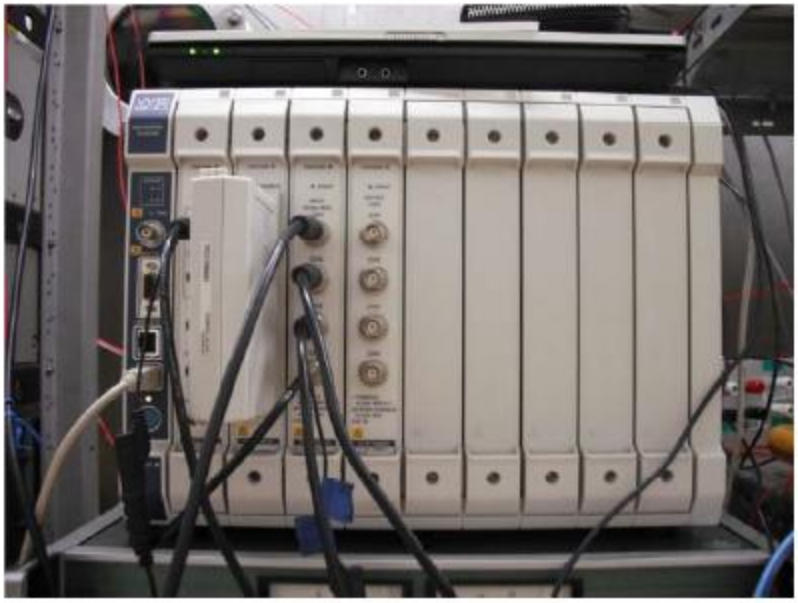

Figure 4.10 Digital oscilloscope.

4.5.3 Thrust Balance

Thrust generated by the Hall thruster was measured by a dual pendulum thrust balance developed in the University of Tokyo [47]. Figure 4.11 shows its schematic and appearance. The balance is controlled to cancel the generated thrust by $\boldsymbol{J}\times\boldsymbol{B}$ force, and the thrust was evaluated in terms of the current needed for the thrust cancelation. After the displacement signal goes into the low pass filter, it was read by LabVIEW. The thermal effect caused by the heating due to the thruster was minimized by the dual pendulum displacement measurement system.

To measure the thrust, thrust calibration is conducted between the controlling current and thrust using 4 precise weight of 2 g (±5 mg), and between the controlling current and coil current. The relations between controlling current and weight and between controlling current and coil current are shown in Figure 4.12.

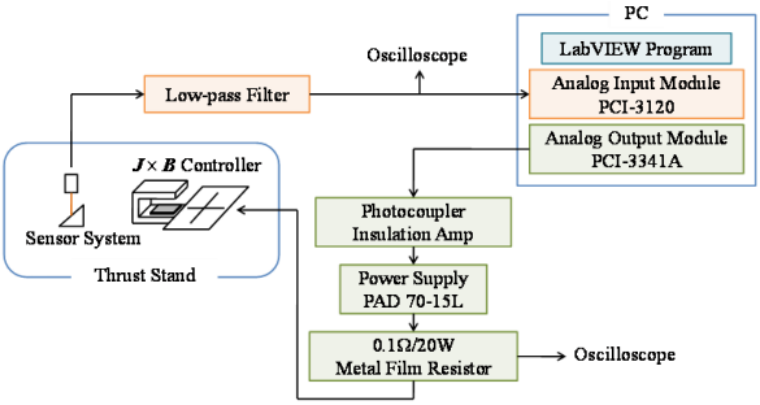

(a) Schematic of thrust measurement system.

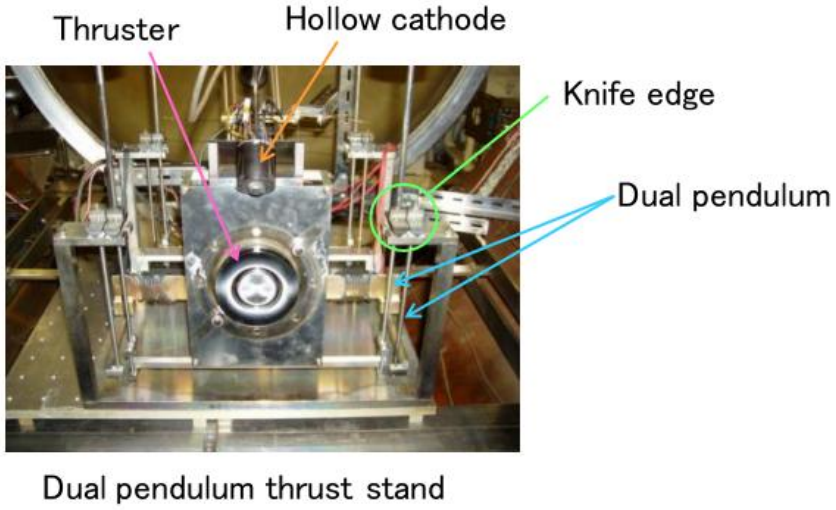

(b) Outlook of thrust balance.

Figure 4.11 Dual pendulum thrust balance.

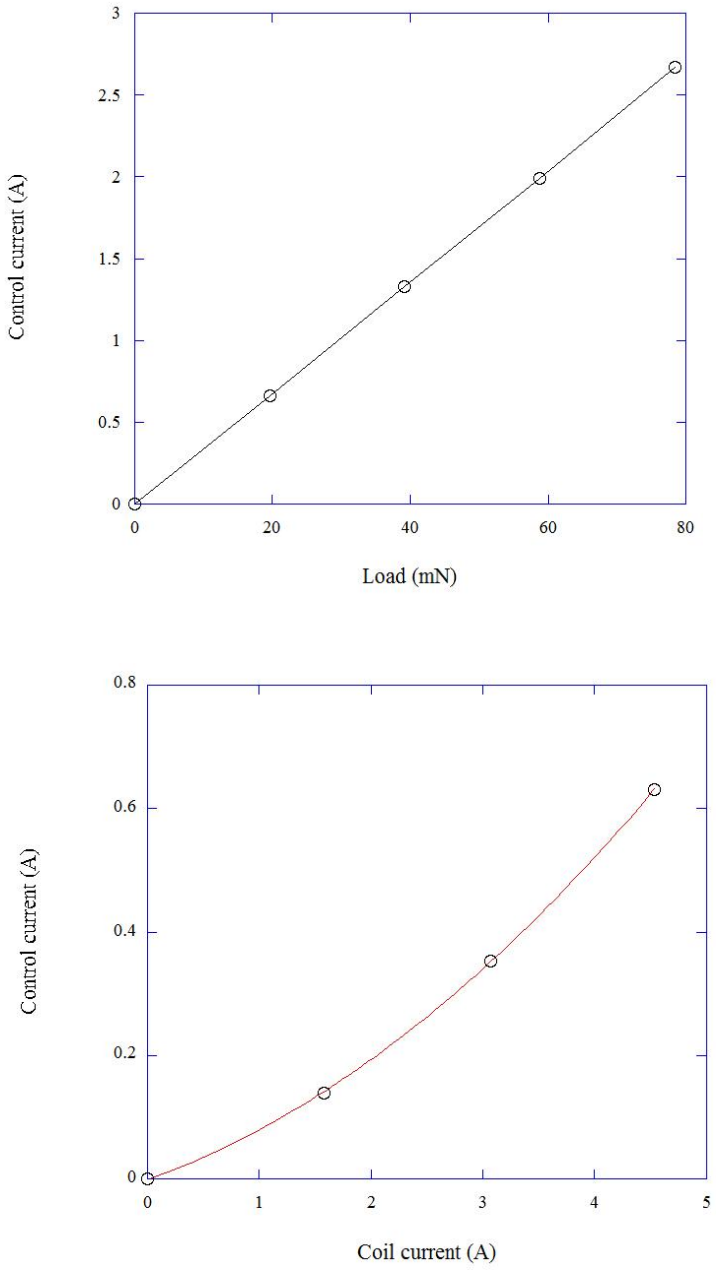

Figure 4.12 Relation of control current versus load and coil current.

Chapter 5

Results and Discussions

5.1 Discharge Characteristics of UT-58 with Xenon and Argon Propellant

5.1.1 Discharge Characteristics of UT-58 with Xenon Propellant

At first, UT-58 was operated with xenon propellant to evaluate its discharge characteristics and thrust performance. Propellant mass flow rate was between 1.0 and 3.0 Aeq. The evacuation capability of vacuum system prevented a higher mass flow rate. A picture of the thruster in operation is shown in Figure 5.1.

The discharge characteristics with xenon propellant are shown in Figure 5.2. Generally, two modes, high-voltage mode and low-voltage mode exist in operating Hall thrusters, and it changes through a point called “Knee Point” [48]. In our operating condition, the discharge current is larger than propellant mass flux equivalent to current, so these operating points are in high-voltage mode, and it is supposed that almost all propellant is ionized

The change of oscillation amplitude of discharge current with the change of discharge voltage is shown in Figure 5.3. It is clear that oscillation amplitude increases as discharge voltage increases. At many operating points except a few, Δ was beyond 0.2.

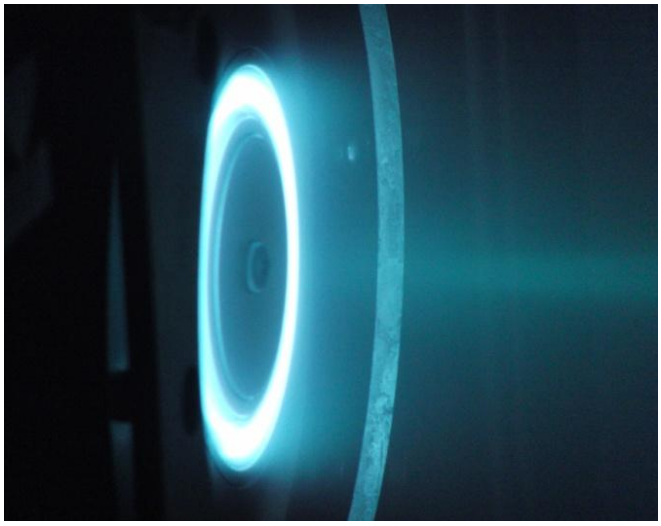

Figure 5.1 UT-58 operation with xenon propellant.

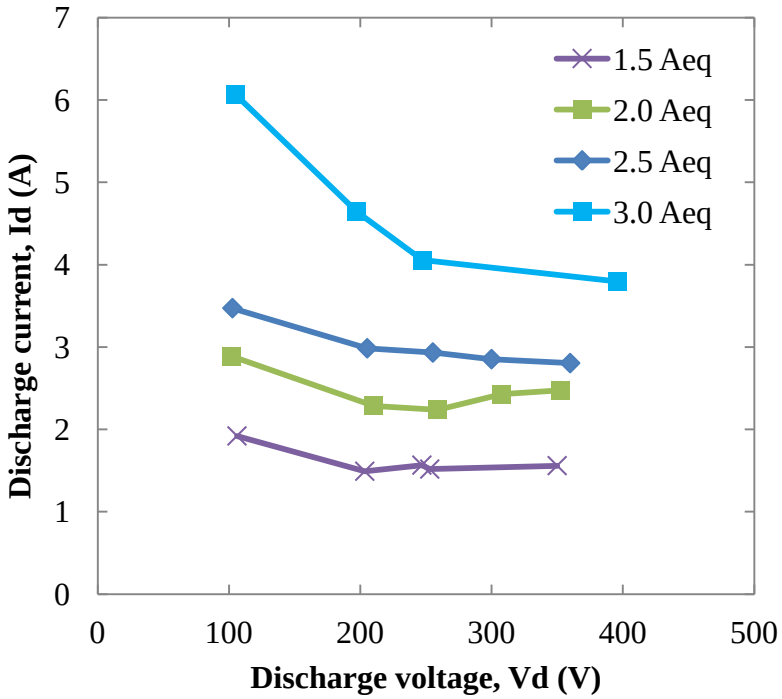

Figure 5.2 Discharge characteristics with xenon propellant.

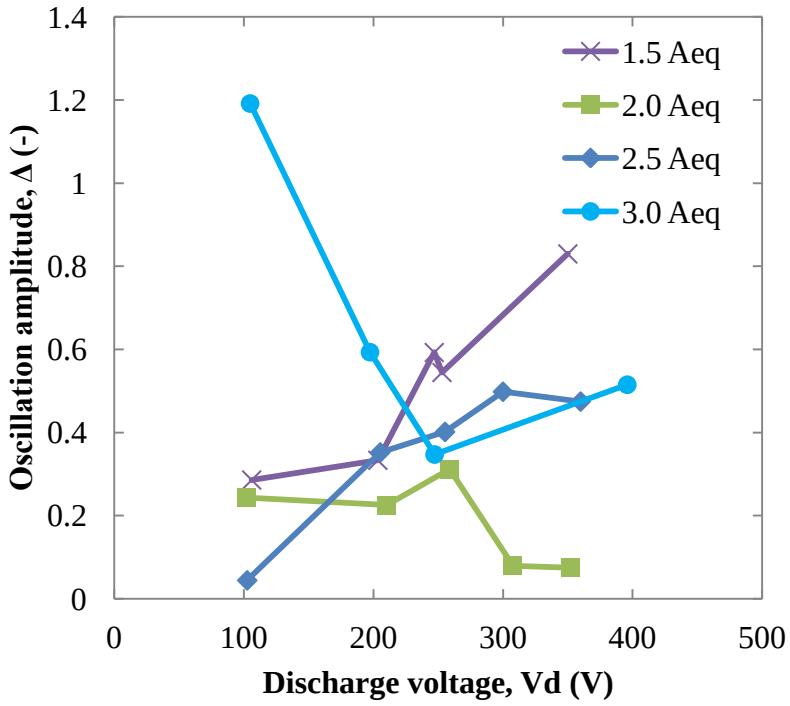

Figure 5.3 Oscillation characteristics with xenon propellant.

5.1.2 Discharge Characteristics of UT-58 with Argon Propellant

Next, UT-58 was operated with argon propellant. The picture of the thruster in operation with argon propellant is shown in Figure 5.4. As the ionization energy of argon is larger than that of xenon (Table 1.1, Figure 1.7 and Figure 1.8), and the ionization cross section of argon is less than half of that of xenon (Table 5.1), it is assumed that degree of ionization with argon propellant is typically smaller than with xenon [24]. In this research, the argon propellant mass flow rate is between 3.0 to 8.0 Aeq. Discharge was not stable at mass flow rates below 3.0 Aeq, and the mass flow controller limited to increase the mass flow rate beyond 8.0 Aeq.

Discharge characteristics and oscillation characteristics with argon propellant are shown in Figure 5.5 and Figure 5.6 respectively. Discharge current is lower than that of equivalent to propellant mass flow rate for lower mass flow rate up to 5.0 Aeq. Thus, these operating points are in low-voltage mod. However, the trend shows that the discharge current increases strongly with 6.0 Aeq, 7.0 Aeq and 8.0 Aeq but is more srable than with 3.0 Aeq. Oscillation amplitude with argon propellant was below 0.2 at many operating points. So it is concluded that discharge oscillation is not an issue with this input power level.

Figure 5.7 shows the internal current, beam current, guard ring current and discharge current with

argon propellant. As the discharge voltage increases, the beam current and guard ring current increases accordingly. This is because electron energy increases according to discharge voltage and more propellant is ionized. However, the electron current does not vary so much. This is because electron current does not follow the discharge voltage (input power) so much but follows the intense of magnetic flux density so much. These currents were measured with the regime with high magnetic flux density (50-80 mT), so the performance of the electron confinement by the magnetic field does not vary so much.

Figure 5.4 UT-58 operation with argon propellant.

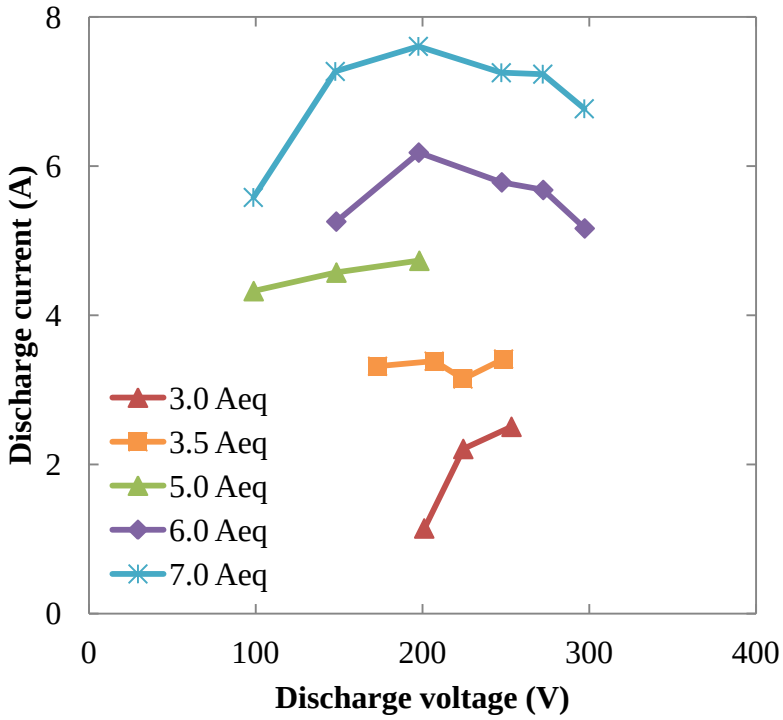

Figure 5.5 Discharge characteristics with argon propellant.

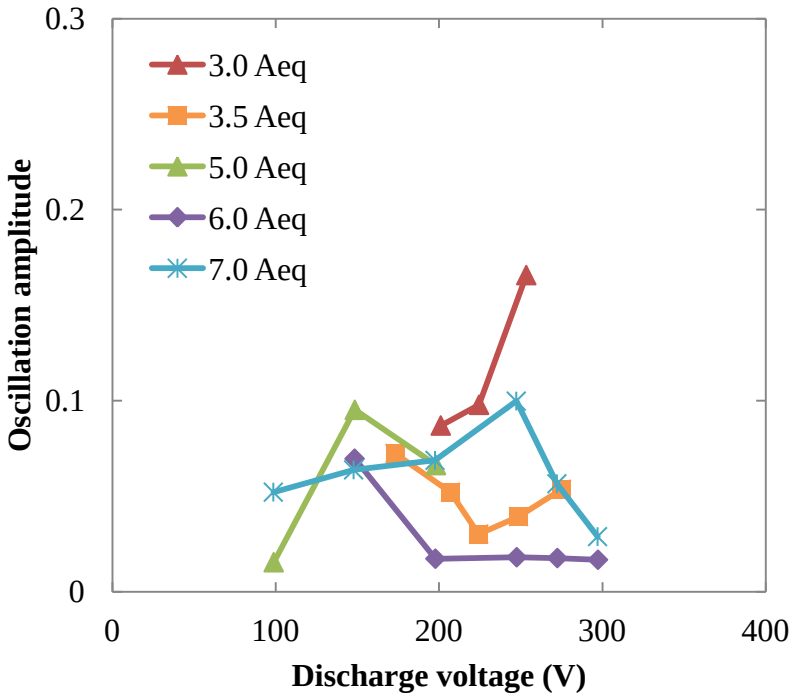

Figure 5.6 Oscillation characteristics with argon propellant.

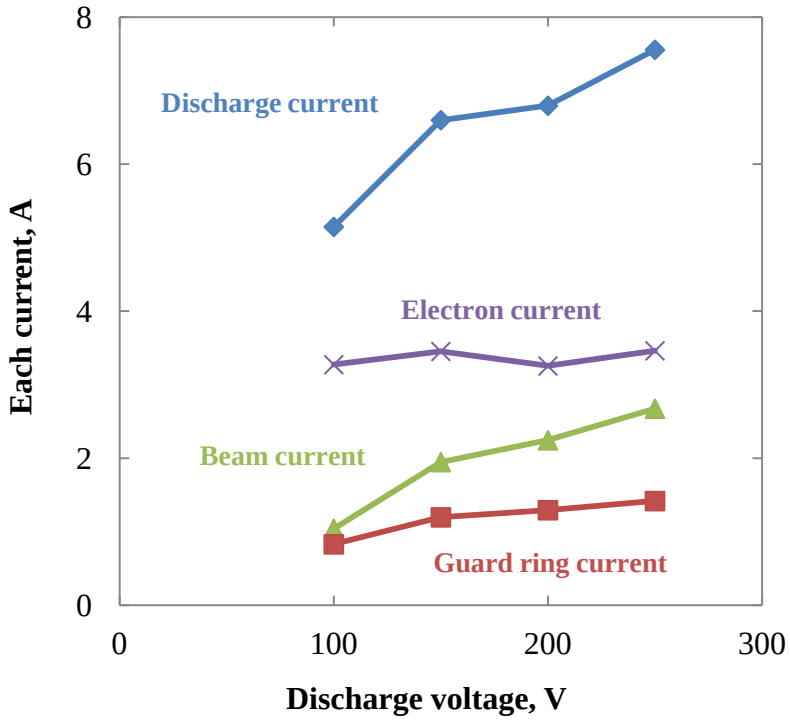

Figure 5.7 Internal current characteristics with argon propellant (*Q*=6.0 Aeq).

5.2 Thrust Performance of UT-58 with Xenon and Argon Propellant

5.2.1 Thrust Performance of UT-58 with Xenon Propellant

The thrust versus input power is shown Figure 5.4. Regardless of the variation of propellant mass flow rate, the thrust to power ratio stays constant, at about 54.7 mN/kW. At the operation point where the propellant flow rate is 3.0 Aeq and discharge voltage is 350 V, the thrust is as high as 92.2 mN.

The results of specific impulse and anode efficiency are shown in Figure 5.5. Similarly, the slope of the connection lines in Figure 5.5 is almost constant regardless of the difference of propellant flow rate. 73 % of anode efficiency as most and 1846 s of specific impulse are achieved at the operation point where the propellant flow rate is 3.0 Aeq and discharge voltage is 200 V. However, at this point the oscillation amplitude of discharge current is at a very high value of 0.59 as shown in Figure 5.3, where the thruster cannot be put in practical use.

Figure 5.6 shows the comparison between UT-58 and Russian TALs, D series. The anode efficiency is equal to or greater than that of other TAL thrusters with the same input power. It is

supposed that this is because the magnetic lines by magnetic shielding contribute to improved anode efficiency. That is, apart from stability of the thruster, the number of ions going into the guard ring becomes smaller.

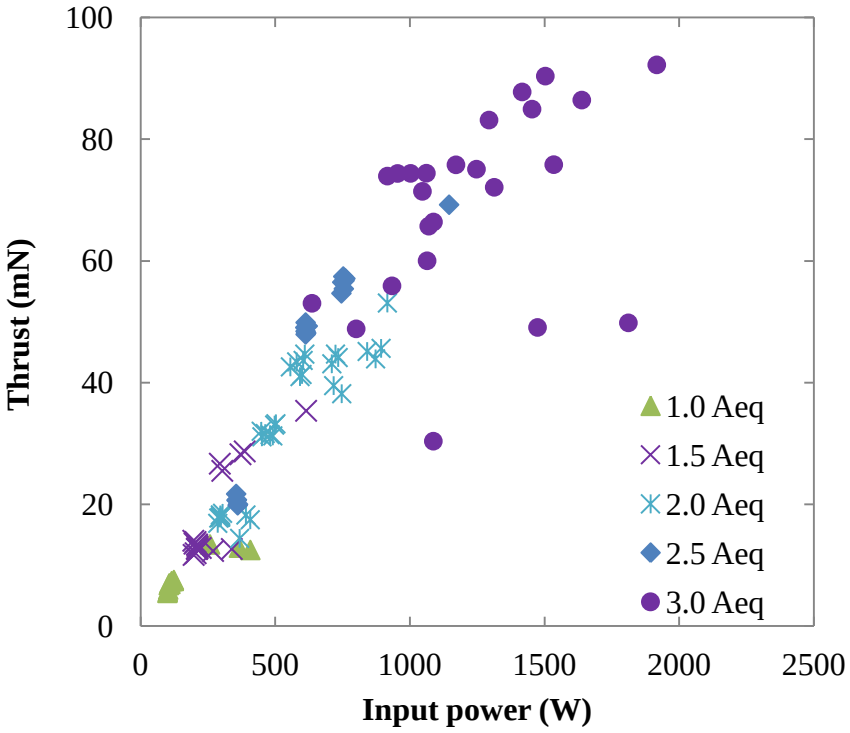

Figure 5.8 Thrust versus input power with xenon propellant.

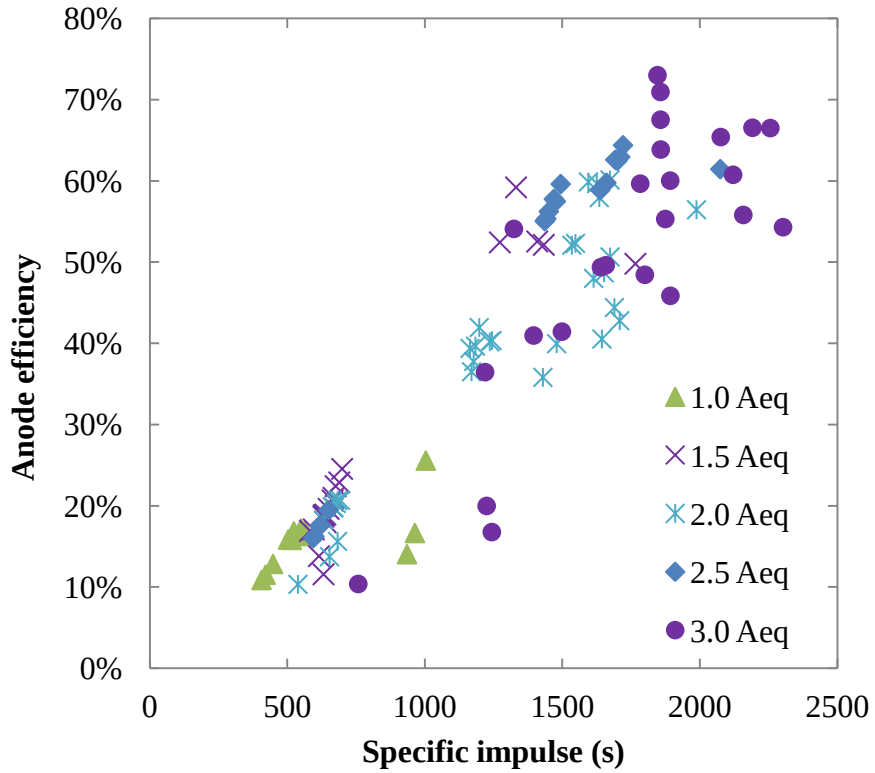

Figure 5.9 Thrust performance with xenon propellant.

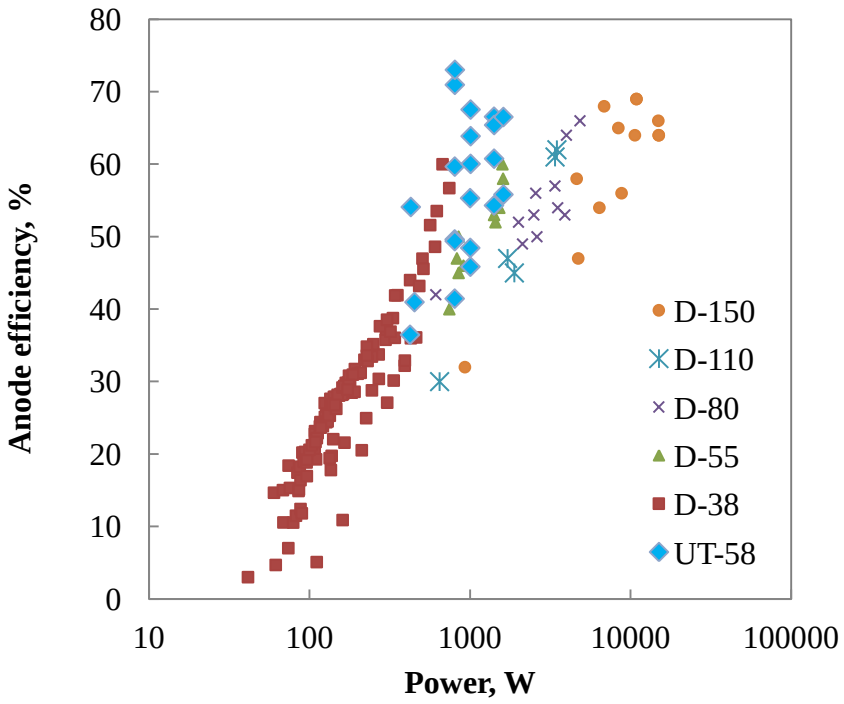

Figure 5.10 Comparison of the anode efficiency versus input power with Russia D series.

5.2.2 Thrust Performance of UT-58 with Argon Propellant

Thrust versus input power and thrust performance are shown in Figure 5.10 and Figure 5.11 respectively. A maximum thrust of 51.8 mN and a maximum anode efficiency of 23.5 % were achieved. The thrust to power ratio was improved when more mass flow rate was supplied. Besides, the anode efficiency with more propellant flow rate was higher than that with lower propellant flow rate. The aim to achieve, an anode efficiency of 15 % could be achieved, as was seen necessary by calculation [23].

Table 5.1 shows the summary of thrust performance of UT-58 with xenon and argon propellant.

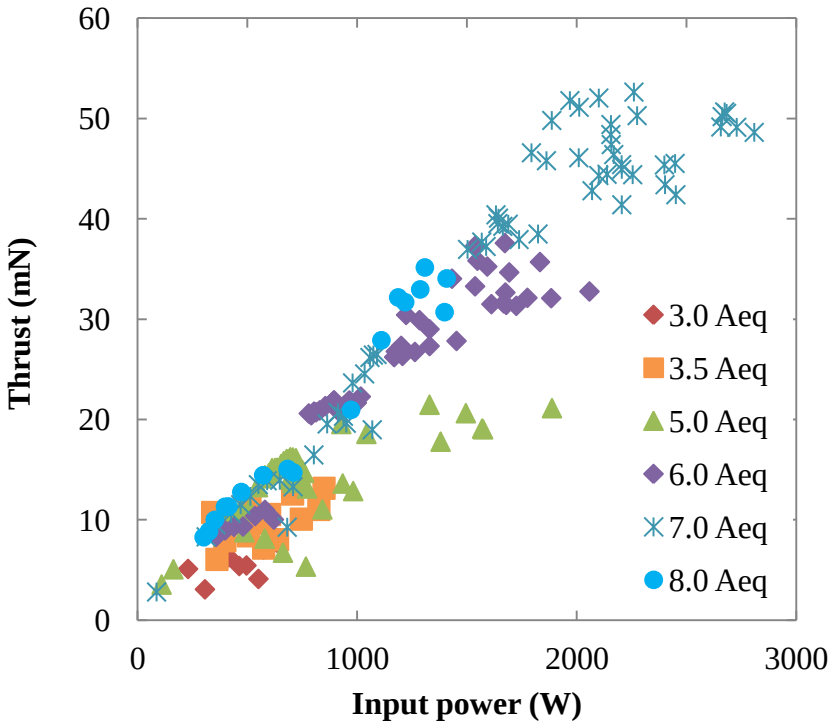

Figure 5.11 Thrust versus input power with argon propellant.

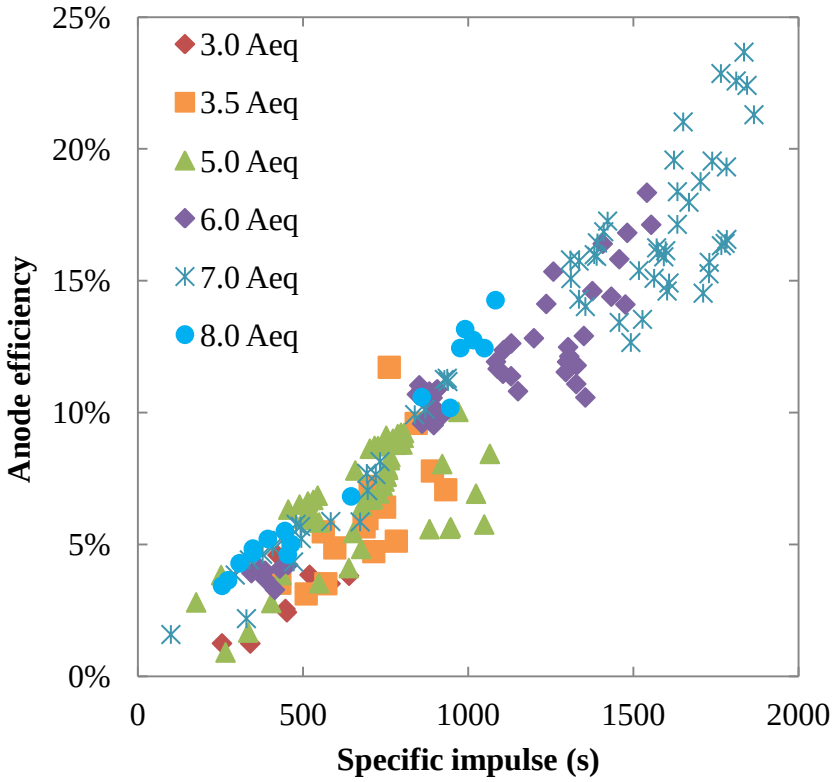

Figure 5.12 Thrust performance with argon propellant.

Table 5.1 Summary of thrust performance of UT-58.

	Xenon (~3.0 Aeq)	**Argon (~8.0 Aeq)**
Input power (kW)	1.92	2.81
Maximum thrust (mN)	92.2	51.8
Maximum anode efficiency (%)	73.0	23.5
Maximum specific impulse (s)	2302	1864

5.3 Comparison of Operating Characteristics of UT-58 between Xenon and Argon Propellant

5.3.1 Characteristics of Discharge Current and Oscillation Amplitude versus Magnetic Flux Density with Xenon and Argon Propellant

As is mentioned in Chapter 2.4, a few modes of electron diffusion exist in Hall thrusters, and discharge current and oscillation amplitude of Hall thrusters depend on the magnetic flux density. Figure 5.13 shows the measured discharge current and oscillation amplitude with xenon propellant where the propellant mass flow rate was 2.0 Aeq and the discharge voltage was 200 V. And Figure 5.14 also shows the both with argon propellant where the propellant mass flow rate was 6.0 Aeq and the discharge voltage was 250 V. Following the theory in Chapter 2.4, the characteristics of discharge current and oscillation amplitude classified into 3 electron diffusion regions, classical diffusion region, transition region, anomalous diffusion region as shown in Figure 5.13 and Figure 5.14. With both xenon and argon propellant, the classical region is located where the magnetic flux density is up to around 16 mT. However, the biggest difference of the characteristics between xenon and argon is the width of the transition region. As for xenon propellant, it is considered that the transition region is located in the regime where from 16 mT to 51 mT of the magnetic flux density. On the other hand, as for argon propellant it is considered that the transition region is located in the quite narrow regime where from 16 mT to 22 mT of the magnetic flux density.

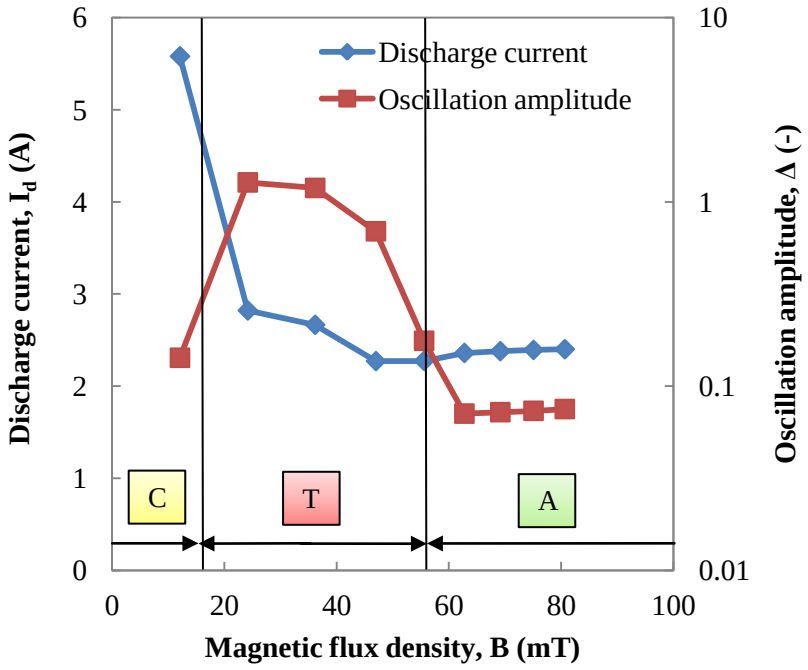

Figure 5.13 Typical characteristics of discharge current and oscillation with xenon propellant (V_d=200 V, Q=2.0 Aeq).

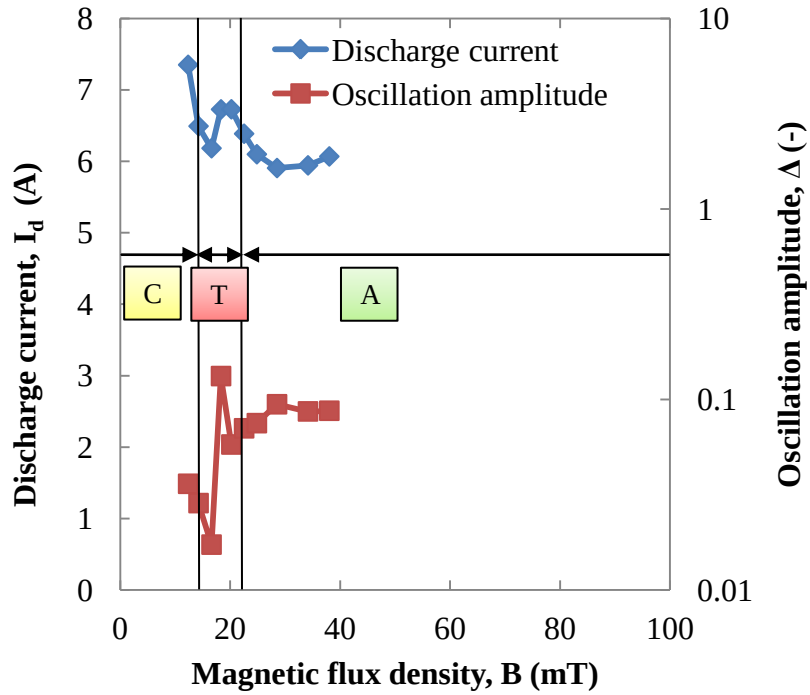

Figure 5.14 Typical characteristics of discharge current and oscillation with argon propellant (V_d=250 V, Q=6.0 Aeq).

5.3.2 The Definition of Common Three Electron Diffusion Modes by Each Oscillation Amplitude with Xenon and Argon Propellant

It is said in Chapter 2.4 that electron velocity in the axial direction at the channel exit relates so much to the oscillation characteristics in Hall thrusters, and that is expressed as a function of V_d, Q, σ, M, and $\boldsymbol{B}$ as:

$$-v_{ez,exit} \propto \frac{Q \cdot \sqrt{m_n} \cdot \sigma \cdot V_d}{B^2} \tag{5.4}$$

Figure 5.15 shows the plots of the oscillation amplitude with xenon and argon versus the expression for the electron velocity in the axial direction at the channel exit (Eq. 5.4). It is noted that regardless the kind of propellant, the characteristics of the oscillation amplitude has the same trend. The oscillation amplitude has lower level in the regime where the abscissa is lower, but that has quite higher level in the regime where the abscissa is increased, and that has lower level again in the regime where the abscissa is more increased. Now, the FWHM (Full Width at Half Maximum) is introduced for both xenon and argon propellant, and points indicating the maximum oscillation amplitude and those indicating the half value of each maximum. Regardless of kinds of propellant, the same lines passing through the points indicating the half values of their maximum are described. Thus, the common three electron diffusion regions are defined by these common two lines. The low magnetic flux density regime can be classified under anomalous diffusion region, the high magnetic flux density regime can be classified under classical diffusion region, and the intermediate region between anomalous and classical diffusion region can be classified under transition region.

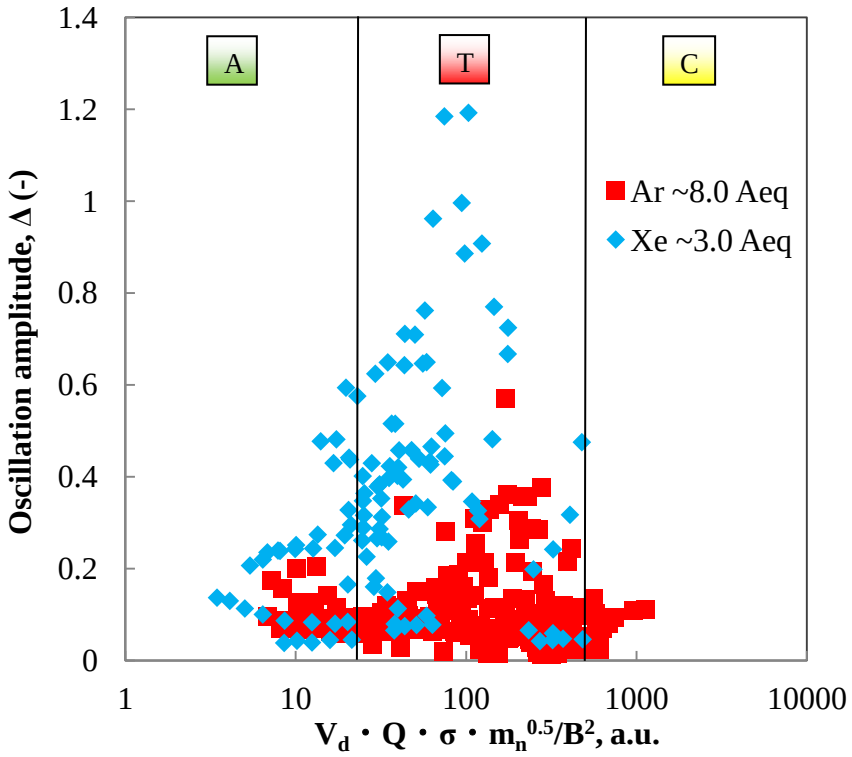

Figure 5.15 Three same electron diffusion modes regardless of xenon and argon propellant.

5.3.3 Oscillation Map and Anode Efficiency Map with Xenon and Argon propellant

The most important input parameters for Hall thrusters operation are discharge voltage $\boldsymbol{V_d}$, propellant flow rate $\boldsymbol{Q}$, and magnetic flux density $\boldsymbol{B}$. Translating the expression of the electron velocity in the axial direction to the these three parameters above, the optimal operating points can be understood well. Figure 5.16 and Figure 5.18 shows the oscillation maps with xenon and argon propellant respectively. The abscissa of these figures is magnetic flux density, that is, the function of the denominator of Eq. 5.4, and the ordinate of these figures is the function of discharge voltage, propellant flow rate, and coefficient of each propellant, that is, the numerator of Eq. 5.4. And the borderlines of electron diffusion modes in Figure 5.15 are described as curves in the form of $y = Cx^2$, where y is the numerator of Eq. 5.4, x is the magnetic flux density, and C is the coefficient of the borderlines in Figure 5.15, those are 20 and 300. By doing such manipulations, the three electron diffusion regions can be understood along the three important input parameters of Hall thrusters and optimal operating points can be found easily. From the left side, classical diffusion region, transition region and anomalous diffusion region are classified by the two curving

borderlines. As the same as Figure 5.15, the oscillation amplitude with each propellant is lower in the classical and anomalous diffusion regions, but that is higher in the transition region. The color scale of Figure 5.16 and Figure 5.17 shows the oscillation amplitude. The ordinate is a function of discharge voltage and propellant flow rate, thus this is the image of the input power. The region where is no color shows where UT-58 could not be operated. The limitation of the ordinate is by the limitation of the PPUs and the evacuation of the vacuum system.

To understand better the optimal operating points with argon propellant comparing to xenon propellant, anode efficiency maps with xenon and argon propellant are introduced. Figure 5.18 and Figure 5.19 shows the anode efficiency maps with xenon and argon propellant respectively. In this research, optimal operating points are defined as those having higher anode efficiency and lower oscillation amplitude. By these figure, it is concluded how to achieve higher anode efficiency stably with xenon and argon propellant in UT-58. UT-58 could not be operated in the classical diffusion region with xenon propellant, but succeeded in all regions with argon propellant. The optimal operating point is in anomalous diffusion region with xenon propellant. However, that is in classical diffusion region with argon propellant, where the magnetic flux density is around 20 mT. Again, it is discovered from Figure 5.11 and Figure 5.12 that in order to realize higher anode efficiency with argon propellant, more mass flow rate and more discharge voltage should be applied, which means more operating regime should be realized in the regime in the higher value of the ordinate in Figure 5.19. Thus, it is concluded that operating regime with argon propellant should be expanded according to red arrow.

As the thruster size increases, the width between the pole pieces increases accordingly. That means, the application of higher magnetic flux density is more difficult as shown from Figure 3.2 to 3.5. As for UT-58, ideal shape of magnetic lines using magnetic shielding can achieve only limited value of magnetic flux density as is indicated in Figure 3.5. However, by using argon propellant, UT-58 can be operated in the classical diffusion region efficiently and stably, when the magnetic flux density is quite small. Thus, an ideal shape of magnetic lines can be applied, reducing the erosion of channel wall.

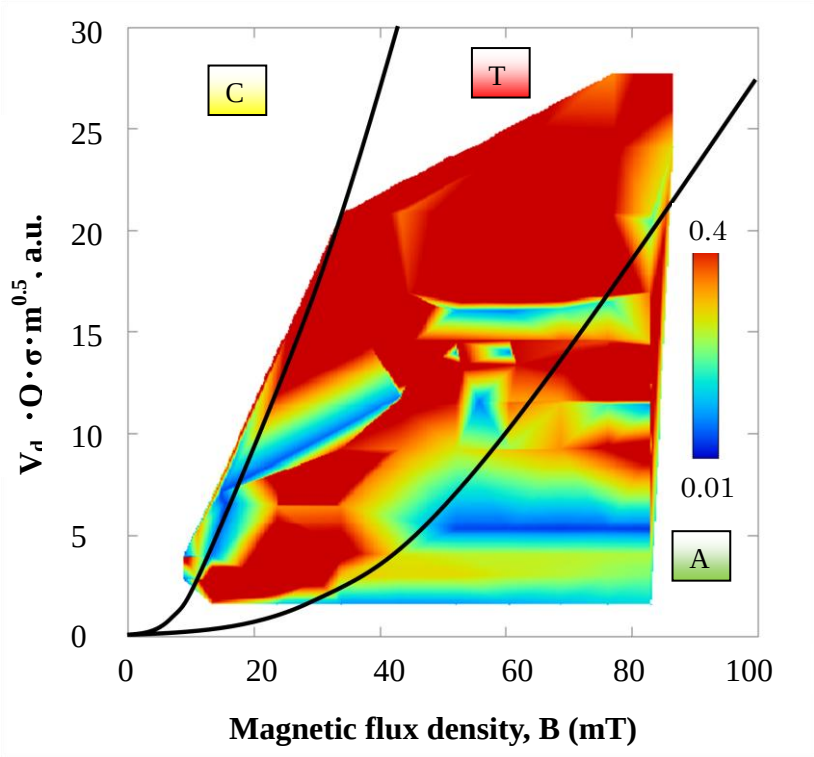

Figure 5.16 Oscillation map with xenon propellant.

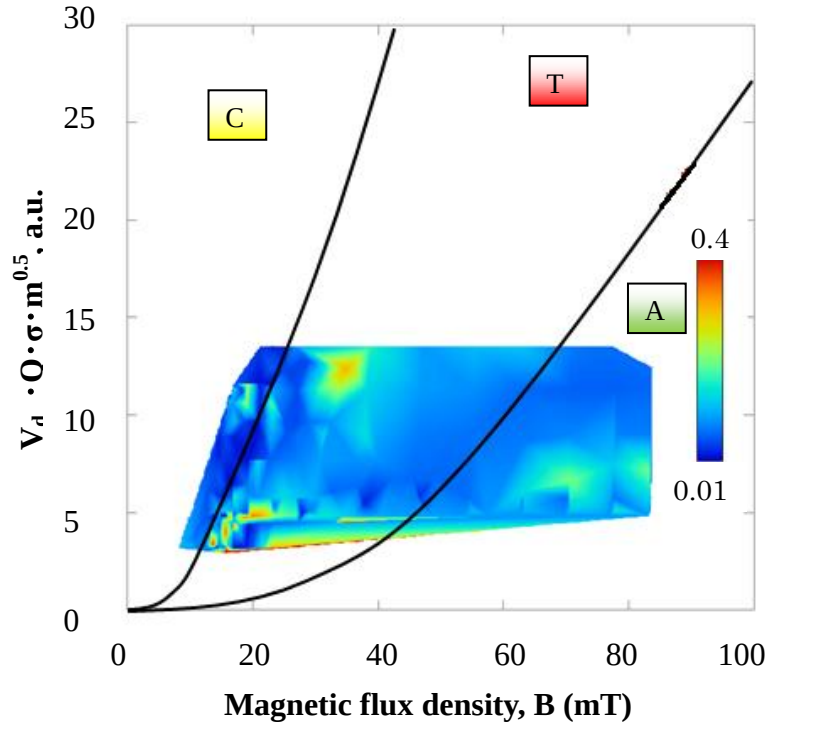

Figure 5.17 Oscillation map with argon propellant.

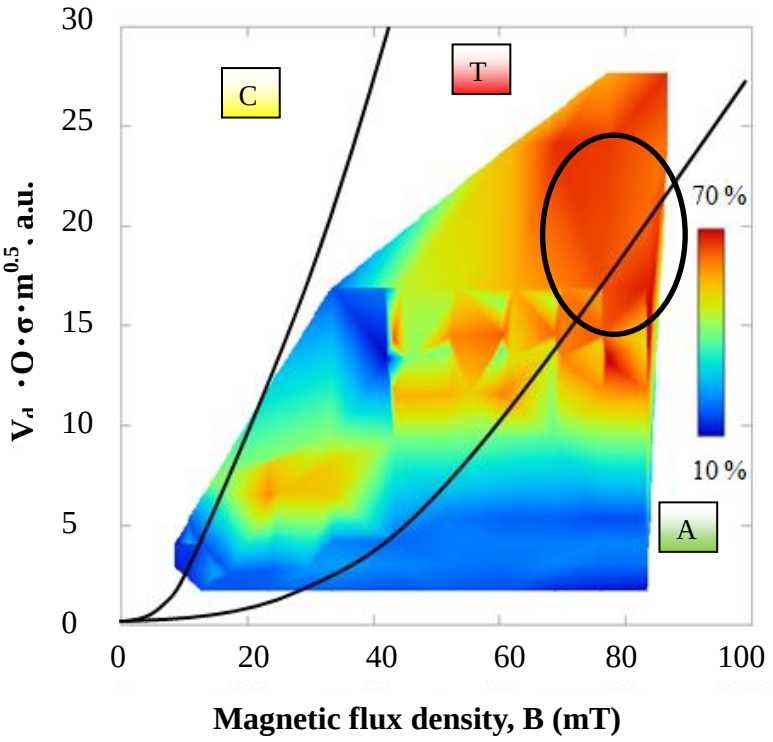

Figure 5.18 Anode efficiency map with xenon propellant.

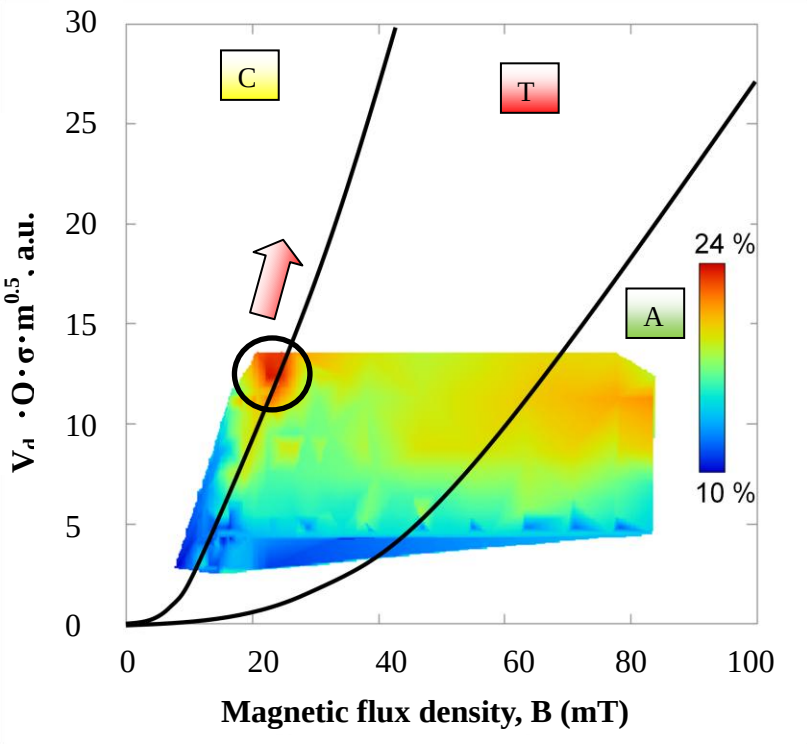

Figure 5.19 Anode efficiency map with argon propellant.

5.3.4 Discussions of the Difference of Optimal Operation Regime between Xenon and Argon Propellant

As shown in 5.3.3, the optimal operation region is different between xenon and argon propellant. The reason is discussed in this paragraph.

<Xenon propellant>

As for xenon propellant, the optimal operation regime is in the transition region and anomalous diffusion region, where the magnetic flux density is relatively high. As shown in Figure 5.2, the discharge current is larger than that is equivalent to current. Therefore, xenon propellant operation is considered to be in the high-voltage mode, and almost all of propellant is ionized. Figure 5.20 shows the discharge current and thrust versus magnetic flux density when the discharge voltage is 250 V and propellant mass flow rate is 3.0 Aeq, where more than 70 % of anode efficiency was achieved. As same as the typical tendency of discharge current by the electron diffusion, it increases in the transition region but decreases again forward anomalous region soon. This can be explained as follows: in the region where the magnetic flux density is high, the electron mobility decreases according to $1/B^2$, therefore the electrons get to be less likely to flow into the anode side. Consequently, the electron current decreases in the anomalous diffusion region, which results in the decrease of the entire discharge current. On the other hand, the thrust does not vary so much versus the change of the magnetic flux density, which means the beam current does not vary so much versus the change of the magnetic flux density. As a result, the acceleration efficiency is improved, thus the entire anode efficiency is also improved.

Figure 5.21 shows the anode efficiency map and discharge voltage line with xenon propellant. Compared the operation point which achieved more than 70 % of anode efficiency where the discharge voltage was 250 V, in order to achieve higher anode efficiency UT-58 should be operated in the anomalous diffusion where the electron current decreases with higher input power. According to Figure 5.21, with 350 V or 400 V of discharge voltage, UT-58 was operated only in the transition region where the decrease of electron current is insufficient. Consequently, UT-58 with 350 V or 400 V of high discharge voltage is considered to be able to achieve higher anode efficiency in the anomalous diffusion region. In other words, UT-58 should be applied more magnetic flux density which positions in the righter side from of the right border curve in Figure 5.21.

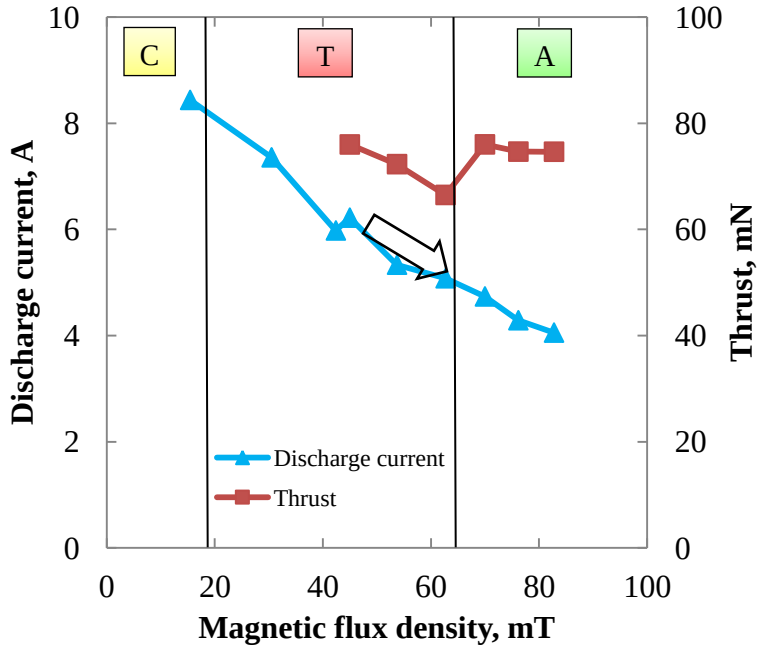

Figure 5.20 Discharge current and thrust versus magnetic flux density (V_d=250 V, Q=3.0 Aeq, xenon).

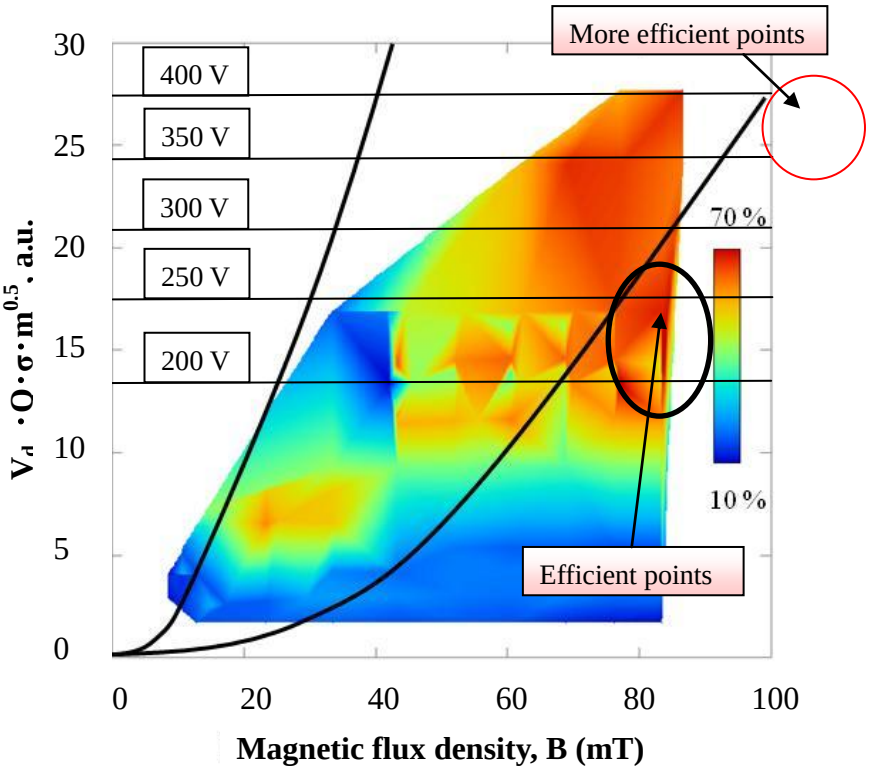

Figure 5.21 Anode efficiency map and discharge voltage lines with xenon propellant (Q=3.0 Aeq).

<Argon propellant>

As for argon propellant, the optimal operation regime is in the classical diffusion region, where the magnetic flux density is low. As shown in Figure 5.5, the discharge current is lower than that is equivalent to current, and it increases relatively sharply as the discharge voltage increases. Therefore, argon propellant operation is considered to be in the low-voltage mode, and not so much of propellant is ionized. As for the reasons why UT-58 with argon propellant achieved the highest anode efficiency in the classical diffusion region where the magnetic flux density is low are considered to be following two reasons:

1. Influence of relative higher input power

In the region where the magnetic flux density, the electron cannot be confined very well by the magnetic field, which leads higher electron current. As a result, the entire discharge current increases and total input power also increases when the applied voltage is the same level. This increased input power leads higher electron temperature assuming that the density of plasma is constant. Consequently, more neutral particles are collided with electrons and ionized, thus the propellant utilization efficiency increases. Figure 5.22 shows the acceleration efficiency and propellant utilization efficiency versus magnetic flux density when the discharge voltage was 100 V and propellant mass flow rate was 6.0 Aeq of argon. Propellant utilization efficiency is highest in the Figure in the regime where the magnetic flux density is from 20 mT to 30 mT.

2. More efficient confinement of electrons in the classical diffusion region

As for argon propellant, propellant utilization efficiency is quite lower than that with xenon propellant. In such condition, UT-58 could be operated in the classical diffusion region. On the other hand, UT-58 with xenon propellant whose propellant utilization efficiency is quite high almost could not be operated in classical diffusion region as shown in Figure 5.16 and Figure 5.18. Electrons are considered to be confined more efficiently in the classical diffusion region where electron mobility follows $1/\boldsymbol{B}^2$ than in the anomalous diffusion region where electron mobility follows $1/\boldsymbol{B}$. The electrons' efficient confinement results in the relatively more frequent ionization collision and higher propellant utilization efficiency. Moreover, such regime is considered to be the blue green region in Figure 2.8 where the oscillation amplitude is quite low. The low propellant utilization efficiency seems to be the cause of low oscillation amplitude of discharge current with argon propellant. Consequently, if the propellant utilization efficiency is improved, the more efficient operation points will be in the anomalous diffusion region than in the classical diffusion region, and the oscillation amplitude will become larger.

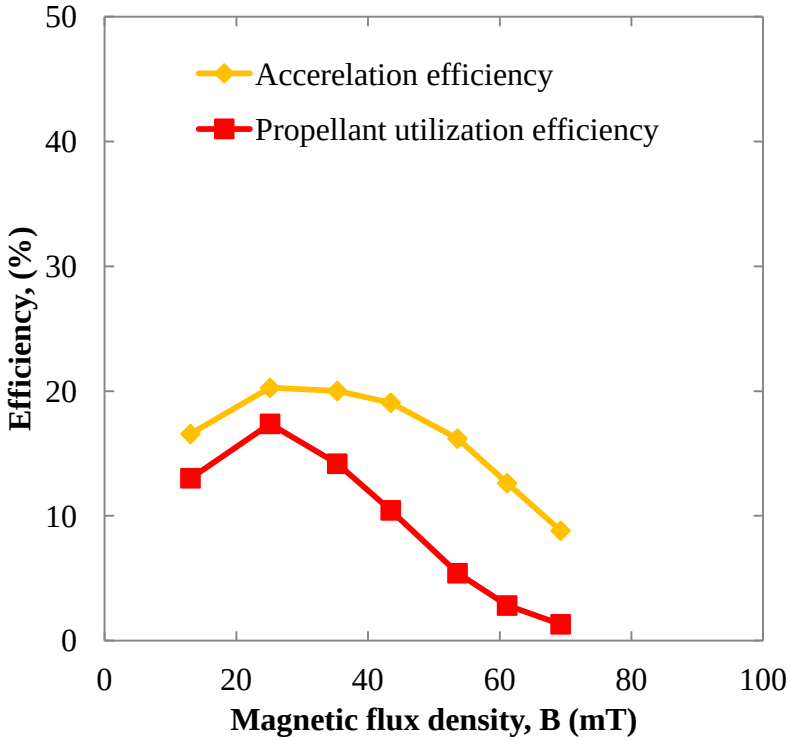

Figure 5.22 Acceleration efficiency and propellant utilization efficiency versus magnetic flux density (V_d=100 V, Q=6.0 Aeq).

5.4 Design Suggestion for Argon Anode Layer Thruster

5.4.1 Internal Efficiencies of UT-58 with Argon Propellant

Figure 5.23 shows the each internal efficiency, those are acceleration efficiency, propellant utilization efficiency and energy efficiency, with argon propellant when the propellant flow rate is 6.0 Aeq. The acceleration efficiency and propellant utilization efficiency are calculated using the measured beam current shown in Figure 5.10, and energy efficiency is calculated using measured thrust shown in Figure 5.11. As the discharge voltage increases, which is the same as the input power increases, the each efficiency is improved. Especially, the propellant utilization efficiency was most improved by 156 % when the discharge voltage was 250 V compared to 100V. The discharge characteristics of UT-58 with argon propellant indicates low-voltage mode as shown in Chapter 5.000000, thus these internal efficiency will be improved when the more discharge voltage is applied according to the red arrow in Figure 5.23.

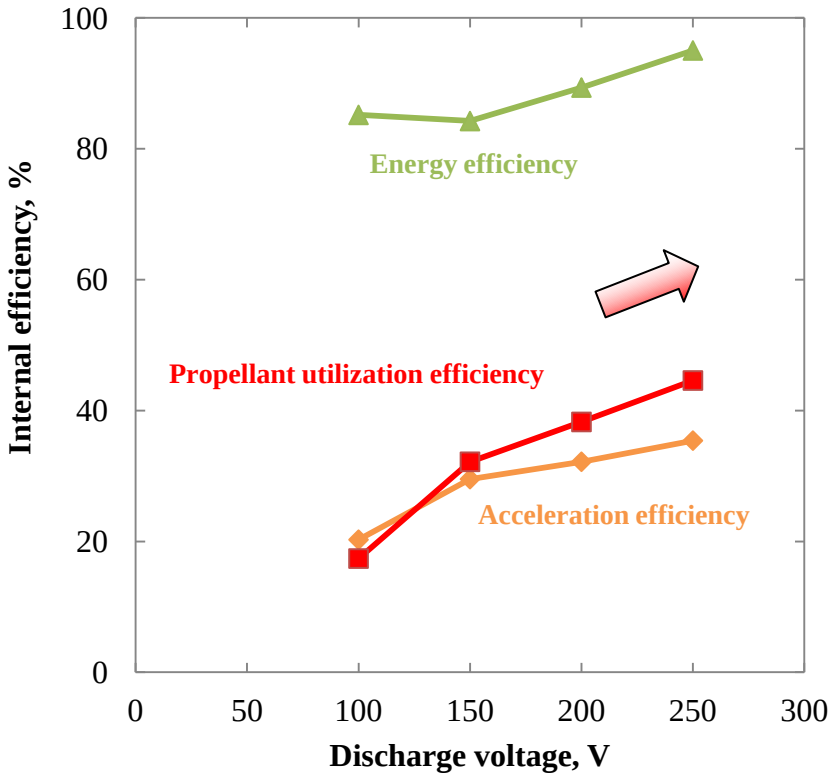

Figure 5.23 Internal efficiencies with argon propellant.

5.4.2 Methods for Improvement of Propellant Utilization Efficiency with Argon Propellant

As is shown in 5.3.1, the most serious cause of the low anode efficiency of UT-58 with argon propellant is low propellant utilization efficiency. That propellant utilization efficiency is modeled as [49]:

$$\eta_u = 1 - \exp\left(-\frac{\beta_i L \dot{m}}{v_n S \sqrt{2em\Delta\varphi_i}} \eta_u \right) \tag{5.1}$$

Instead of Eq. 5.1, one can use the approximant:

$$\eta_u \cong 1 - \exp\left[-\frac{3}{2}\left(\gamma \dot{m} - 1\right) \right], \quad \left(\gamma = \frac{\beta_i L}{v_n S \sqrt{2em\Delta\varphi_i}} \right) \tag{5.2}$$

Assuming that β_i, $\Delta\varphi \propto V_d$ and energy efficiency is constant, in order to improve the propellant utilization efficiency it is concluded there 2 measures from these equations as:

1. Apply more discharge voltage V_d and more propellant mass flow rate $\dot{m}$
2. Reduce the cross-section area of the channel S

Figure 5.24 shows the relation between the product of channel mean diameter and channel height and propellant utilization efficiency calculated by Eq.5.2.

Now, it is assumed that the anode efficiency more than 50 % with argon propellant is achieved, which means that $\eta_a = 0.65$, $\eta_u = 0.81$ and $\eta_e = 0.95$. At first, the first approach of two measures above is considered. According to the green line in Figure 5.24, $\boldsymbol{Q \times V_d^{0.5}}$ >141, the propellant utilization efficiency of UT-58 can achieve more than 80 %, which results in more than 50 % of anode efficiency with the cross-section area of the thruster is let the same as that of UT-58. However, the PPUs and evacuation of the vacuum system limits the value of input power less than the value which $\boldsymbol{V_d}$=300 V and $\boldsymbol{Q}$=7.0 Aeq (the blue line in Figure 5.21). Conversely, if the PPUs and vacuum evacuation are improved, more than 80 % of propellant utilization efficiency with UT-58 will be achieved.

Consequently, the second measure above has to be considered. The blue line in Figure 5.21 shows the relation between the channel cross-section and propellant utilization efficiency with the operation limits. It is concluded that in order to achieve more than 80 % of propellant utilization efficiency $\boldsymbol{S}$<386 has to be filled. Following the scaling law shown in Chapter 3, we can chose the parameter *d* and *b* as:

$$d = 48 \ \text{(mm)}, \quad b = 8 \ \text{(mm)} \tag{5.3}$$

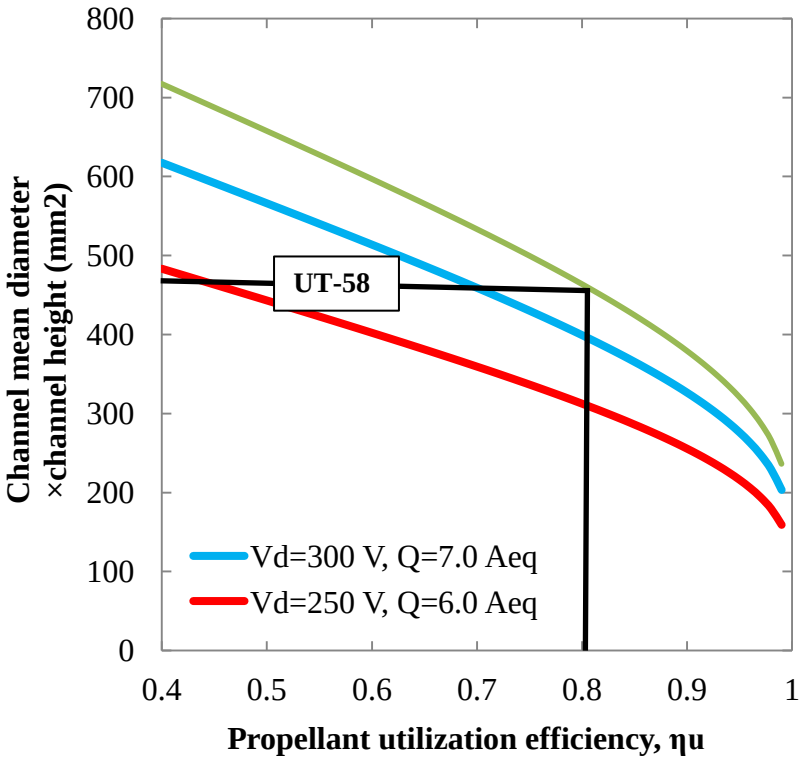

Figure 5.24 Relation between channel cross-section area and propellant utilization efficiency with argon propellant.

5.4.3 Scaling Method for the Optimal Argon Anode Layer Hall Thrusters

In order to detect further the scaling method for optimal argon thrusters, we developed the channel geometry determination flow as shown in Figure 5.25. Generally, there are six parameters to fix the thrust performance of the thrusters, which are input power $\boldsymbol{P}$, thrust $\boldsymbol{F}$, specific impulse $\boldsymbol{I_{sp}}$, anode efficiency $\boldsymbol{\eta_A}$, propellant flow rate $\dot{m}$ and discharge voltage $\boldsymbol{V_d}$. First of all, three of them are required to fix the thrust performance, and lest of them are determined by following equations as:

$$\eta_A = \frac{gI_{sp}F}{2P} \tag{5.4}$$

$$\dot{m} = \frac{F^2}{2\eta_A P} \tag{5.5}$$

$$P = I_d V_d \tag{5.6}$$

$$I_d = C\dot{m} \tag{5.7}$$

And as is described in Chapter 3, the total anode efficiency is described as:

$$\eta_A = C' \cdot \eta_{losses} \cdot \eta_u \tag{5.8}$$

Then the loss efficiency and propellant utilization efficiency can be described using designing parameters, $\varepsilon_{w_ref.Ar}$, $\varepsilon_{a_ref.Ar}$, $\varepsilon_{i_ref.Ar}$ and channel geometry ***d***, ***L/b*** as:

$$\eta_{loss} = 1 - \frac{V_{d_ref}}{V_d}\left[\frac{L}{b}\left(\frac{L}{b}\right)^{-1}{}_{ref}\,\varepsilon_{w_ref} + \left(\varepsilon_a + \varepsilon_i\right)_{ref}\right] \tag{5.9}$$

$$\eta_u = 1 - \exp\left(-\frac{\dot{m}\sqrt{V_d}}{v_n \pi \sqrt{2em_i}} \cdot \frac{1}{d} \cdot \frac{L}{b}\eta_u\right) \tag{5.10}$$

We have to get these designing parameters by the experimental results using argon propellant shown in Figure 5.23. When the propellant flow rate was 6.0 Aeq and discharge voltage was 250 V, the propellant utilization efficiency was 0.446 and anode efficiency was 0.15. Therefore, we can calculate these designing parameters as flows:

$$0.15 = 0.446 \times C'' \times \eta_{loss} \quad \text{then} \quad \eta_{loss} = 1 - \varepsilon_{w.Ar} - \varepsilon_{aAr} - \varepsilon_{i.Ar} = 0.373 \tag{5.11}$$

As for ***C***", the constant value from Eq. 3.4 is used. Using Eq. 3.6, Eq. 3.7 and Eq. 3.8, loss factors with argon propellant and the same thruster can be calculated as shown in Table 5.2. Finally, we can calculate as an output the total anode efficiency by giving the appropriate channel geometry, ***d***, ***b*** and ***L.*** Then check that it is the same or not as the first determined anode efficiency by required three parameters. If that is the same, such geometry is optimal. However if that was wrong, it is necessary to give three required parameters or appropriate channel geometry again, and iterate until the output total anode efficiency is the same as the first determined one. The next paragraph shows how to determine the channel geometry to achieve the highest anode efficiency.

Table 5.2 Calculated loss factors of UT-58 with argon propellant

Parameters	Xenon (Reference)	Argon	Unit of measure
V_d	400	250	V
$\dot{m}$	3	6	Aeq
ε_w	0.096	0.252	n.d.
ε_a	0.038	0.1	n.d.
ε_i	0.105	0.275	n.d.
η_A	0.673	0.15	n.d.

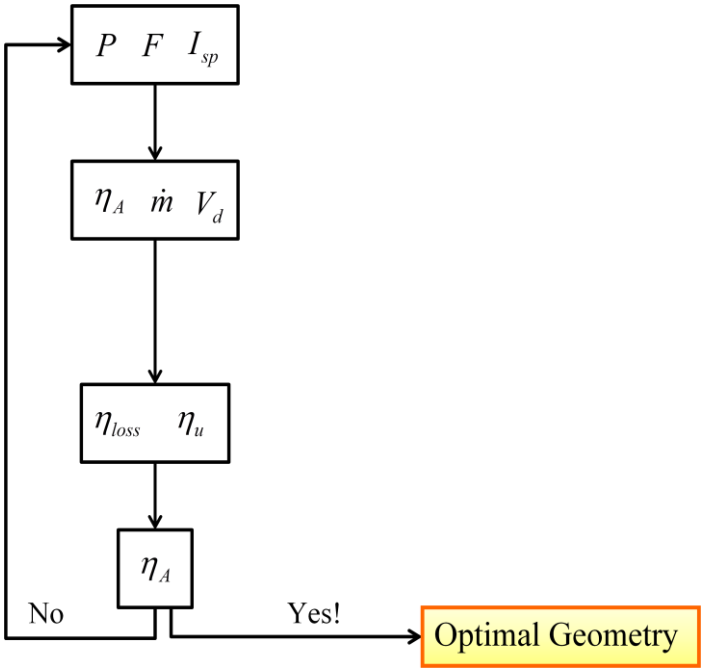

Figure 5.25 Channel geometry determination flow.

Using the experimental result shown in 5.4.1, the relation map among channel mean diameter, aspect ratio of channel length and width, and output anode efficiency can be described. Figure 5.26 shows the relation among channel geometric parameters and output anode efficiency calculated by the experimental results when the discharge voltage was 250 V and propellant flow rate was 6.0 Aeq. The red point shows the real anode efficiency of UT-58 whose ***d*** is 58 mm and ***L/b*** is 0.25. This figure shows that the smaller the channel mean diameter is, the output anode efficiency increases. This can be understood from Eq. 5.10, which means the propellant utilization efficiency is improved. And this figure also shows that each channel diameter has the optimal aspect ratio of channel Length and channel width. Figure 5.27 shows the optimal anode efficiency line with appropriate ***d*** and ***L/b***, that is, the orthographic projection to the basement of the curve surface ridge in Figure 5.26. Once the channel mean diameter is fixed, it is possible to select the appropriate aspect ratio using Figure 5.27. It should be noted that there are some limitations by the magnetic circuit designing, heat flux calculation and wall erosion estimation. The thruster needs to be designed with magnetic circuit which has inner coil in the center axis in many cases. Therefore, we cannot chose the too small channel mean diameter because of these limitations. Once a channel mean diameter and an aspect ratio are determined, we have to design the magnetic circuit and calculate the heat flux to the coils at least. If those channel geometry is not appropriate in terms of these limitations, we have to go back to determine the different channel geometry again.

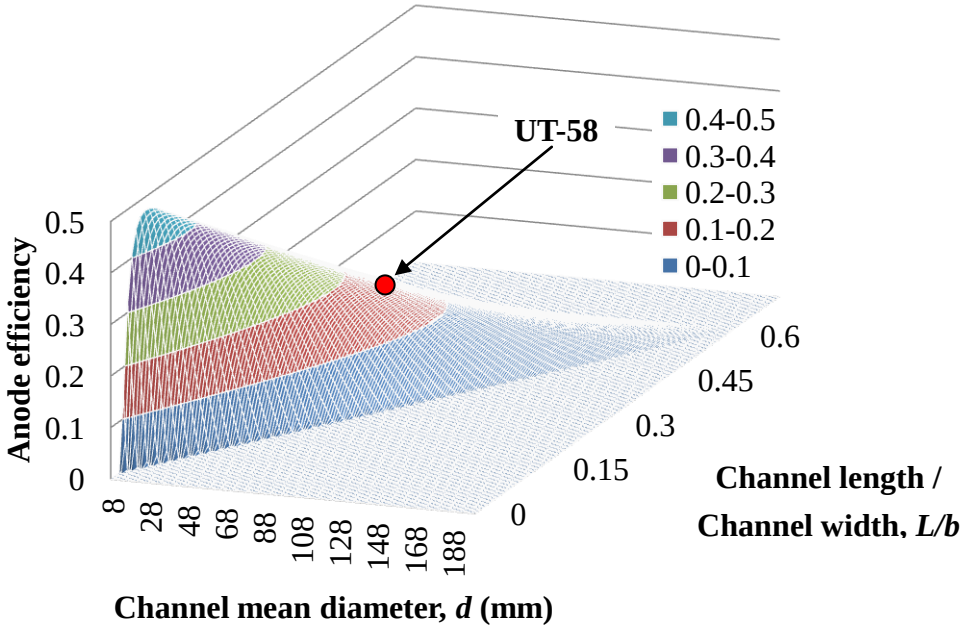

Figure 5.26 Relation among channel mean diameter, aspect ratio of channel length and channel width, and output anode efficiency (V_d = 250 V, Q = 6.0 Aeq).

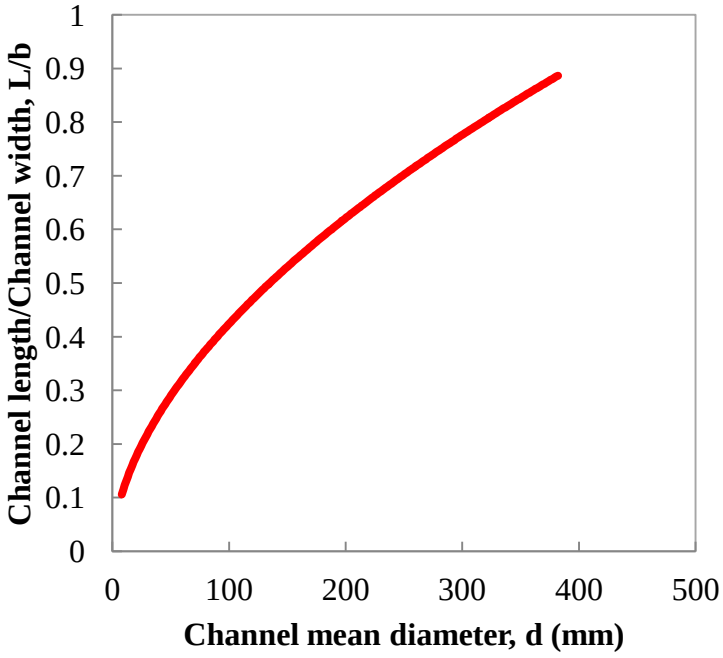

Figure 5.27 Optimal anode efficiency line with appropriate *d* and *L/b*.

<The next generation argon thruster design>

Using the method above, the more efficient argon anode layer thruster can be designed with the present operating parameters (V_d = 250 V, Q = 6.0 Aeq) as the next step. Figure 5.28 shows the relation among the channel geometric parameters and the output anode efficiency with present operating parameters. And Figure 5.29 shows the optimal anode efficiency line with appropriate *d* and *L/b* in this case. As is noted in the previous paragraph, we have to be careful of choosing the channel geometric values because of the some limitations. In order to achieve almost 40 % of anode efficiency with the next generation argon thruster, it can be suggested that the channel mean diameter ***d*** is 45 mm and the aspect ratio ***L/b*** is 0.27, which achieves 37 % of anode efficiency. The supposed specifications of this thruster are shown in Table 5.3.

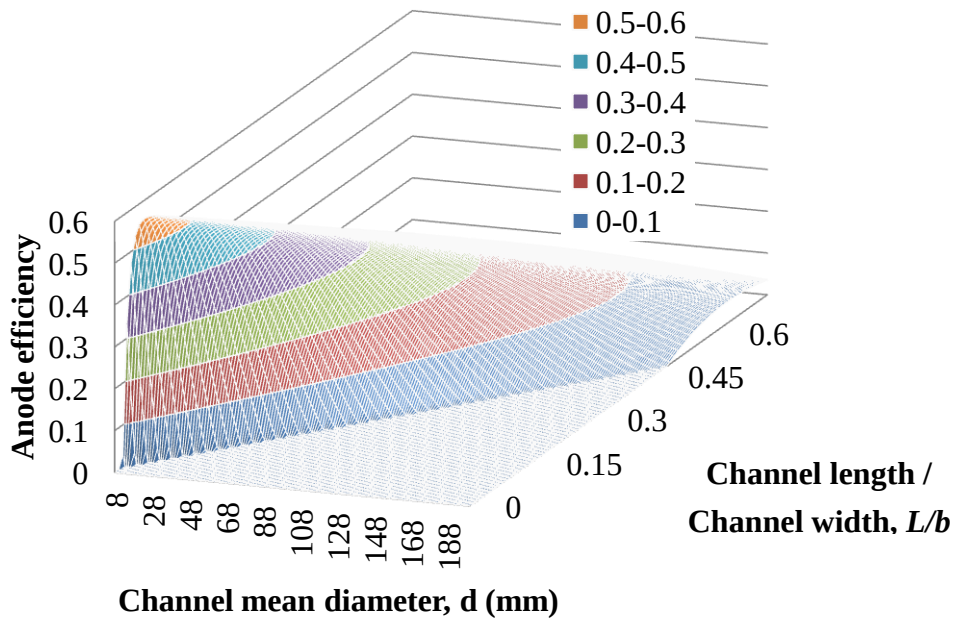

Figure 5.28 Relation among channel mean diameter, aspect ratio of channel length and channel width, and output anode efficiency (V_d = 300 V, Q = 7.0 Aeq).

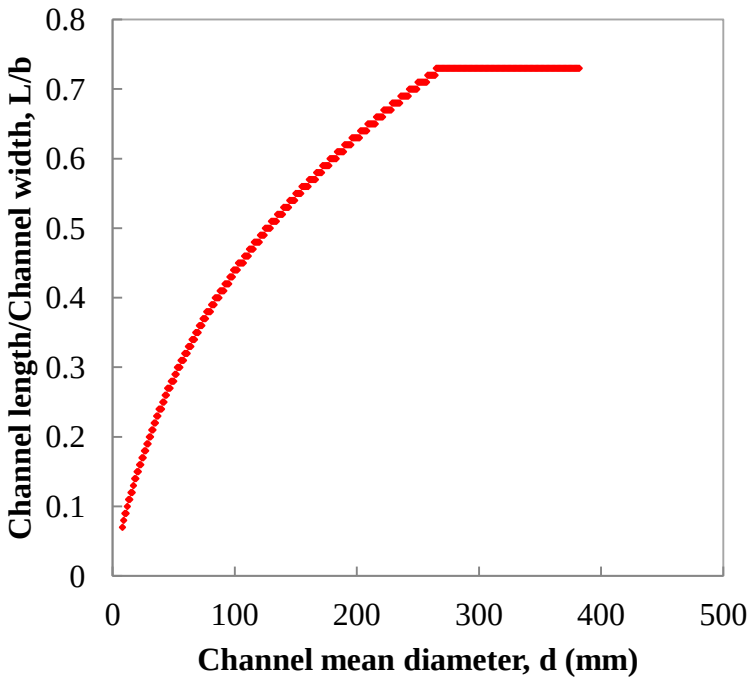

Figure 5.29 Optimal anode efficiency line with appropriate *d* and *L/b*.

Table 5.3 Supposed specifications of the next generation argon thruster.

Parameters	Values	Unit of measure
V_d	300	V
P	2300	W
$\dot{m}$	7	Aeq
F	49.7	mN
I_{sp}	1748	s
η_A	0.37	n.d.
d	45	mm
b	6	mm
L	1.62	mm

<Future argon thrusters design to achieve the JAXA's next asteroid mission>

As is shown in Figure 1.9, JAXA established the mission roadmap to achieve exploring next asteroid in 2028. In order to achieve this mission with argon anode layer Hall thrusters, the optimal channel geometric design is considered in this paragraph. When it is assumed four argon thrusters are clustered to achieve this mission, the required parameters are shown in Table 5.4. By calculating the relation among the channel geometric parameters and output anode efficiency considering these requirements, the optimal channel geometry can be determined by the Figure 5.30. In order to achieve this mission by four argon thrusters, it can be suggested that the channel mean diameter ***d*** is 300 mm and the aspect ratio ***L/b*** is 0.15, which achieves 50 % of anode efficiency. The supposed geometry of these thrusters are shown in Table 5.5.

Table 5.4 Required parameters per one thruster for next asteroid mission.

Parameters	Values	Unit of measure
V_d	300	V
P	40000	W
$\dot{m}$	136	Aeq
F	1500	mN
I_{sp}	2721	s
η_A	0.5	n.d.

Table 5.5 Optimal channel geometry for next asteroid mission.

Parameters	Values	Unit of measure
d	300	mm
b	60	mm
L	9	mm

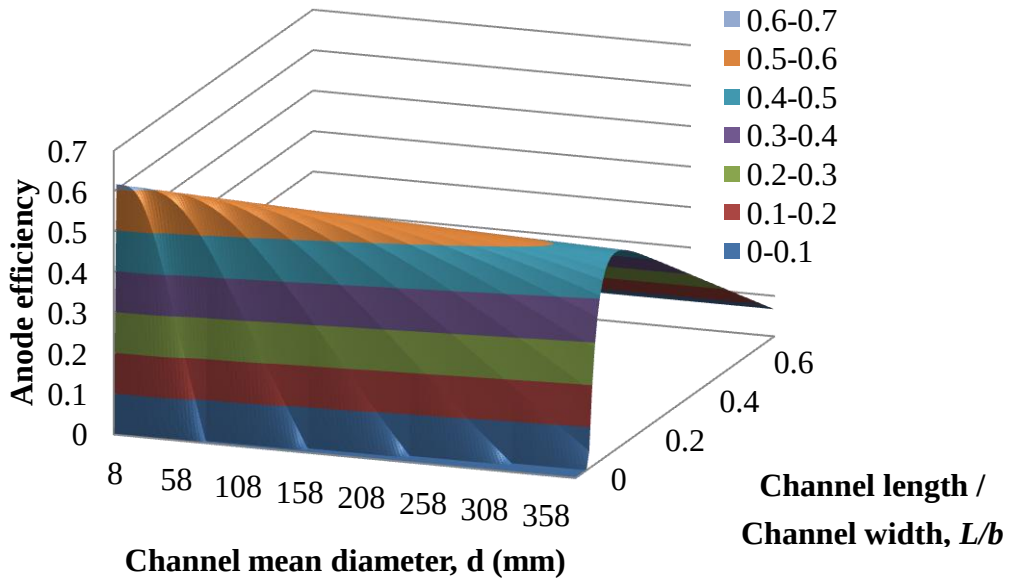

Figure 5.30 Relation among channel mean diameter, aspect ratio of channel length and channel width, and output anode efficiency (V_d = 300 V, Q = 136 Aeq).

5.4.4 Validation of Scaling Method by the Results with Xenon Propellant

In order to validate the scaling method above, the experimental results with xenon propellant are used. In this research, the propellant utilization efficiency with xenon propellant was not measured, hence, it needs to be assumed by comparing the thrust with both xenon and argon propellant. The thrust can be expressed using the propellant utilization efficiency as:

$$F = \eta_u \dot{m} \sqrt{\frac{2\eta_e e V_d}{m}} \tag{5.12}$$

And propellant mass ratio is introduced as:

$$\kappa = \frac{m_{Xe}}{m_{Ar}} \tag{5.13}$$

Assuming that the discharge voltage and energy efficiency is constant, the ratio of the propellant utilization efficiency is described as:

$$\frac{\eta_{u\,xe}}{\eta_{u\,Ar}} = \frac{F_{Xe}}{F_{Ar}} \cdot \frac{\dot{m}_{Ar}}{\dot{m}_{Xe}} \cdot \sqrt{\kappa} \tag{5.14}$$

By using Eq. 5.14, the propellant utilization efficiency with xenon propellant can be calculated. The thrust of both propellants with the discharge voltage is 250 V and calculated propellant utilization efficiency with xenon propellant are shown in Table 5.6. It is concluded that the propellant utilization efficiency with xenon propellant is quite higher (almost 100 %) than that with argon propellant. Next, the relation among the channel geometric parameters and output anode efficiency with xenon propellant when the discharge voltage is 250 V and propellant utilization efficiency is 3.0 Aeq as shown in Figure 5.31. The red point shows the real anode efficiency of UT-58 whose ***d*** is 58 mm and ***L/b*** is 0.25. The experimental result of anode efficiency with these operating parameters is 68 %. On the other hand, the calculated anode efficiency with UT-58's channel geometry is 68.3 %, which well accords with the experimental result. Therefore, this scaling method should be reliable.

Table 5.6 Measured thrust and calculated propellant utilization efficiency with xenon and argon propellant.

Parameters	Xenon	Argon
Mass flow rate (Aeq)	3	6
Mass flow rate (mg/s)	4.08	2.48
Thrust (mN)	66.3	32.7
Propellant utilization efficiency (%)	99.5	44.6

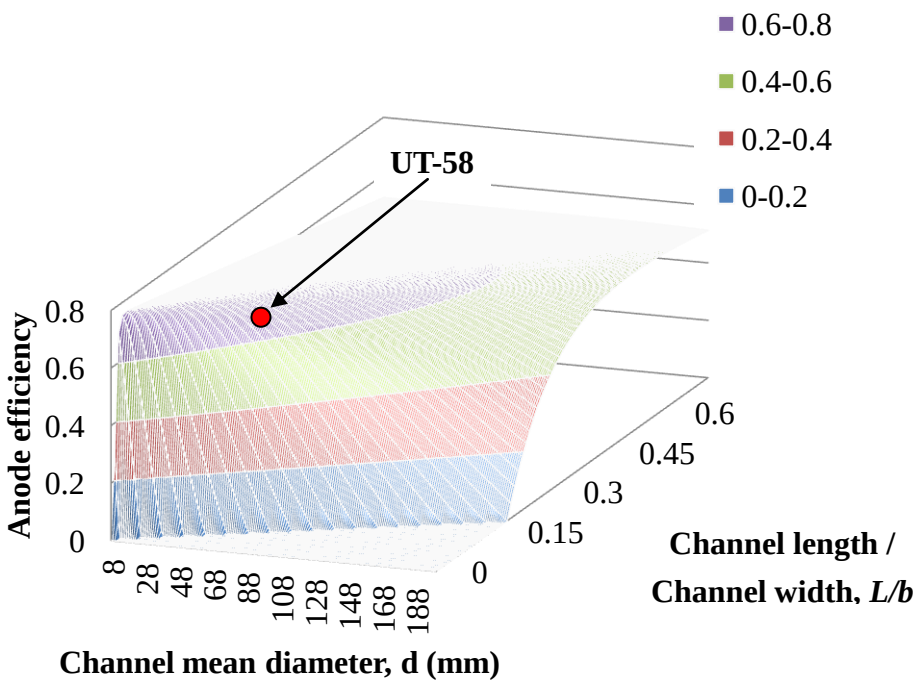

Figure 5.31 Relation among channel mean diameter, aspect ratio of channel length and channel width, and output anode efficiency with xenon propellant (V_d = 250 V, Q = 3.0 Aeq).

Chapter 6

Conclusions

For the understanding the operation characteristics and the construction for argon anode layer Hall thrusters, experimental investigation was conducted. As a result, we got following conclusions using the newly developed anode layer Hall thruster, UT-58:

1. UT-58 achieved high anode efficiency of 23.5 % with argon propellant showing the predominance over other propellant candidates for the future large space exploration missions.

2. The optimal operation regime with argon propellant is in the classical diffusion region where the magnetic flux density is lower, which has the advantage of being more likely to feature the magnetic shielding system having lower magnetic flux.

3. The scaling law for the optimal channel geometry with argon propellant was constructed using the experimental results. The next generation argon thruster has 45 mm of the channel mean diameter and 0.27 of the aspect ratio of the channel length and channel width.

This research shows the possibility to choose the argon propellant for the future large space exploration missions and uncovered the design guideline to achieve higher efficiency and less erosion by the magnetic shielding. From the above, this research is considered to have a major impact on the project ‘RAIJIN’, and contribute to execute future large space exploration missions in JAXA’s roadmap.

Bibliography

1. 栗木恭一，荒川義博：電気推進ロケット入門，東京大学出版会，2003.

2. Dan M. Goebel, and Ira Katz,: Fundamentals of Electric Propulsion: Ion and Hall Thrusters, JPL Space Science and Technology Series, Jet Propulsion Laboratory, California Institute of Technology, 2008.

3. Ronald W. Humble, Gary N. Henry, Wiley J. Larson,: Space Propulsion and Design, Learning Solutions, 1995.

4. Brown, D. L., Larson, C. W., and Beal, B.E.,: Methodology and Historical Perspective of a Hall Thruster Efficiency Analysis, AIAA Journal of Propulsion and Power, Vol. 25, No. 6, 2009, pp. 1163-1177

5. Dumazert, P., Verdier, S. L.., Marchandise, F., Koppel, C. R., Garnero, P. and Blame F.: PPS-1350-G Qualification Status March 2003, IEPC Paper 2003-270, 2003.

6. Marchandise, F. R.., Biron, J., Gambon, M. Cornu, N., Darnon, F. and Estublier D.: The PPS 1350 qualification demonstration 7500h on ground, about 5000h in flight, IEPC Paper 2005-209,2005

7. Koppel, C. R., Estublier, D.: The SMART-1 Hall Effect Thruster Around the Moon: In Flight Experience, IEPC Paper 2005-119,2005.

8. Ozaki, T., Kasai, Y., Inanaga, Y., Nakagawa, T., Osuga, H., Itoh, T., Kajiwara, K. and Matsui, K.: Electric Propulsion Development Activity at MELCO. AIAA Paper 2006-4321, 2006.

9. Zhurin, V. V., Kaufman, H. R. and Robinson, R. S.: Physics of closed drift thrusters, Plasma Source Science and Technology, 8 (1999), R1-R20.

10. Kim, V., Popov, G., Arkhipov, B., Murashko, V., Gorshkov, O., Koroteyev, A., Garkusha, V., Semenkin, A. and Tverdokhlebov, S.: Electric Propulsion Activity in Russia, IEPC Paper 2001-005, 2001.

11. Semenkin, A. V., Tverdokhlebov, S. O., Garkusha, V. I., Kochergin, A. V., Chislov, G. O., Shumkin, B. V., Solodukhin, A. V. and Zakharenkov, L. E.: Operating Envelopes of Thrusters with Anode Layer, IEPC Paper 2001-013, 2001.

12. Yim, J. T., Keidar, M. and Boyd, I. D.: And Evaluation of Sources of Erosion in Hall Thrusters, AIAA Paper 2005-3530, 2005.

13. Choueiri, E. Y.: Fundamental Difference between the Two Hall Thruster Variants, Physics of Plasma, 8 (2001), pp. 5025-5033.

14. Semenkin, A., Kochergin, A., Garkusha, V., Chislov, G. and Rusakov, A.: RHETT/EPDM Flight Anode.

15. Manzella, D., Oleson, S., Sankovic, J., Haag, T., Semeskin, A., Kim, V.: Evaluation of low power Hall thruster propulsion, AIAA Paper 1996-2736, 1996.
16. Ashkenazy, J., Raitses, Y., Appelbaum, G.: Low Power Scaling of Hall Thrusters, ESPC Paper, 1997.
17. Semeskin, A.: Demonstration Tests and an Anode Analysis of Critical Issues Associated with Low Power TAL, 2000.
18. Jesse, A. L., Alec, D. G.: Efficiency Analysis of a Hall Thruster Operating with Krypton and Xenon, Journal of Propulsion and Power, Vol. 22, pp. 1402-1412, 2006.
19. James, S., Mike, R., John, D.: Light Metal Propellant Hall Thrusters, IEPC Paper 2009-138, 2009.
20. Nagao, N., Kinefuchi, K., Saito, Y., Okita, K. and Kuninaka H.: Activities for High Power Electric Propulsion System in Japan, ISTS Paper 2013-b-10, 2013.
21. Miyasaka, T., Komurasaki, K., Koizumi, H., Schönherr, T., Yamamoto, N., Tahara, H., Takegahara, H., Nakano, M., Aoyagi, J., Funaki, I., Watanabe, H., Okawa Y., Kakami A., Takao, Y., Yokota, S., Ozaki, T. and Osuga, H.: Overview on Developments of High-Power Anode Layer Thruster in Japan, ISTS Paper 2013-o-1-01, 2013.
22. Yamamoto, N., Miyasaka, T., Komurasaki, K., Koizumi, H., Schönherr, Tahara, H., Takegahara, H., Aoyagi, J., Nakano, M., , Funaki, I., Watanabe, H., Okawa Y., Kakami A., Takao, Y., Yokota, S., Ozaki, T. and Osuga, H.: Developments of Robust Anode-layer Intelligent Thruster for Japan IN-space propulsion system, IEPC Paper 2013-244, 2013.
23. Y. Ito, M. Nakano, T. Shönherr, S. Cho, K. Komurasaki, H. Koizumi: In-Space Transportation of a Solar Power Satellite Using a Hall Thruster Propulsion System, ICREA, 2012.
24. Zakharenkov, L., Chislov, G. and Semeskin, A.: Study of Low Power TAL Characteristics, IEPC Paper 2001-041, 2001.
25. 高橋大祐,: アノードレイヤ型ホールスラスタの推進性能向上に向けた設計最適化, 東京大学, 2011, 修士論文.
26. 福島靖博,: 周方向に非一様な推進剤供給によるホールスラスタの放電安定化, 東京大学, 2009, 修士論文.
27. Yamamoto, N., Komurasaki, K. and Arakawa, Y.: Discharge Current Oscillation in Hall Thrusters, Journal of Propulsion and Power, Vol. 21, pp. 870-876, 2005.
28. 山本直嗣,: ホールスラスタの放電振動に関する研究, 東京大学, 2003, 博士論文.
29. 野中吉紀,: ホールスラスタの作動特性と推進性能, 東京大学, 1994, 修士論文
30. Chen, F. F.: Introduction to Plasma Physics and Controlled Fusion, Plenum Press, New York, 1984.

31. Hagelaar, G. J. M., Bareilles, J., Garrigues, L. and Boeuf, J. P.: Role of anomalous electron transport in a stationary plasma thruster simulation, Journal of Applied Physics, Vol. 93, pp. 67-75, 2003.
32. Meezan, N. B., Hargus, Jr., W. A. and Cappelli, M. A.; Anomalous electron mobility in a coaxial Hall discharge plasma, Physical Review E, Vol. 63, pp. 026410-1-7, 2001.
33. Tamida, T., Suga, I., Nakagawa, T., Osuga, H., Ozaki, T. and Matsui K.: Realization of Low Frequency Oscillation Free Operation in a Hall thruster, IEPC Paper 2007-88, 2007.
34. H. Osuga, F. Kurokawa, T. Tamida and N. Yamamoto: A NEW POWER CONTROL METHOD FOR HALL THRUSTER USING OSCILLAION-MODE-MAP, IAC Paper 2010-C4.4.12, 2010.
35. H. Osuga, F. Kurokawa, T. Tamida and N. Yamamoto: A New Conditions Control for Optimal Power Efficiency of Hall Thruster, 14th International Power Electronics and Motion Control Conference, EPE-PEMC, 2010.
36. H. Osuga, F. Kurokawa, N. Yamamoto and T. Tamida, A New Magnetic Flux Density Control Method to Improve Power Consumption of Hall Thruster, IEPC Paper 2011-182, 2011.
37. Tommaso, M., Francesco, B., Christian, B., Enrico, A. D. M. and Mariano, A.: High Power Hall Thrusters Design Options, IEPC Paper 2007-311, 2007.
38. Ahedo, E.: Presheath/sheath Model with Secondary Electron Emission from Two Parallel Walls, Physics of Plasma, Vol. 9, no. 10, pp. 4340-4347, 2002.
39. Morozov, A. I., Esiphcuk, Y.V., Tilinin, G. N., Trofimov, A. V., Sharov, Yu. A., and Shshepkin, G. Ya.: Plasma Accelerator with Closed Electron Drift and Extended Acceleration Zone, Soviet Physics-Technical Physics, Vol. 17, no. 1, 1972.
40. Ryan, W. C., Dan, M. G., Richard, R. H., Taylor, S. M. and Richard, E. W.: Magnetically Shielded Miniature Hall Thruster: Development and Initial Testing, IEPC Paper 2013-201, 2013.
41. Garrigues, L., Mazouffre, S., Hénaux, C., Vilamot, R., Rossi, A., Harribey, D., Bourgeois, G., Vaudolon, J. and Zurbach, S.: Design and first test campaign results with a new flexible magnetic circuit for a Hall thruster, IEPC Paper 2013.250, 2013.
42. Ioannis, G. M., Ira K., Richard, R. H., Dan, M. G., Kristi, d. G. and Alex, M.: Magnetic shielding of the channel walls in a Hall plasma accelerator, Physics of Plasmas, Vol. 18, 033501, 2011.
43. Yamamoto, N., Komurasaki, K. and Arakawa, Y.: Condition of Stable Operation in a Hall Thruster, IEPC Paper 2003-086, 2003.
44. 横田茂, 安井伸輔, 熊倉賢, 小紫公也, 荒川義博: アノードレイヤ型ホールスラスタ内部のシース構造と放電電流の数値解析, 日本航空宇宙学会論文集, Vol. 54, pp. 39-44, 2006.
45. Goebel, D. M., Crow, J. T. and Forrester, A. T.: Lanthanum hexaboride hollow cathode for dense plasma production, Review of Scientific Instruments, 49 (1978), pp. 469-472.
46. Dan M. Goebel and Emily Chu: High Current Lanthanum Hexaboride Hollow Cathode for 20-to-100 kW Class Hall Thrusters, AIAA-2012-4079, 48th JPC, Atlanta, July 2102.

47. N. Nagao, S. Yokota, K. Komurasaki, and Y. Arakawa: Development of a 2D Dual Pendulum Thrust Stand for Hall Thrusters, Review of Scientific Instruments, Vol. 76, 115108, 2007.
48. Hargus, W. A. Jr., Meezan, N. B. and Cappelli, M. A.: The Transit Behavior of a Low Power Laboratory Xenon Hall Thruster, AIAA Paper, 2008-5187, 2008.
49. A.A. Shagaida, O. A. Gorshkov, and D. A. Tomilin: Influence of the Erosion of the Discharge Channel Wall on the Efficiency of a Stationary Plasma Thruster, Technical Physics, 2012, Vol. 57, pp. 1083-1089, 2012.

Conference Presentations

1. 藤田大樹, 張科寅, 川嶋嶺, 細田誠也, 伊藤裕樹, 赤木将平, 小紫公也, 小泉宏之, Tony Schönherr, 荒川義博: アルゴン作動アノードレイヤ型ホールスラスタの作動特性, 第 53 回航空原動機・宇宙推進講演会, JSASS-2013-0012, 2013.
2. Daiki Fujita: Operating Parameters and Oscillation Characteristics of Anode Layer Hall Thruster with Argon Propellant, 29th International Symposium on Space Technology and Science, June 2013, 2013-s-07-b, 2013.
3. T. Schönherr, D. Fujita, Y. Ito, R. Kawashima, S. Cho, H. Koizumi, and K. Komurasaki: Argon anode-layer thruster for mass space transportation," 29th International Symposium on Space Technology and Science, June 2013. ISTS 2013-o-1-03.
4. T. Schönherr, Y. Ito, D. Fujita, R. Kawashima, H. Koizumi, and K. Komurasaki: Influential parameters for discharge behavior and performance of anode-layer thruster, 31st International Conference on Phenomena in Ionized Gases, July 2013.
5. D. Fujita, K. Komurasaki: Operating Parameters and Oscillation Characteristics of Anode-Layer Hall Thruster with Argon Propellant, The 9th International Symposium on Applied Plasma Science, E-3, 2013.
6. T. Schönherr, R. Kawashima, H. Koizumi, K. Komurasaki, D. Fujita, and Y. Ito: Design and performance evaluation of thruster with anode layer UT-58 for high-power application, 33rd International Electric Propulsion Conference, Oct. 2013. IEPC-2013-242.
7. 藤田大樹, 川嶋嶺, 伊藤裕樹, 赤木将平, 鈴木淳, Tony Schönherr, 小泉宏之, 小紫公也, H25 年度宇宙輸送シンポジウム, STEP-2013-054, 2013.
8. T. Schönherr, D. Fujita, Y. Ito, P. Bambach, J. Suzuki, R. Kawashima, H. Koizumi, and K. Komurasaki: Performance evaluation and probe measurements of argon-based high-power thruster with anode layer UT-58, Asian Joint Conference on Propulsion and Power 2014, Mar. 2014.

Journal Papers

1. Daiki Fujita, Rei Kawashima, Yuki Ito, Shohei Akagi, Jun Suzuki, Tony Schönherr, Hiroyuki Koizumi, Kimiya Komurasaki: Operating parameters and oscillation characteristics of an anode-layer Hall thruster with argon propellant, Journal of Vacuum, Aug. 2014. Under review.